

# **FRACTURE TOUGHNESS MEASUREMENTS IN A HSLA STEEL**

by

**ABHIJIT SENGUPTA**

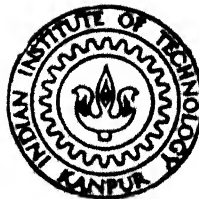
ME

1988

M

SEN

FRA



**DEPARTMENT OF METALLURGICAL ENGINEERING**

**INDIAN INSTITUTE OF TECHNOLOGY, KANPUR**

**JANUARY, 1988**

# **FRACTURE TOUGHNESS MEASUREMENTS IN A HSLA STEEL**

A Thesis Submitted  
In Partial Fulfilment of the Requirements  
for the Degree of

**MASTER OF TECHNOLOGY**

**18401**

by  
**ABHIJIT SENGUPTA**

*to the*

**DEPARTMENT OF METALLURGICAL ENGINEERING  
INDIAN INSTITUTE OF TECHNOLOGY, KANPUR**

**JANUARY, 1988**

13 APR 1989  
CENTRAL LIBRARY  
U. S. AIR FORCE  
Acc. No. A.104131

ME-1980-M-SEN-FRA

(ii)

4/1/88  
Dr. M.N. Shetty

CERTIFICATE

This is to certify that this work entitled  
'Fracture Toughness Measurements in a HSLA steel' has been  
carried out under my supervision and has not been submitted  
elsewhere for a degree.



Dr. M.N. Shetty  
Professor  
Department of Metallurgical  
Engineering  
Indian Institute of  
Technology  
Kanpur.



ACKNOWLEDGEMENTS

It is my pleasant duty to record here my deep sense of gratitude to my thesis supervisor, Dr. M.N. Shetty, Professor, Department of Metallurgical Engineering, firstly for suggesting this challenging project and secondly for the many enlightening discussions we had during the course of this work. His constructive criticism and suggestions were always readily available to me and this has a source of strength throughout.

I am thankful to the Physical Metallurgy Laboratory Group, Steel Authority of India Limited, Ranchi, especially to Dr. Sanak Mishra, Dr. Santanu Ray, EPMA operator Mr. Patra for their whole hearted co-operation to me during my association with them. I shall for ever cherish their companionship.

I am very much thankful to Mr. V.P. Gupta for being extremely helpful throughout my project work and for his excellent sketches in this thesis.

Thanks are due to Mr. B.K. Jain for his kind interest, encouragement and valuable contributions in carrying out my experiments.

Excellent cooperation of Mr. K.P. Mukherjee, Mr. P.K. Pal, Mr. Rohman, Mr. R.C. Sharma, Mr. Sreevastava,

Mr. Mandal are greatly appreciated. I am thankful to all my colleagues, in particular, Mr. S. Kumar, Mr. K.R. Upadhyaya. Mr. S.N. Pradhan's impeccable typing has helped me in no small measure in compiling this report in a short time.

I am also thankful to DMRL, Hyderabad and Indira Gandhi Centre for Atomic Research, Kalapakkam for sending ineffably beautiful TEM photographs.

Finally, I thank all my friends in the campus for making my stay here a memorable one.

ABHIJIT SENGUPTA

CONTENTS

CHAPTER		Page
CHAPTER I	INTRODUCTION	
1.1	General	1
1.2	Linear Elastic Fracture Mechanics	3
	1.2.1 Energy balance approach to fracture	3
	1.2.2 Stress intensity factor approach to fracture	6
1.3	Yielding Fracture Mechanics	14
	1.3.1 The role of extent of plasticity	14
	1.3.2 Concept of crack opening displacement (COD)	17
	1.3.3 Concept of J-intergral	21
1.4	Methods of Fracture Toughness Measurements	27
	1.4.1 $K_{Ic}$ testing	27
	1.4.2 COD testing	33
	1.4.3 J-determination techniques	34
	1.4.4 New test methods	44
1.5	Scanning Electron Microscope and its application to Fractography	45
	1.5.1 Principal Features of SEM	45
	1.5.2 Operation of SEM	47
	1.5.3 Specimen Preparation	50
	1.5.4 Unique Features	51
	1.5.5 Production and Viewing of SEM Fractographs	52
	1.5.6 Defects and Limitations of SEM	52

1.6	Electron Micro Probe Analyzer and its application to Fractography	54
1.6.1	Theory of operation	55
1.6.2	Mode of Data Presentation	55
1.6.3	Specimen Preparation	56
1.7	Transmission Electron Microscope and its application to Fractography	57
1.7.1	Specimen Selection and Preparation	58
1.7.2	Preparation from Bulk Sections	59
1.7.3	Artifacts of Specimen Preparation	59
1.7.4	Application to Thin Foil Technique	60
1.7.5	Specimen manipulation	60
1.7.6	Selected Area Diffraction	60
1.7.7	Bright and Dark Field Electron Microscopy	61
1.7.8	Applications of TEM	62
1.7.9	Image Defects in Electron Lenses	63
1.8	Effects of Heat Treatments on Fracture Toughness	64
1.8.1	Normalizing followed by Tempering	64
1.8.2	Quenching followed by Tempering	65
1.8.3	Martempering	68
1.8.4	Austempering	69
1.9	Non-metallic inclusions in Steel and their effects on Fracture Toughness	69
1.9.1	Sulfides in Steel	70
1.9.2	Deformability of Steel inclusions	72
1.9.3	Hot Shortness	75
1.9.4	Influence of inclusions on mechanical properties	77

1.10	Segregation to grain boundary, interfaces and fracture	Page 82
CHAPTER II	EXPERIMENTAL PROCEDURE	89
2.1	Bend Test	91
2.1.1	Specimen Design and preparation	91
2.1.2	Test procedure	94
2.1.3	Bend test at various temperatures	97
2.2	Straight Tensile Test	104
2.3	Notched Bar Impact Test	109
2.3.1	Specimen Design and Preparation	109
2.3.2	Test Procedure	110
2.4	Electron Micro Probe Analyzer and Scanning Electron Microscopy	110
2.5	Transmission Electron Microscopy	111
2.6	Optical Microscopy	112
CHAPTER III	RESULTS AND DISCUSSION	113
3.1	Bend Test Results	113
3.2	Tensile Test Results	119
3.3	Impact Test Results	120
3.4	Composite Curves	132
3.5	Effects of Heat treatments and optical microscopy results	136
3.6	Electron Micro Probe Analyser and Scanning Electron Microscopy results and Effects of microstructure on Fracture Toughness	144
3.7	Effects of non-metallic inclusions on Fracture Toughness	152
3.8	Transmission Electron Microscopy Results	155

	Page
3.9 Determination of $Q$	165
3.10 Comparision with the Literature Value of $J_{1c}$	169
CONCLUSION	170
REFERENCES	171

LIST OF FIGURES

<u>Number</u>	<u>Title</u>	<u>Page</u>
1	Crack--deformation modes	1
2	Model for equations for stresses at a point near a crack	1
3	Some crack configurations	12
4	Schematic representation of increasing degree of yielding	16
5	The Dugdale model for crack tip plasticity	16
6	Arbitrary contour over which J-integral is evaluated	22
7	Crack tip schematic of the fracture process	22
8	Schematic of compact specimen	29
9	Schematic force/displacement records showing quantities involved in analysis	32
10	Schematic force/displacement records for calculation of COD	32
11	Schematic load-displacement curves with prescribed load/displacement	35
12	Schematic of steps in a compliance J determination	38
13	Schematic showing Rice-Merkle J formula for bend type specimen	38
14	Procedure for experimental $J_{1c}$ measurement	41
15	Essential components of SEM	46
16	Useful signals generated by an electron beam	46
17	Pattern of zones in a specimen	46
18	Selected Area Diffraction Pattern	61

		(x)
		Page
19	Diffraction Contrast	61
20	Free energy of formation of MnS	71
21	Schematic indication of crack formation at metal/inclusion interface	71
22	Effect of rolling temperature on the relative plasticity of MnS	71
23	Part of Fe-S diagram	76
24	Mechanism of ductile fracture when MnS inclusions are involved	76
25	Definition of Plastic instability	80
26	Relationship between surface energy and dihedral angle	80
27	Cumulative frequencies for a dihedral angle	80
28	Effect of Mn:S ratio on dihedral angle of sulfur	84
29	Surface tensions for solutions	84
30	Bend specimen-standard proportions and tolerances	92
31.	Loading condition during bend test	92
32	Bend test apparatus for correction determin- ations	95
33	Method of applying correction to load-displa- cement record	95
34	Direct tensile test specimen Charpy impact test specimen	99
35	Load-displacement records for three-point bent tests at various temperatures	98
36	Load-displacement records for three-point bent tests for various treatments	101
37	Variation of $J_1$ versus temperature	102



	Page
38	Variation of CVN versus temperature 107
39	Stress-Strain Curves of direct tensile tests at various temperatures 105
40	Determination of $J_{1C}$ 108
41	Variation of UTS, YS, $\sigma_f$ versus temperature 124
42	Determination of n from $\ln \sigma$ versus $\ln C$ plot 125
43	Variation of n versus temperature 127
44	Determination of Q from $\ln J_X$ versus $1/KT$ plot 128
45	Variation of fracture toughness ( $J_1$ ) with different heat treatments 137
46	Model heat treatment cycles 138
47	Optical Micrographs 140
48	Electron Micro Probe Analysis pictures and scanning Electron Microscopy fractographs 146
49	Transmission electron microscopy pictures of CVN samples 156
50	Transmission electron microscopy pictures of bend samples 158

## ABSTRACT

Fracture studies are conducted on a high strength low alloy steel. The concept of J-integral in elasto-plastic fracture mechanics, is used to determine the fracture criterion. Slow three point bend tests are carried out on machined and notched specimens and the value of  $J_1$  and  $J_{1c}$  determined from the area under the load-displacement curve. In continuation with an earlier work, the bend tests are carried out in the temperature range of  $440^{\circ}\text{C}$  to  $730^{\circ}\text{C}$ , thus completing a series of J measurements from about  $-77^{\circ}\text{K}$  upto the inter-critical region. With a knee around the ductile to brittle transition temperature,  $J_1$  values increases upto  $490^{\circ}\text{C}$  and followed a sharp decrease upto  $730^{\circ}\text{C}$ . Direct tensile and charpy impact tests are also carried out over the same temperature range and it is found that the  $J_1$  values correlate well with other mechanical properties such as CVN. The  $J_1$  values versus temperature plot shows three distinct regions, namely, the initial sharp rise in  $J_1$  values from  $0^{\circ}$  to  $100^{\circ}\text{C}$ , plateau region between  $30^{\circ}\text{C}$  to  $230^{\circ}\text{C}$  and finally sharp rise upto  $490^{\circ}\text{C}$ . The lower value of the transition temperature (about  $35^{\circ}\text{C}$ ) found in J tests are compared with that from CVN from an earlier investigation has been attributed to the differences existing between dynamic and static fracture toughness. The  $K_1$  values obtained from a direct conversion of the  $J_1$  values compare well with those reported in literature.

The results also report effects of various conventional heat treatments on  $J_1$ . Microstructural investigations are undertaken in and around the fracture zone using TEM, EMPA and SEM to know the effect of microconstituents on fracture toughness.

## CHAPTER 1

### INTRODUCTION

#### 1.1. GENERAL :

High strength low alloy (HSLA) steels can be processed carefully to produce a fine grained ferrite - pearlite microstructure with an attractive combination of strength and fracture toughness. Microalloying additions of strong carbide and nitride formers provide precipitation hardening and assist in grain refinement. The resultant microstructure has high resistance to cleavage, a low transition temperature and cold formability, and excellent resistance to both opening-mode and shear-mode ductile fracture. All these can be obtained from simple laboratory tests on small specimens. Most of the fracture-toughness testing of ferrite-pearlite HSLA steels to date has involved the resistance of the steels to brittle fracture at low temperature, because of their use in gas pipelines in arctic environments. Thus, most of the available fracture toughness data are from charpy impact tests, drop-weight tests, and most of the knowledge of microstructural effects concerns the DBTT (ductile-brittle transition temperature) and dynamic toughness. But these methods donot always give clear-cut transition temperature and they ignore the influence

of flawsize, shape and of the stresses in the structure . In 1920, Griffith formulated the theory which stated that an existing crack would propagate if the total energy of the system would thereby be lowered. In 1957, Irwin modified Griffith's theory, according to which fracture occurs when the stresses near the crack tip reach a critical value depending upon the material. Griffith-Irwin concept was subsequently modified. The linear elastic fracture mechanics ( LEFM) approach provides quantitative expressions for the fracture stress in terms of crack size and shape and loading conditions. But at higher temperature, this concept becomes unrealistic because materials start behaving plastically near the crack tip. The inclusion of elasto-plastic deformation behaviour has then led to the development of important concepts like the crack opening displacement (COD) and J-integral which give an one-parameter criterion for the fracture toughness of the material.

In the present investigation, since the material is ductile we have opted for the J-integral technique. The method is simpler to carry out and the interpretation of the results are exact and without much error. This method is also eminently suited for high temperature fracture toughness measurements.

Slow bend tests are carried out to determine the J-values, by using the method popularly known as the J-estimation procedure. HSLA steel in our study exhibits dynamic strain ageing between  $30^{\circ}\text{C}$  and  $230^{\circ}\text{C}$  and the J versus temperature plot shows a plateau in this region. The temperature dependence of J has been correlated to the properties in direct tensile tests and charpy impact tests. The microstructural investigations were carried out using optical TEM techniques and detailed fractography was done by using SEM and EMPA to correlate the fracture characteristics with microstructure.

## 1.2 LINEAR ELASTIC FRACTURE MECHANICS

### 1.2.1 Energy Balance Approach to Fracture

Griffith [1] first proposed the energy balance approach for the study of fracture mechanics. He explained that a brittle material contains a population of fine cracks which produces stress concentrations of sufficient magnitude so that theoretical cohesive strength is reached in localized regions at a nominal stress which is well below the critical theoretical value. According to Griffith, 'A crack will propagate when the decrease in elastic strain energy is at least equal to the energy required to create the new crack surface'. This was a significant step towards the establishment of a relationship between failure stress and crack length. Griffith's equations is

$$\sigma = \left( \frac{2E\gamma_s}{\pi c} \right)^{1/2} \quad (1)$$

Where  $\sigma$  is the stress required to propagate a crack in a brittle material,  $E$  is the Young's modulus,  $\gamma_s$  is the surface energy  $c$  is the crack size.

For plastically deforming materials, Orowan 2 & 3 suggested that the Griffith equation would be made more suitable with brittle fracture in metals. by the inclusion of a term  $\gamma_p$  expressing the plastic work required to extend the crack.

$$\sigma_f = \left[ \frac{2E(\gamma_s + \gamma_p)}{\pi c} \right]^{1/2} \approx \left( \frac{E\gamma_p}{c} \right)^{1/2} \quad (2)$$

The surface energy term  $\gamma_s$  can be neglected as compared with  $\gamma_p$ .

Orowan pointed out that the approach would be valid only if plastic deformation was confined to thin layers adjacent to the crack walls. He demonstrated that fracture stress was inversely proportional to the square root of crack length by the modified theory. However, the value of  $\gamma_p$  calculated from these results was three to five times that to be expected from the X-Ray analysis of fractured surface. He concluded that these results would be better explained using a crack tip characterizing parameter approach.

But according to Irwin, fracture would occur when the strain energy release rate reached a critical value if the process was essentially similar for different loadings and geometries. This critical value could be regarded as a material property to be determined for a fracture test. Irwin and Kies [4] noted that the strain energy in an elastic body could be represented by the relationship

$$U = \frac{Q^2 C}{2} \quad (3)$$

where  $Q$  is the characterizing force and  $C$  the compliance of the body, i.e., the displacement at the point of application of  $Q$ .

So the strain energy release rate, with respect to crack extension, can be calculated as,

$$\frac{\partial U}{\partial a} = \frac{1}{2} Q^2 \frac{\partial C}{\partial a} \quad (4)$$

By measuring the compliance of a test specimen, or a component model, with various crack lengths the value of  $\frac{\partial C}{\partial a}$  as a function of crack length could be obtained. A fracture test could be interpreted by evaluating  $\frac{\partial U}{\partial a}$  at fracture using the fracture load and the value of  $\frac{\partial C}{\partial a}$  for appropriate crack length.

Irwin [5] proposed that critical strain energy release rate could be regarded as a force. In these terms, fracture was described as a rate controlled process driven



by this force, which was defined as the irreversible energy loss per unit area of newly created surface. This force, denoted by  $G$  ( after Griffith ) would have a critical value,  $G_c$ , when a crack starts to propagate.

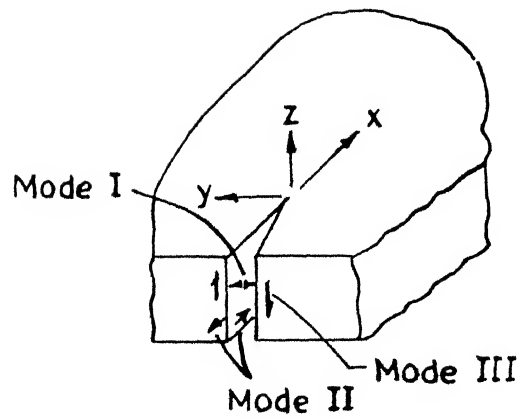
There is a strict equivalence between the strain energy release rate concept  $G$ , and the stress intensity approach for limited plastic deformation. Thus the techniques available for determining stress intensity factors are equally valid for determining  $G$ . However, in situations where extensive plastic deformation takes place prior to failure the relationship between an energy balance approach and a crack tip environment approach becomes more tenuous.

### 1.2.2 Stress Intensity Factor Approach to Fracture

The previous section discussed about the development of fracture mechanics on the basis of an energy balance approach. The fracture phenomena which focuses attention the mechanical environment near the tip of a crack was developed by Irwin and is generally known as the stress intensity factor approach.

#### a) Fracture Modes

In dealing with the stress intensity factor there are several modes of deformation that could be applied to the crack. These have been standardized and shown in Figure 1. Mode I, the crack-opening mode, refers to a tensile



F  
Fig. 1 Crack-deformation modes.

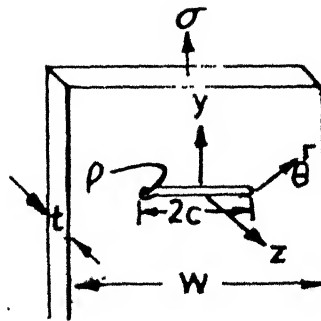


Fig. 2 Model for equations for stresses at a point near a crack.

stress applied in y direction normal to the faces of the crack. This is the usual mode for fracture toughness tests and a critical value of stress intensity determined for this mode would be designated as  $K_{Ic}$ . In engineering practice the importance of the opening mode I far exceeds that of the other modes. This work is limited to mode I unless specifically stated otherwise.

Irwin [6] laid the foundation for the important area of fracture mechanics. He proposed that fracture occurs at a fracture stress corresponding to a critical value of the crack-extension force, where equation(1) is rewritten as

$$\sigma_f = \left( \frac{KG}{\pi c} \right)^{1/2} \quad \dots (5)$$

$$G = \pi c \frac{\sigma^2}{E} \quad \dots (6)$$

G may also be considered the strain energy release rate i.e. the rate of loss of energy from the elastic stress field to the inelastic process of crack extension.

#### b) The Elastic Crack Tip Stress Field

Using Westergaard's [7] complex stress functions, Irwin [8] demonstrated that the elastic stress field near the tip of the crack in a infinite sheet could be described for mode I.

The stress distribution at the crack tip in a thin plate for an elastic solid in terms of the coordinates shown

in Figure 2 is given by the following equations:

$$\sigma_x = \sigma \left( \frac{c}{2r} \right)^{1/2} \left[ \cos \frac{\theta}{2} \left( 1 - \sin \frac{\theta}{2} \sin \frac{3\theta}{2} \right) \right] \quad 7(a)$$

$$\sigma_y = \sigma \left( \frac{c}{2r} \right)^{1/2} \left[ \cos \frac{\theta}{2} \left( 1 + \sin \frac{\theta}{2} \sin \frac{3\theta}{2} \right) \right] \quad 7(b)$$

$$\sigma_{xy} = \sigma \left( \frac{c}{2r} \right)^{1/2} \left[ \sin \frac{\theta}{2} \cos \frac{\theta}{2} \cos \frac{3\theta}{2} \right] \quad 7(c)$$

where  $\sigma$  = gross nominal stress =  $\frac{P}{wt}$  and these equations are valid for  $c > r > P$ .

Irwin pointed out that the above equations indicate that the local stresses near a crack depend on the product of the nominal stress  $\sigma$  and the square root of the half-flaw length. He called this relationship the stress-intensity factor  $K$ , where for a sharp elastic crack than infinitely wide plate,  $K$  is defined as

$$K = \sigma \sqrt{\pi c}$$

$K$  has the unusual dimensions of  $\text{MN/m}^{3/2}$  or  $\text{MPa}\sqrt{\text{mm}}$ . Using these definitions for  $K$ , the equations for the stress field at the end of a crack can be written

$$\sigma_x = \frac{K}{\sqrt{2\pi r}} \left[ \cos \frac{\theta}{2} \left( 1 - \sin \frac{\theta}{2} \sin \frac{3\theta}{2} \right) \right] \quad 8(a)$$

$$\sigma_y = \frac{K}{\sqrt{2\pi r}} \left[ \cos \frac{\theta}{2} \left( 1 + \sin \frac{\theta}{2} \sin \frac{3\theta}{2} \right) \right] \quad 8(b)$$

$$\sigma_{xy} = \frac{K}{\sqrt{2\pi r}} \left[ \sin \frac{\theta}{2} \cos \frac{\theta}{2} \cos \frac{3\theta}{2} \right] \quad 8(c)$$

values of  $K$  for many geometrical cracks and many types of loading may be calculated from the theory of elasticity. From the above discussion one can easily establish the relationship between 'G' the crack extension force and the

stress intensity factor 'K'

$$G = \frac{1+k}{8\mu} K^2 \quad (9)$$

where  $\mu$  is the shear modulus and

$k$  is a function of Poisson's ratio ( $\nu$ )

viz.  $K = 3 - 4\nu$  for conditions of plane strain

$$= \frac{3-\nu}{1+\nu} \text{ for conditions of plane stress.}$$

The above relationships show that the attainment of a critical extension force is equivalent to a critical stress environment. Fracture in this situation can be characterized by the attainment of a critical value of  $K$ .

Elastic analysis has shown that the stress environment around a crack tip was entirely similar to all situations to within a linear scaling factor. By means of tests on suitably shaped and loaded specimens it was possible to determine the material property  $K_{Ic}$  ( or  $G_{Ic}$  ) by defining it as the value of  $K_I$  ( or  $G_I$  ) operative at the point of fracture. The value of  $K_I$  at the point of fracture was found to be strongly dependent on plate thickness. Only after a certain thickness is exceeded critical value will be regarded as a material property.  $K_{Ic}$ , dependent only on the testing environment. The variation in the apparent value of  $K_{Ic}$  has been attributed to the through the thickness change in constraint along the crack front. The plastic regions that are near a free surface are practically in a

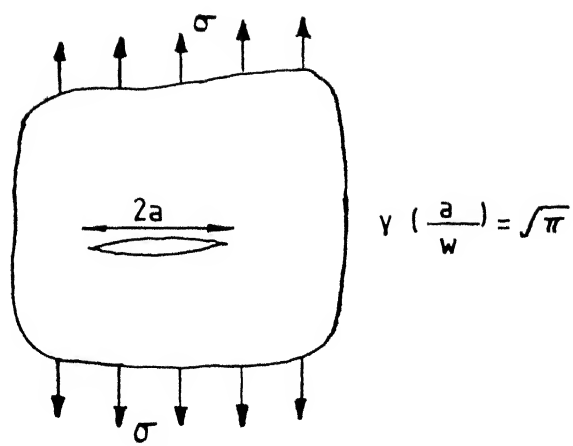
condition of plane stress whilst those remote from such a surface approach conditions of plane strain. When thickness is sufficient the fracture behaviour will be dominated by the region of constrained plastic deformation, a characteristic flat fracture will occur and conditions are described as 'plane strain'.

So far the basic philosophy of the stress intensity approach has been discussed without mentioning precisely how specific cases are dealt with. Obviously to interpret test results or to make design calculations, it is necessary to have explicit expressions for  $K_I$  for specific geometries and loading conditions. The determination of stress intensity factors is a specialist's task necessitating the use of a number of analytical and numerical techniques. It would be appropriate to discuss these in a separate chapter. The important point is that it is always possible to determine  $K_I$  to a sufficient accuracy for any given geometry or set of loading conditions.

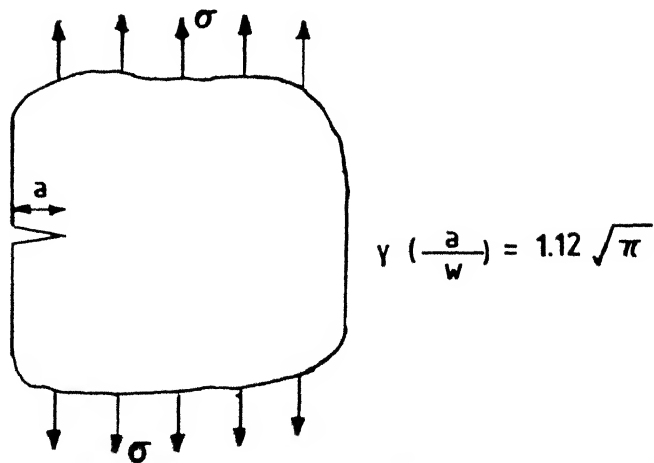
In general stress intensity factors may be written in the form

$$K_I = \sigma \sqrt{a} Y \left( \frac{a}{W} \right) \quad (10)$$

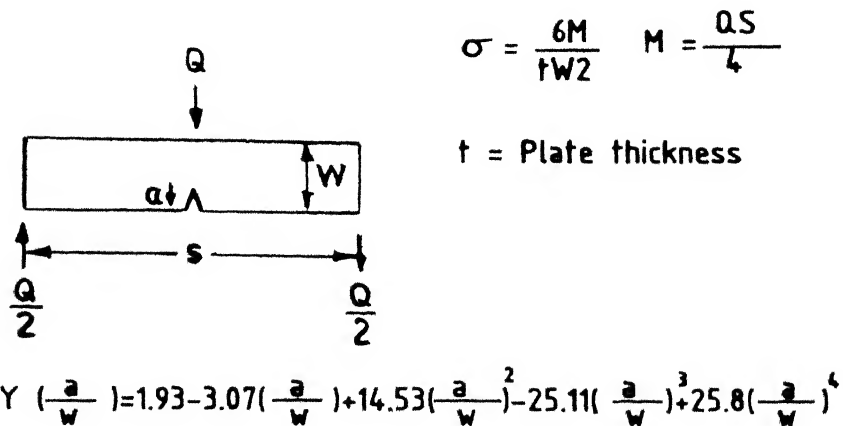
where  $\sigma$  is a characterizing stress  
 $a$  is a characterizing crack length  
 $W$  is a characterizing dimension



(a) Isolated crack in an infinite plate



(b) Surface crack in a semi-infinite plate



(c) Surface crack in three-point bend specimen

Fig. 3 Some crack configurations.

and  $Y\left(\frac{a}{W}\right)$  is a calibration function which defines  $K_1$  for the specific body under consideration.

Figure (3) shows three configurations with the corresponding values of  $Y\left(\frac{a}{W}\right)$ . Thus for example a fracture test on a three-point bend specimen would be interpreted by substituting the appropriate value of  $a/W$  in the polynomial for  $Y\left(\frac{a}{W}\right)$ . Figure (c) noting the load at fracture and thus determining the value of  $K_1$  at fracture. Alternatively, if it is necessary to estimate the maximum permissible depth of a surface defect in a thick component subject to uniform stress, use is made of the solution given in Figure 3(b). Here the stress intensity factor is given by

$$K_1 = 1.12 \sigma \sqrt{\pi a}$$

Consequently a knowledge of a critical value of  $K_1$  as determined by an appropriate fracture test, and the applied stress level permits the critical value of crack depth to be determined.

To summarize, the fracture event is interpreted as being characterized by the attainment of a critical value of the stress intensity factor,  $K_{1c}$ . Geometry and loading conditions influence this environment through the parameter  $K_1$ , which may be determined by suitable analysis. A knowledge of  $K_{1c}$ , obtained from a suitable test, thus provides a means of predicting the fracture behaviour in real structures. The sensitivity of structures to other phenomena



such as fatigue crack growth and stress corrosion cracking can likewise be predicted on the basis of suitably performed tests interpreted in terms of the stress intensity approach.

### 1.3 YIELDING FRACTURE MECHANICS

The prime objective of yielding fracture mechanics is to describe the fracture circumstances for a material of considerable ductility in the presence of a defect. As with other branches of fracture mechanics, a means is sought whereby fracture observed in the laboratory can be interpreted in terms of a material property, toughness. Just as in linear elastic fracture mechanics (LEFM) one approach is to characterize the singular stress, strain and displacement fields around the tip of a sharp crack by a single parameter so too in yielding fracture mechanics efforts have been made to find one parameter characterization of the elastic-plastic stress and strain fields local to the crack tip. It is argued, as in LEFM, that if such a parameter can be found, then for a given composition, temperature, strain rate and environment a process such as fracture supposed to be governed by circumstances at the crack tip, must occur when this parameter reaches a critical value.

#### 1.3.1. The Role of Extent of Plasticity

The notion of plastic constraint and associated terms such as small scale or contained yield and constrained or

unconstrained yielding into proper perspective, the different ways in which cracked component may fail when loaded beyond the range to which LEFM is applicable will now be surveyed briefly. A centre-cracked panel loaded in tension is taken as a simple example.

A stress very near to the crack tip (not specifically defined here but taken as representative of the local stress conditions) is denoted by  $L^\sigma$  the uniaxial yield stress by  $\sigma_y$ , net section stress by  $\sigma_n$  and the uniform stress remote from the crack by  $\sigma$ . It is useful to distinguish four regimes, which can loosely be described as follows.

- (a)  $L^\sigma > \sigma_y > \sigma_n > \sigma$ : Yielding limited to a zone in the immediate vicinity of the crack, to a very small extent. This is the LEFM problem. If failure occurs it is usually by unstable, rapid propagation of the crack.
- (b)  $L^\sigma > \sigma_y > \sigma_n > \sigma$ : Yielding is extensive but does not spread to a lateral boundary of the structure and thus contained. This is a regime that can be called elastic-plastic and to which yielding fracture mechanics can be applied. Failure usually occurs by unstable rapid propagation of the crack.
- (c)  $L^\sigma > \sigma_n > \sigma_y > \sigma$ : Yielding is very extensive and spreads to the lateral boundary ahead of the crack,

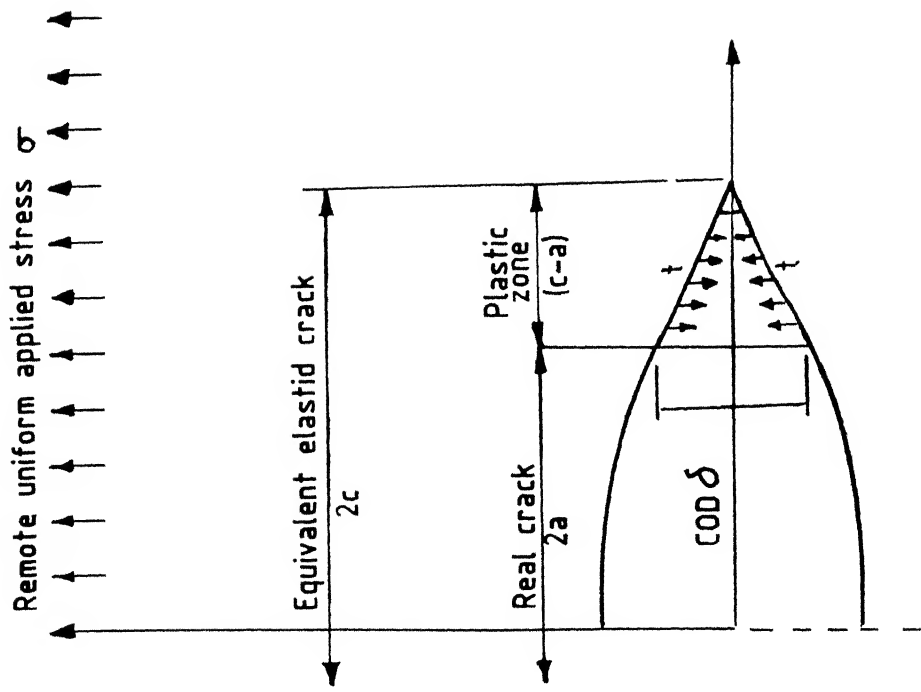


Fig. 5 The Dugdale model for crack tip plasticity.

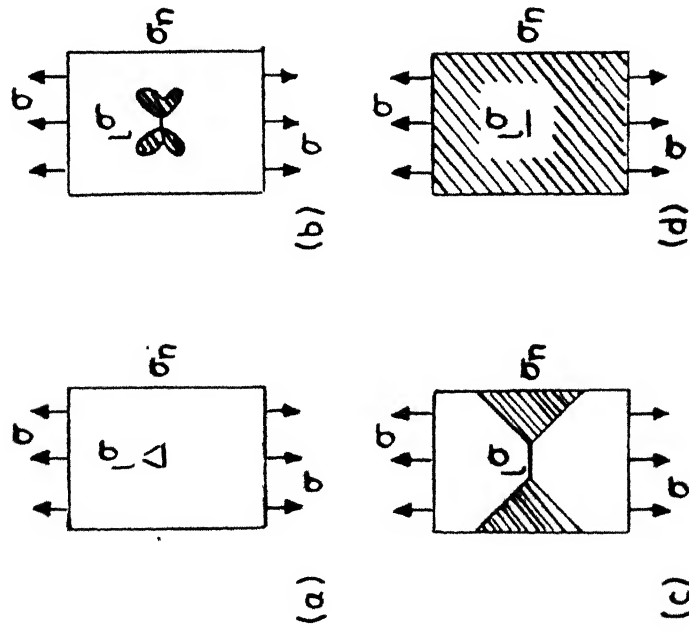


Fig. 4 Schematic representation of increasing degrees of yielding.

and thus uncontained. This is the regime that can be called gross yield, to which yielding fracture mechanics must be applied. For configurations with little lateral constraints and low hardening, tough materials may fail by plastic collapse of the net section, whilst for less tough materials a crack may spread by stable or unstable growth.

- (d)  $L^{\sigma} > \sigma_n > \sigma > \sigma_y$ : Since the applied stress  $\sigma$  is greater than the yield stress, extensive plasticity occurs along the components as well as the cross section implying work hardening of the net section. This is the regime that can be called general yield. Crack propagation in this case may still be the failure mode.

These four conditions are shown schematically in Figure 4. It must be clear that the stress levels used to describe the four states merge from one condition to the other and are affected by configuration, induced biaxial and triaxial stresses and work hardening. Clearly, the regimes starting in (b) and extending through (c) and for some materials into (d) are those that constitute the realm of yielding fracture mechanics of interest here.

### 1.3.2 Concept of Crack Opening Displacement (COD)

The method is based on the assumption- put forward independently by Wells [9], Cottrell [10] and Bavenblatt[11]

that where significant plasticity occurs the fracture process adjacent to the crack tip, and that the separation of the crack faces, or crack opening displacement will be a measure of the intense deformation. Crack extension will then begin at some critical value of this crack opening displacement, according to the particular micromode of fracture that occurs. Hence the method requires analytical prediction of displacements near the crack tip.

The model, proposed by Dugdale<sup>2</sup> [12] and Barenblatt [11] considers an infinite plate with a central crack, length  $2a$ , subjected to a remotely applied uniform stress. The plasticity at the tip of the crack is represented by a notional increase in the crack length to some value,  $2c$  with the faces of the 'crack' over the distance  $(c-a)$  from both ends partly restricted from opening by a restraining stress, ' $t$ ' acting directly on the crack faces. Later Wells [13] noticed that in practice the tip of a slot subjected to plastic deformation opened with a near square ended contour, giving a definite tip opening-the crack opening displacement - (COD) as in Figure 5. He proposed that the COD,  $\delta$ , was a measure of crack tip deformation and that fracture might occur when a critical value of this parameter  $\delta_c$  was reached. This proposal was pursued experimentally and theoretically by many scientists who have showed that it was broadly consistent with fracture results from large tension and bending tests.

In early applications of this model,  $t$  was equated to the uniaxial yield stress,  $\sigma_y$  and relationships obtained for the length,  $2c$ , to which the notional plastic zone extended in terms of the real length,  $2a$ , and the applied stress  $\sigma$

$$\frac{a}{c} = \cos \frac{\sigma\pi}{2\sigma_y} \quad (11)$$

The COD,  $\delta$ , at the tip of the real crack was then evaluated as

$$\delta = \frac{8\sigma_y}{\pi E} \log \sec \frac{\pi\sigma}{2\sigma_y} \quad (12)$$

By expanding the secant term it was found that

$$\delta = \frac{\pi\sigma^2 a}{E\sigma_y} \left[ 1 + \frac{\pi^2}{24} \left( \frac{\sigma}{\sigma_y} \right)^2 + \dots \right] \quad (13)$$

However renumbering the definition of strain-energy release rate in LEFM, for the infinite plate with centre crack  $2a$

$$G = \frac{K^2}{E} = \frac{\pi\sigma^2 a}{E} \quad (14)$$

It is at once seen that the first term in equation (13) corresponds to

$$G = \sigma_y \cdot \sigma \quad (15)$$

If the plastic zone correction factor for plane stress is used then the modified LEFM expression is

$$G = \frac{\pi\sigma^2 a}{E} \left[ 1 + \frac{1}{2} \left( \frac{\sigma}{\sigma_y} \right)^2 \right] \quad (16)$$

which together with equation (15) differs from the equation (13) by a fairly small amount in the coefficient of the second

term. The relationship  $G = t \xi$  is consistent with the work done to close an element of crack, from the reasoning of mechanics of either the macro or dislocation level, so that this model used with the restraining stress  $t = \sigma_y$  appears to be a logical extension to LEFM for plane stress.

Turning to the weaknesses in the model, the most obvious of these is the representation of plastic yielding by an elastic material with only a line of plasticity ahead of the crack. This is not unreasonable for plane stress, but unrepresentative for plane strain. For reasons that are not wholly apparent, the usage of the Dugdale model has retained the plane stress assumption of  $t = \sigma_y$ . It has in fact suggested that this inconsistency might be avoided through the use of a constrained yield stress

$$t = m \cdot \sigma_y \quad (17)$$

where  $m$  might be  $\sqrt{3}$  ( from plastic zone correction) or even as high as 3 for yielding material analysed for contained yielding.

Still by using these modified expressions for finding the fracture criteria there exists some discrepancies between theory and experiment. Thus the above model ignores the effect of a finite plate and of a work hardening material.

### 1.3.3 Concept of J-integral

Of the many parameters proposed to correlate elastic-plastic fracture behaviour, the J-integral as proposed by Rice [14] has been one of the most promising. The J-integral was used originally as an analytical tool for crack-tip stress and strain determination. It was first proposed as a fracture parameter, labelled  $J_{1c}$ , with supporting experimental method proposed was fairly cumbersome. Easier experimental methods for determining  $J_{1c}$  have been developed. A considerable amount of new work has been conducted both in supporting the use of  $J_{1c}$  as an elasticplastic fracture criterion and in developing the testing techniques for determining  $J_{1c}$ .

#### a) J-theory in General

The J-integral as proposed by Rice [14] is a two dimensional energy line integral (ref. Figure 6):

$$J = \int_{\Gamma} \left( W \, dy - T_i \frac{\partial u}{\partial x} \, ds \right) \quad (18)$$

where  $W$  is the strain energy density

$$W = \int_0^{\epsilon_{mn}} \sigma_{ij} \, d \epsilon_{ij} \quad (19)$$

$T_i$  is the traction vector defined by the normal  $n$  along the path of intergration, ,  $T_i = \sigma_{ij} n_j$ ,  $u$  is the displacement vector, and  $S$  is a length along. The J-integral is path independent and is applicable to elastic material or elastic-plastic material when treated by a deformation theory of plasticity.



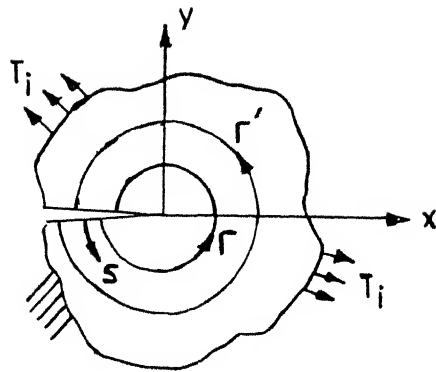


Fig. 6 Arbitrary contour over which J integral is evaluated

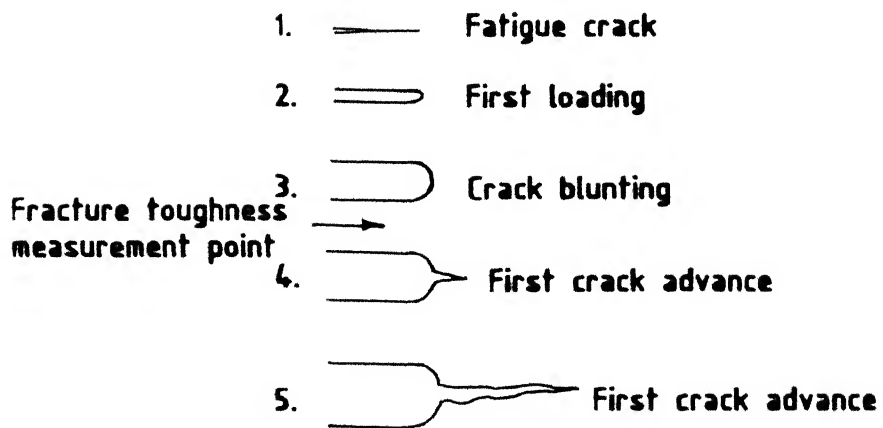


Fig. 7 Crack-tip schematic of the fracture process

The J-intergral characterizes the crack tip field the basis of which is provided by the work of Hutchinson 15 and Rice and Rosengren [16 ]. They have extended fracture mechanics concents to cases of large scale yielding which also assumed the crack tip singularity. They indicate that the product of plastic stress and strain approches a  $\frac{1}{r}$  singularity, r being a near tip crack field length parameter. The crack tip singularity is uniquely dependent on the material constitutive relations. For a deformation theory of plasticity McClintock [17 ]has demonstrated, through the crack tip plastic stress and strain equations expressed from the Hutchinson, Rice, Rosengren (HRR) singularity, the existence of singularity in r whose strength is the J-integral.

The J-integral has another important advantage as a fracture criterion. Broberg [18] considered growth criteria for a nonlinear elastic body containing a crack. For such a body, stress and strain singularities occur at the crack tip. This region ahead of the crack tip is termed as the end region outside which the material may be regarded as a continuum. As the load is increased, the end region eventually reaches a critical state at which the crack starts moving. one prominent feature of the end region at critical state is that the state is neither dependent on the distribution of loads nor on the crack length. It simply and solely depends on the material itself. The end region or plastic

zone can be specified by  $J_c$ , as it reaches the critical state.

From the foregoing discussion, it is evident that J-integral displays three prominent features attractive to its use as a fracture criterion namely,

- (i) J-integral as a field parameter indicates the stress and strain distribution in a cracked body.
- (ii) It describes the crack tip region by specifying the strength of the singularity.
- (iii) Critical value of J-integral,  $J_c$  is a material property which can be used as a fracture criterion.

The J-integral can be conveniently evaluated experimentally through its energy rate interpretation as follows. It may be noted that in equation (5) the two terms in the integral namely  $W$  and  $T_i \frac{\partial u_i}{\partial x_i}$ , have the dimensions of energy. Thus,  $J$  is an energy related quantity. In fact, Rice [14] has shown that the J-integral is equal to the change in potential energy for a virtual crack extension

$$J = -\frac{du}{da} \quad (20)$$

where  $u$  is the potential energy per unit thickness  
 $a$  is the crack length.

Equation (20) expresses an energy process where  $J$  is identical to  $G$ , the crack driving force. For the case of plastic behaviour where deformation is not reversible,

J loses its significance as a crack driving force. It can be considered as an energy comparison between two similar bodies identically loaded which have incrementally differing crack sizes. The line integral definition of J in Equation (18) is most useful for an analytical determination of J where numerical methods are employed. The energy rate interpretation is used for experimentally determining J. Equation (19) represents an exact method for experimentally measuring J, however, for most testing purposes, an approximation to Equation (3) is used.

b) Limitations of  $J_{1c}$  Approach

- (i) Since the Rice energy line integral is expressed only in two dimensions, the J approach is therefore, limited to problems of plane strain or generalised plane stress.
- (ii) Another limitation is that since J is shown to be path independent for deformation plasticity theory, the use of J as a fracture criterion should be compatible with the assumptions of deformation plasticity. This would restrict its use to monotonic loading and zero crack extension since any unloading cannot be treated by this theory of plasticity. Any crack extension necessarily implies unloading near the crack tip. In general, structures failing in plane stress exhibit some

subcritical crack growth. Hence, the J integral failure criterion may be limited to the case of plane strain which is implied by the subscript I in  $J_{1c}$ .

(iii) Also, since J is taken as the single parameter which characterizes the strength of the crack tip singular field equations, the size of the test specimen must be sufficient so that the crack-tip field equations are undisturbed by the specimen boundaries.

#### c) J as a Fracture Criterion

The fracture process starts with a sharp crack when the specimen or structure containing that crack is unloaded. For a test specimen the crack is introduced by fatiguing at a low  $\Delta K$  level before the fracture test is conducted. As the crack undergoes loading the crack tip becomes blunted. This blunting increases with an increase in loading until a load is reached where a crack advance occurs ahead of the original blunted crack (ref. Figure 7). At the point where the first crack advance occurs the fracture toughness measurement point is defined. In terms of J this point is labelled  $J_{1c}$ .

This model may not strictly characterize the actual physical process. Cracking may be ahead of the original blunted crack as voids are opened and joined. However, this model gives a general description of the fracture process which can then be related to a fracture parameter such as J. A physical application of the model is conceived more easily when cracking occurs in a ductile tearing mode.

#### 1.4 METHODS FOR FRACTURE TOUGHNESS MEASUREMENT

Standard test method for the determination of  $K_{Ic}$  has been approved by ASTM Ref. Standard Test Method for Plane Strain Fracture Toughness of Metallic Materials- ASTM Designation E399-74. The ASTM procedures have been divided so as to permit measurement of  $K_{Ic}$  and displacement (COD) under identical conditions with the same laboratory equipment and in the same test.

##### 1.4.1 $K_{Ic}$ Testing

###### (a) Type of Test Piece

Two main types of test pieces are recommended.

(i) Bend Test Pieces: These are the simplest and cheapest to machine. Limitations are imposed upon the test piece dimensions and the shape and depth of the notch. The pieces most commonly used have  $B = \frac{1}{2} W$ ,  $a = 0.45 W$  to  $0.5 W$ , where  $B$  is the thickness,  $W$  is the width and  $a$  the crack length of the specimen.

(ii) Compact Tension test Pieces: The specimen tension test pieces use less material, but the cost of machining the Clevis pinholes accurately is considerable. The recommended dimensions are  $B = \frac{1}{2} W$ ,  $a = 0.45$  to  $0.55 W$  and  $2F = 0.275 W$ . Please refer to Figure 8.

(b) Testing Fixtures

To reduce friction to a minimum, bend tests are made on freely rotating rollers with or without fixed centres. The diameter of the rolls and centre of loading point should be between  $\frac{1}{3} W$  and  $W$ .

(c) Test Piece Dimensions

The plane strain fracture toughness of a material is a measure of its resistance to unstable fracture under conditions where plastic deformation is limited to a region of the crack tip which is small in comparison to the test piece size, but the manner and the degree in which plasticity is to be limited is confirmed recently.

This is achieved by restricting the nominal stress at the crack tip to below the yield stress. The nominal stress is the stress that would exist at the crack tip if there were no stress intensification there.

In a compact tension test piece:

$$\sigma_{\text{nom}} = \frac{2Q(2W+a)}{B(W-a)^2} \quad (21)$$

and in a bend test piece:

$$\sigma_{\text{nom}} = \frac{3QL}{B(W-a)^2} \quad (22)$$

where  $Q$  is the applied load.

ASTM special committee has accepted the recommendation that the nominal stress should not exceed

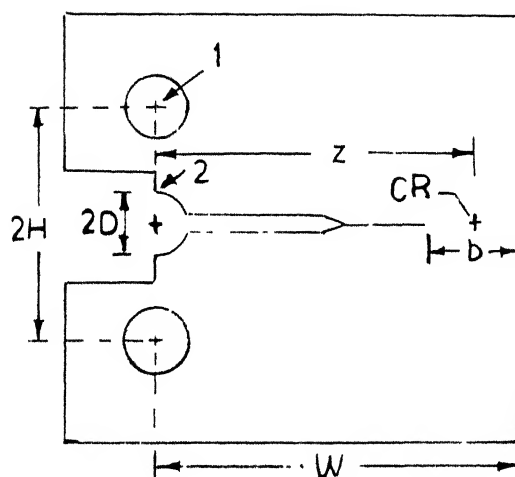


Fig. 8 Schematic of compact specimen 1, load point, 2, displacement point, CR, centre of rotation.



0 percent of the 0.2 percent proof stress.

Another requirement is that is to limit plastic deformation by maintenance of plane strain conditions at the crack tip. According to the standardized procedure to ensure plane strain ASTM 24, consistent  $K_{Ic}$  values could be obtained if

$$a, B > 2.5 \left( \frac{K_{Ic}}{Y} \right) \quad (23)$$

where  $a$  is the crack length

$B$  is the thickness of the test piece.

Moreover  $a/W$  values greater than 0.55 were considered undesirable because at high  $a/W$  values small errors in crack length can give rise to large errors in  $K_{Ic}$ .

#### (d) Fatigue Pre-Cracking

Basic requirements for the fatigue pre-cracking:

- (a) The ratio of minimum to maximum force shall be in the range of 0 to 0.1.
- (b)  $K_f$  shall not exceed  $0.7 (\sigma_{y1} / \sigma_{y2}) K_Q$  where  $\sigma_{y1}$  and  $\sigma_{y2}$  are the proof stresses at the temperatures of fatigue cracking and at the test temperature respectively.
- (c) The crack length shall be not less than 1.25 mm and the  $a/W$  ratio shall be in the range 0.45 to 0.55.

After testing the crack is measured and the effective crack length is measured from the average of three measurements at 25, 50 and 75 percent  $B$ .

(e) The Offset Procedure

$K_{1c}$  values were originally calculated from the pop-in load illustrated in Figure 9. Type IV since many materials do not exhibit pop in a procedure is established to determine  $K_{1c}$  values from force-displacement records showing deviations from linearity but no sudden discontinuity i.e. type I, Figure 9. The secant intercept procedure is adopted for this purpose.

The procedure is as follows. Referring to Figure 9 draw the secant line  $OQ_5$  through the origin with slope 5% less than the tangent  $OA$  to the initial part of the record. Draw a horizontal line representing a constant force of  $0.8 Q_Q$ ;  $q_1$  is the distance along this line between  $OA$  and the curve record. If this deviation from linearity at the force of  $0.8 Q_Q$  is more than  $1/4$  of the corresponding deviation,  $q$ , at the force of  $Q_5$  excessive non-linearity is present and so the curve is rejected.

So, for this situation the test piece of greater thickness should be selected and the experiment is to be repeated for  $K_{1c}$ .

(f) Calculation of  $K_{1c}$

The stress intensity factor at the tip of a crack of length  $2a$ , for the three point bending is given by

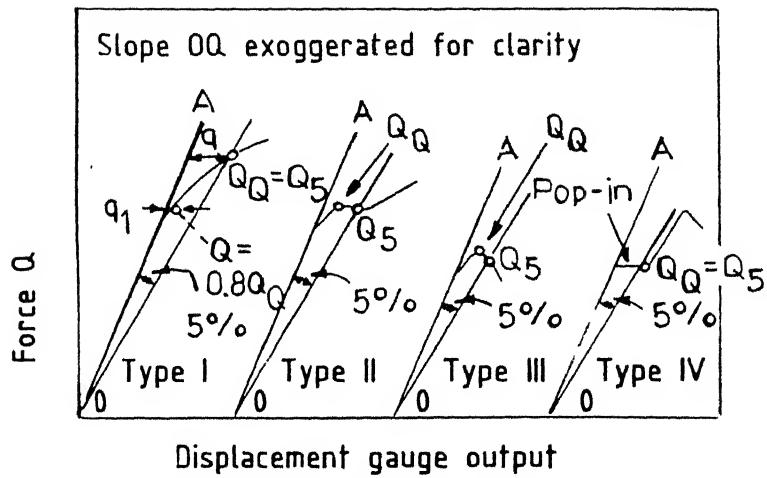


Fig. 9 Schematic force /displacement records showing quantities involved in analysis.

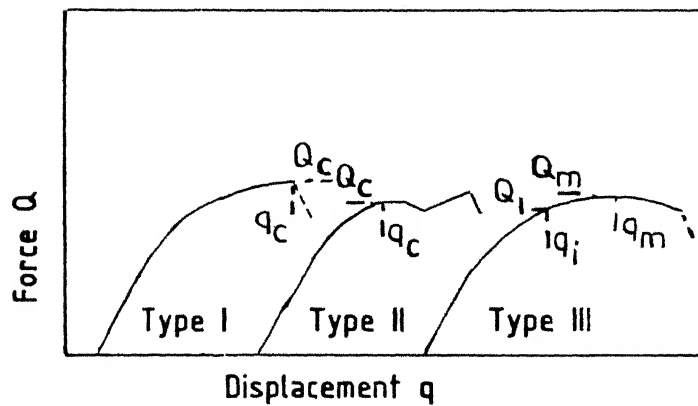


Fig. 10 Force /displacement records for calculation of COD

$$K = \frac{QY}{BW^{1/2}} \quad (24)$$

where Y is the compliance function derived from the relationship between test piece compliance and dimensionless crack length  $a/W$  i.e.

$$\begin{aligned} Y &= f\left(\frac{a}{W}\right) \\ &= 1.93 \left(\frac{a}{W}\right)^{1/2} - 3.07 \left(\frac{a}{W}\right)^{3/2} + 14.53 \left(\frac{a}{W}\right)^{5/2} - 25.11 \left(\frac{a}{W}\right)^{7/2} \\ &\quad + 25.80 \left(\frac{a}{W}\right)^{9/2} \end{aligned} \quad (25)$$

These values are given in tabular form for values of  $a/W$  between 0.45 and 0.55 in increments of 0.001 ( $a/W$ ).

The main objective of the COD test is to determine the critical crack opening displacement at the tip of a sharp crack at the onset of crack extension. This is done by measuring the displacement at the mouth of the notch using a gauge identical to the used in  $K_{Ic}$  tests and by performing a suitable calculation.

#### 1.4.2 COD Testing

The test record consists of a plot of force  $Q$  versus crack opening displacement at the notch mouth measured by a displacement transducer. A typical record is shown in Figure 10 where the critical displacement  $q_c$  at instability is the total value corresponding to the maximum applied force  $Q_c$ , Figure 10. In the case of type II, if the failing load portion can be shown to be associated with crack growth,

by electrical potential method or by an audible sound, then  $Q_c$  is measured at the discontinuity shown. The third type of record where there is no sudden discontinuity is associated with slow crack growth which commences during the rising portion of the test record. An electrical potential method must be used to detect at the initiation of stable crack growth  $\delta_i$ .

In those cases where crack growth cannot be measured the crack opening displacement  $\delta_m$  at the displacement  $q_m$  corresponding to the first attainment of a maximum load can be used.

#### 1.4.3 J-determination Techniques

##### i) Compliance J

The J-integral can be conveniently evaluated through the energy release rate interpretation of J as derived by Rice [14]. As explained earlier, J may be written for non-linear elastic material with no crack advance as:

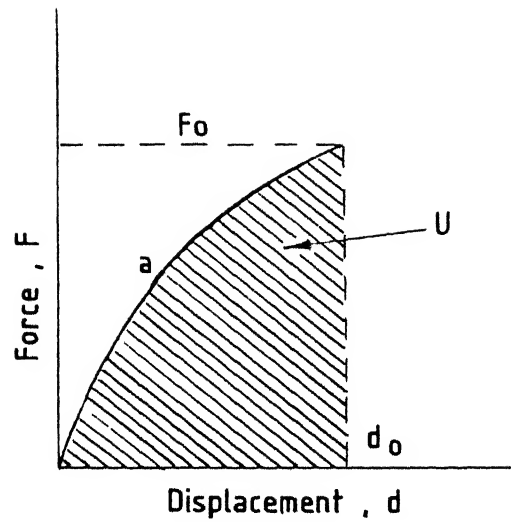
$$J = - \frac{1}{B} \frac{\partial u}{\partial a} = \frac{1}{B} \frac{\partial c}{\partial a} F \quad (26)$$

where F is the applied load

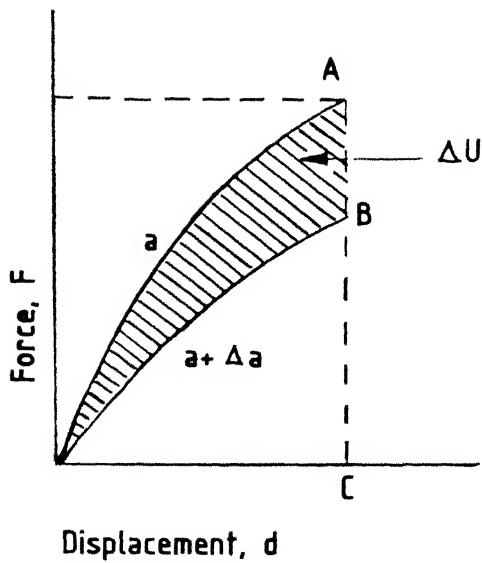
u is the load point displacement and

c is the complementary energy  $\int q \, dF$ .

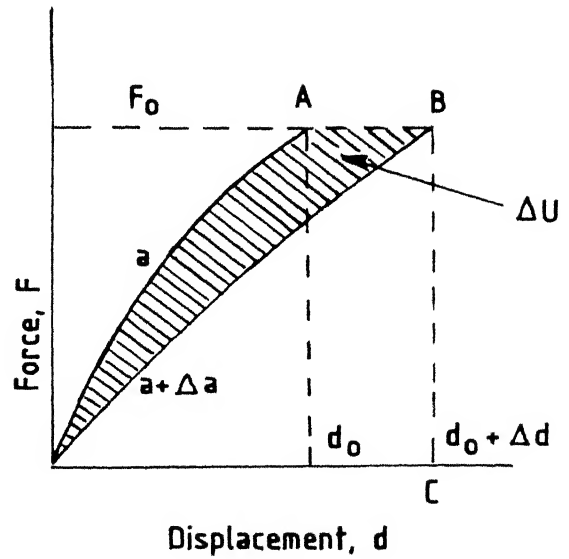
In the case of plasticity, where deformation is irreversible and J cannot be interpreted as the energy available to drive the crack, the contour integral J is numerically equal to



(a)



(b)



(c)

Fig. 11 Schematic load-displacement curves with prescribed load/displacement.

$$- \frac{1}{B} \left( \frac{\partial u_{el}}{\partial a} \Big|_u + \frac{\partial u_{pl}}{\partial a} \Big|_u \right) \quad (27)$$

This represents the energy difference for monotonically loaded cracks cut initially to different lengths.

Using equation (26)  $J$  may be experimentally evaluated as follows. For convenience displacements are prescribed as boundary conditions. Hence, the second term of the  $J$  integral in equation (18) drops out i.e., the potential energy becomes equal to the integral of the strain energy which is simply equal to the work done on the body.

The  $J$ -integral can be evaluated considering the load deflection diagrams of similar bodies with neighbouring crack sizes. When two similar bodies with crack lengths  $a$  and  $a + \Delta a$  are loaded, the load deflection curves are represented by  $OA$  and  $OB$ . If in the first body, the crack extends from  $a$  to  $a + \Delta a$  under prescribed load  $F_0$ , the total work done on the body is represented by the area  $OABCO$  (Figure 11(b)). Because of reversibility, the unloading curve from the point  $B$  is the same as the loading curve of the body starting with a crack length,  $a + \Delta a$ . The strain energy of the body with a crack length  $a + \Delta a$ , under the load  $F_0$  is the area  $OBCO$ . The shaded area  $OABO$  ( $-\Delta U$ ) is the energy available for crack extension. Similarly when the crack extends from  $a$  to  $a + \Delta a$  under prescribed displacements, the energy available for crack extension is the shaded area  $OABO$  (Figure 11(b)).

At any given displacement, the area under the load versus load point displacement record may be found for bodies with different crack lengths. The slope of the plot  $U$  versus ' $a$ ' at a given displacement is  $\left. \frac{\partial U}{\partial a} \right|_v$  and hence  $J$  can be determined. This process is shown schematically in the Figure 12. The final plot is  $J$  versus the applied displacement. In general, this curve depends on the crack length  $a$ . If the applied displacement is found for the initiation of crack growth, the critical  $J$  value,  $J_{1c}$  may be found.

## ii) $J_{1c}$ Testing Using Rice et al Estimation Procedures

A compliance determination of  $J$ , while possessing the advantage of generality, is tedious and expensive in both time and material and therefore is no longer used to determine experimentally. A significant advance in fracture toughness testing was provided by the development of the Rice-Paris-Merkle  $J$  formula for deeply cracked bars subjected to bending [19]. This same method has been made use of in our present study of the determination of  $J$  for the low alloy steel.

### a) The Rice-Paris Merkle $J$

The derivation of this formula is based on the fact that the angle of bend  $\theta$ , for deeply cracked bars, is only a function of the applied moment  $M$  and the square of the



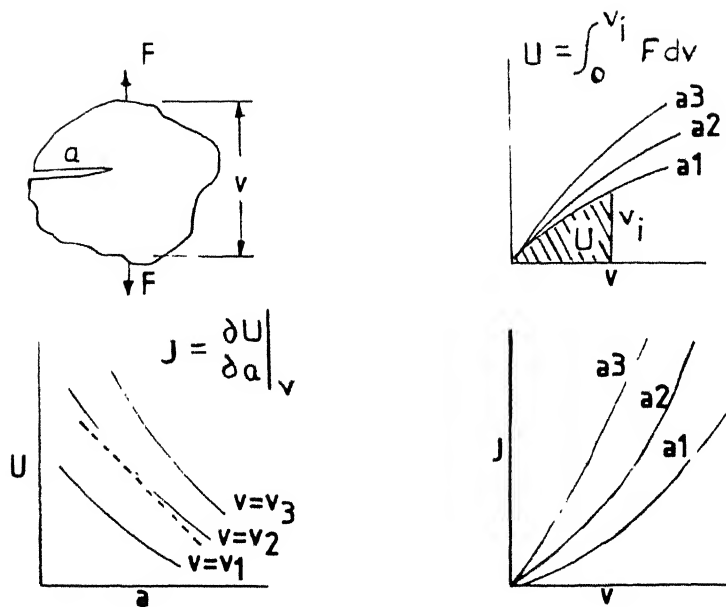


Fig. 12 Schematic of steps in a compliance  $J$  determination

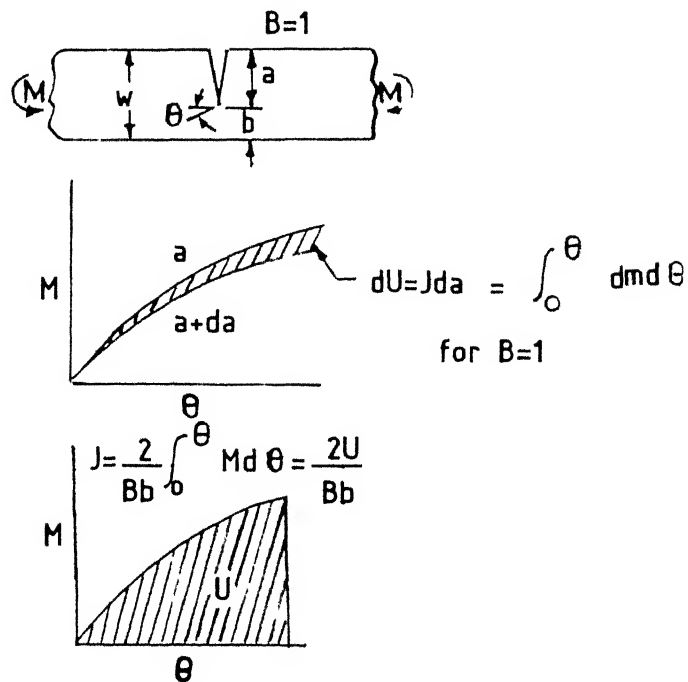


Fig. 13 Schematic showing Rice-Paris-Markle  $J$  formula for bend type specimen.

remaining ligament,  $b$  (Ref. Figure(13))

$$\Theta = f\left(\frac{M}{b^2}\right) \quad (28)$$

Using the potential energy definition of  $J$  given by equation (26) and the fact that  $da$  is equal to  $-db$ ,  $J$  can be written as

$$\begin{aligned} J &= \frac{1}{b_0} \int_0^\Theta \left. \frac{\partial \Theta}{\partial a} \right|_N dM \\ &= \frac{1}{B} \int_0^\Theta \left. \frac{\partial \Theta}{\partial b} \right|_M dM \end{aligned} \quad (29)$$

This is schematically illustrated in Figure.13. From equation (28)

$$-\left. \frac{\partial \Theta}{\partial b} \right|_M = -f' \left( \frac{M}{b^2} \right) \left. \frac{\partial (M/b^2)}{\partial b} \right|_M = \frac{2M}{b^3} f' \left( \frac{M}{b^2} \right) \quad (30)$$

Similarly

$$\left. \frac{\partial \Theta}{\partial M} \right|_b = \frac{f' (M/b^2)}{b^2} \quad (31)$$

and thus

$$\left. \frac{\partial \Theta}{\partial b} \right|_M = \frac{2M}{b} \left. \frac{\partial \Theta}{\partial M} \right|_b \quad (32)$$

Substituting equation (32) in equation (29)

$$\begin{aligned} J &= \frac{2}{bB} \int_0^M M \cdot \left. \frac{\partial \Theta}{\partial M} \right|_b dM \\ &= \frac{2}{Bb} \int_0^\Theta M d\Theta \end{aligned} \quad (33)$$

yields the result that  $J$  is simply related to the work done on the specimen. Again the above derivation holds true for deeply cracked bars in bending such that  $\Theta$  is only a function of  $M/b^2$ . The concept of relating  $J$  to the work done on the specimen is one that is used almost exclusively in present test methods.

b) Testing Procedure

From the discussion above, it is learnt that this method is based on the approximate formulation for calculating  $J$  given by Rice et al

$$J = \frac{2A}{Bb} \quad (34)$$

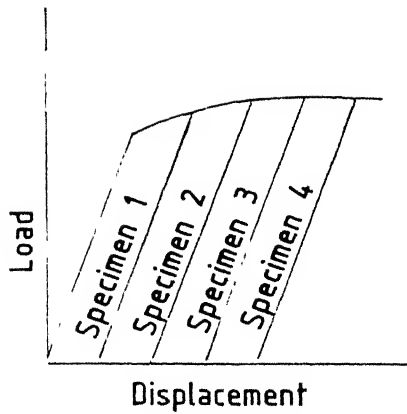
where  $B$  = specimen thickness

$b$  = remaining uncracked ligament of the specimen,

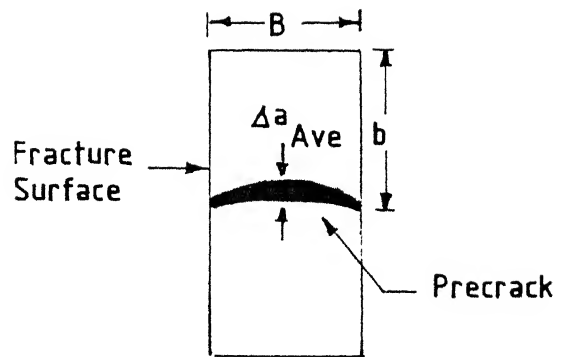
$A$  = area under the load versus load point displacement curve.

This formulation applied to a specimen with a deep crack subjected to a bend type of loading. The types of specimens most suited to this formulation are the compact toughness specimen (CT) and bend bars with three point loading.

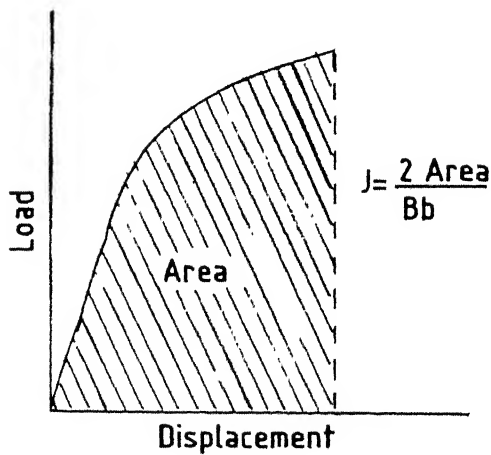
The method proposed for determining the  $J_{1C}$  measurement point is shown schematically in Figure 14. Several identical specimens are loaded to differing values of displacement and then unloaded (Figure 14(a)). These specimens will hopefully all exhibit different amounts of crack growth. After unloading, the crack advance is marked and



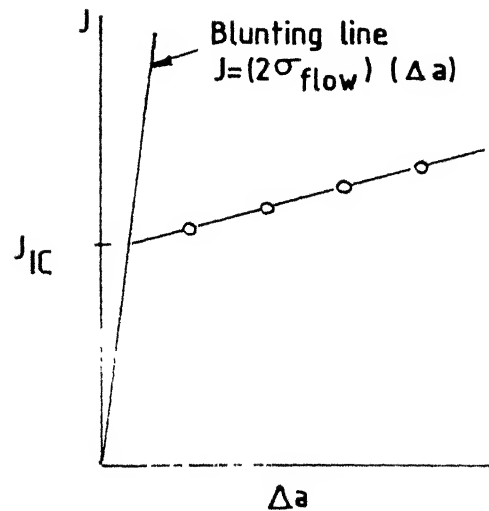
(a) Load identical specimens to different displacements



(b) Heat tint and measure average crack extension



(c) Calculate  $J$  for each specimen.



(d) Plot  $J$  vs  $\Delta a$  find  $J_{IC}$

14 Procedure for experimental  $J_{IC}$  measurement: multiple specimen R-curve.

the specimens broken open so that the crack advance,  $\Delta a$ , can be measured (Figure 14(b)). Different methods can be used to mark the crack advance. For steels the easiest method is heat tinting. The specimens are heated about 600°F for about 10 min. The specimens subsequently are broken open at liquid nitrogen temperature. The value of  $J$  at the point where the specimen is unloaded is determined from equation (20) for each specimen (Figure 14(c)). This value of  $J$  is plotted as a function of crack advance (figure 14(d)).

The curve in Figure 14(d) is the crack growth resistance curve from which  $J_{1c}$  is determined. The present method for determining  $J_{1c}$  uses the blunting line defined as

$$J = 2\sigma_{\text{flow}} \cdot \Delta a \quad (35)$$

the point where additional crack advance occurs from the blunted crack, that is, the  $J_{1c}$  measurement point, is marked by a change of slope in the curve of  $J$  versus crack extension. The points on the plot which lie to the right of the blunting line are generally fitted with a straight line and  $J_{1c}$  is taken at the intersection of this fitted line and the blunting line.

The method for determining  $J_{1c}$  as described by Figure 14 is presently used as standard method. Certainly some aspects of this method can be improved. Most notably

perhaps is the method of analysis the data points in Figure 14(d) to obtain  $J_{1c}$ . This analysis is somewhat subjective and can possibly lead to ambiguous values of  $J_{1c}$ . The use of the approximation formula from equation (34) has been compared experimentally with the original energy rate definition of  $J$ , equation (3) and found to compare favourably for  $a/W > 0.6$ .

#### Fatigue pre-cracking of Specimens

Specimens should be precracked in fatigue with a maximum permissible load not exceeding one fourth  $P_L$ , which can be calculated from the following

$$P_L = \left(\frac{4}{3}\right) \frac{B b^2 \sigma_{flow}}{S} \quad \text{for the bend specimen} \quad (36)$$

where  $b$  is uncracked ligament,  $B$  is the specimen thickness,  $S$  is the specimen bend span and  $\sigma_{flow}$  is the flow stress.

Fatigue cracking should be conducted at a sufficiently low load so that the crack tip is not overloaded. The  $J_{1c}$  test is expected to go into the plastic regime which means that specimen will most probably reach limit load.

#### c) Limitations of this $J_{1c}$ testing

One important limitation on the test method is specimen size needed to determine a  $J_{1c}$  value. This size limitation is generally expressed by

$$B, a \geq \alpha J_{1c} / \sigma_{flow} \quad (37)$$

where  $B$ ,  $a$ , are the specimen thickness, crack length respectively.  $\alpha$  is a non dimensional constant taken to be somewhere in the order of 25 to 50. These values in fact differ from one material to another depending on such things as the degree to which the material strain hardens.

Another important limitation on the use of the present  $J_{1c}$  test methodology lies in the specimen type. The approximation formula for  $J$  given by equation (34) has been formulated only for bend type specimens. Although approximations exist for other types of specimens, care should be exercised whenever a specimen other than a CT or bend bar is used.

#### 1.4.4 New Test Methods

With the use of equation (34)  $J$  can be determined for a single specimen at any given value of displacement. To determine the whole curve of  $J$  versus  $\Delta a$  hence  $J_{1c}$  from a single specimen all that is needed as a continuous monitor of crack advance during the generation of the load-displacement curve. Several methods have been demonstrated which can accomplish this successfully. They are namely elastic compliance method, electrical potential method and ultrasonic method.

## 1.5 THE SCANNING ELECTRON MICROSCOPE AND ITS APPLICATION TO FRACTOGRAPHY

The scanning electron microscope (SEM), although a relatively new instrument in the metallurgical laboratory, was derived from the early works in the field of electromagnetic, vacuum tube electronics, and vacuum pumping technology.

### 1.5.1 Principal Features of SEM [35]

A SEM is a combination of electron optical, vacuum, and electronic control devices for impinging a beam of electrons on a pinpointed spot on the surface of a target specimen and collecting and displaying the signals given off from that target. A typical arrangement of the components of a SEM for use in fractography is shown in Fig. 15. An electron gun emits electrons from a heated filament and accelerates them in a constant stream down the column. The specimen being examined is near the lower end of the column. As the electrons speed towards the specimen, they pass through two or more electromagnetic lenses that focus the stream of electrons into the shape of a small beam so that the impact spot on the specimen is of minimum size.

The electrons emitted from a specimen move to a suitable detector or collector and subsequently generate a current, which is amplified and used to control the brightness of spot on a cathode ray tube. The display image created on the deflection plates of the cathode ray tube. The fracture surface



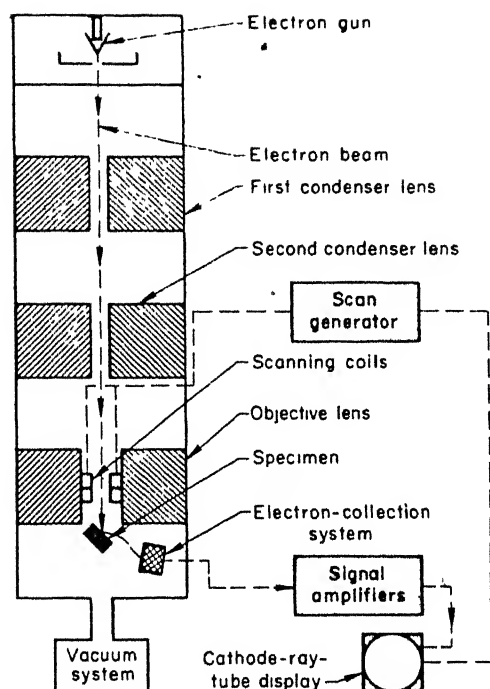


Fig. 15. Essential components of a scanning electron microscope (Ref. 37)

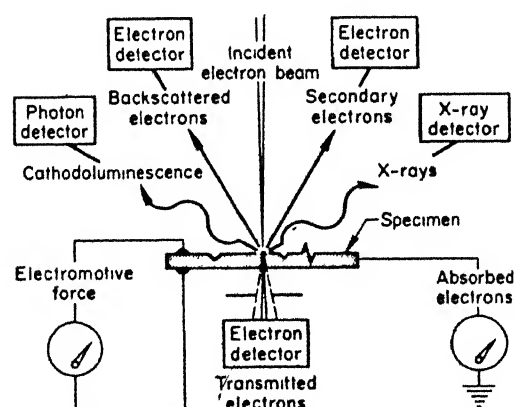


Fig. 16. Useful signals generated by an electron beam (Ref. 37)

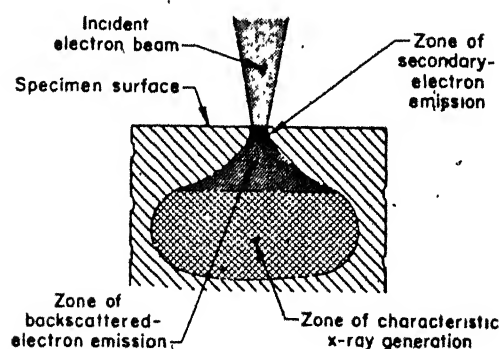


Fig. 17. Pattern of zones in a specimen (Ref. 37)

is scanned by the incident beam in a raster pattern, and the cathode ray tube displays the same pattern on a larger scale.

### 1.5.2 Operation of SEM [35]

When the fracture surface is impacted by the focussed stream of primary electrons, it emits several useful signals, such as backscattered and secondary electrons, cathodoluminescence, X-Rays and transmitted electrons; a fraction of incident beam of electrons is absorbed. The useful signals generated by the interactions of the incident beam with the specimen are illustrated in Fig. 16. From a fractographic standpoint, most interest is in the emitted secondary and reflected backscattered electrons.

Secondary electrons are almost always the preferred signal because they offer better resolution, produce an abundant signal, and permit viewing of areas of specimen that are not in a direct line of sight with the collector. This is the most generally useful type of image for studying surface-topography. It can also be made sensitive to crystal orientations, voltages and magnetic fields. The detector in this case is sensitive to electrons that emerge from the specimen with less than 50 eV energy.

Sometimes it is necessary to sacrifice resolution in order to improve image contrast, especially with smooth specimens and at low magnification. This is accomplished

by using the backscattered-electron mode of operation. This is obtained by collecting electrons that leave the specimen with more than 50 ev energy. Backscattered electrons possess high energy, travel at high velocity, and travel from specimen in straight line paths that produce shadow effects and consequently high image contrasts. The appearance of backscattered electron image will depend on the angle of incidence and on the the position and energy sensitivity of the backscattered electron detector.

There is a considerable loss of resolution in the backscattered mode of operation. Backscattered electrons are electrons with high energy. The electrons escape from as deep as 300 Å in the specimen. Because of scatter within the specimen, the resulting source is much larger in diameter than the incident beam diameter. On the other hand, secondary electrons escape from the top 100 Å layer of the specimen.

The relative quantity of secondary electrons versus backscattered electron captured by the electron collector is controlled by the use of a bias-voltage applied to the collector. If the bias voltage is made negative, the secondary electrons are repelled and the electrons captured will be essentially of the backscattered type.

The electron optical column must be operated at a pressure below  $10^{-4}$  torr. Higher pressure allow greater opportunity for oil vapor to flow back from the diffusion

Chromatic aberration can be regulated to fluctuations of less than 1 in  $10^{-5}$  volts by voltage stabiliser.

Stigmator correctors are usually provided on most high resolution instruments. These correctors simply superimpose, across the gap in the pole pieces, an additional weak elliptical field, which can be varied in strength and direction to compensate for the astigmatism, and is particularly valuable when contamination of the objective aperture occurs. One type consists of a nickel coated, brass, hollow cylinder which can be raised or lowered and rotated inside the objective pole pieces.

## 1.8 SOME HEAT TREATMENTS AND EFFECT OF IT ON FRACTURE TOUGHNESS

### 1.3.1 Normalizing Followed by Tempering [41]

In normalizing, steel is heated to a temperature  $30-50^{\circ}\text{C}$  above  $A_3$  temp in the austenite region and cooled in air. Cooling proceeds more quickly than in common annealing, which gives a somewhat greater degree of undercooling of austenite. Because of this, normalising produces a finer ferrite-pearlite structure. Normalized steel has a greater strength than the steel annealed.

Normalising is employed most often as an intermediate operation to soften the steel before machining, to eliminate

electrons, electron beam current, and the accelerating voltage in the column.

### 1.5.3 Specimen Preparation[36]

The main requirement of a specimen for examination by SEM is that it be of a size small enough to fit into the SEM chamber. This frequently requires sectioning of fractured part.

It is necessary that the specimen or replica for SEM viewing be electrically conductive to prevent electrical charging effects, which could distort the image. This is not a problem in fractographic study of metal surface unless a layer of corrosion products is present. Often, it is advisable to clean metal surfaces that are not fresh fractures and to remove extraneous material and anything that would outgas in the vacuum. Generally steel samples are mounted on Al stub with conducting paint. Silver particles are dispersed in medium of paint to produce an electrically conducting bond on drying.

Two of the most troublesome problems that the microscopist encounters are charging and beam damage. Charging occurs mostly on samples that are thick or have a loose, open structure. Charging effects can generally be attributed to inadequate coating. Thick samples tend to charge because it is difficult to metallize the vertical walls. This can be overcome by painting all the vertical faces with a

conducting paint, as described above, thus ensuring a good conducting path to ground. Reducing the beam current to a lower value also helps, but picture becomes noisier. Reducing the accelerating voltage also decreases the charging, but in many cases this is not pronounced, and the resolution becomes seriously impaired at low voltages.

#### 1.5.4 Unique Features

The SEM permits direct examination of the fracture surface without need for preparation of the thin films or surface replicas. It allows an initial assessment of the surface at relatively low magnification from an image that resembles the macroscopic appearance. This aids the interpretation of fracture features. The SEM also has the advantage of great depth of field.

A fundamental uniqueness of the SEM lies in the method of image formation. Unlike the transmission electron microscope (TEM), there is no magnification or image formation in the column of the SEM, the one function of the magnetic lenses being the production of an electron beam with as small a diameter as possible at the point of contact with the specimen. The information signal from the SEM is therefore a scalar quantity, actually a count of the photons or electrons leaving the spot on the specimen that is being impacted by the electron beam. This one dimensional signal is easily processed electronically and permits a complete

separation between the electron beam striking the specimen and the information signal.

#### 1.5.5 Production and Viewing of SEM Fractographs [37]

Following the initial visual inspection that is the first step in studying of any fracture, preliminary viewing of the fracture surface with a SEM may then be undertaken using the range of lower magnifications available i.e. from 5 to perhaps 50 diameters. In this perusal with the SEM one should appraise the probable mechanism of fracture and identify regions of the fracture surface for later reproduction as fractographs at appropriate magnifications.

#### 1.5.6 Defects and Limitations of SEM

Various kinds of aberrations are observed in electron-optical systems. Chromatic aberration arises because there is, in the electron beam as spread  $e\Delta V$  of electron energies about the mean energy  $eV_0$ . As a result, instead of obtaining a point focus, a disc of least confusion results with a diameter,  $d_c$ , which can be expressed by,

$$d_c = C_c \frac{\Delta V}{V_0} \alpha, \text{ where } \alpha \text{ is semiaperture angle at the image}$$

and  $C_c$  is chromatic aberration constant.  $C_c$  is determined by the nature of focussing field.  $\frac{\Delta V}{V_0}$  is the total fractional spread in electron voltage.

Spherical aberration arises from the use of finite numerical apertures because the electrons moving

on trajectories which are more inclined to the axis experience stronger fields and are more deflected. In this case, the diameter for the disc of least confusion is written as,  $d_s$  and is given by  $d_s \propto C_s \alpha^3$  where  $C_s$  is the spherical aberration const.

The 3rd fault - astigmatism - arises when the lens does not possess perfect rotational symmetry about its axis, i.e. focussing action depends on the plane with which we are concerned. The residual astigmatism can be expressed by,  $\Delta r_A = \Delta f \cdot \alpha$  where  $f$  = maximum difference in focal lengths.

Finally, there is a fundamental limit set by diffraction. In this case, diameter  $d_d$  of the Airy disc as the disc of least confusion where  $d_d = 1.22 \frac{\lambda}{\alpha}$

The four errors described above can be expressed as effective spot size,  $d_{eff}^{th} = (d_c^2 + d_d^2 + d_s^2 + d_a^2)^{1/2}$

Spherical aberration can not be completely removed because it is bound to occur even with a perfectly symmetrical lens and a completely monochromatic beam.

Chromatic aberration can reduce the resolution limit. It can be partly corrected by maintaining high tension stability, i.e., high voltage is maintained constantly and it is highly stabilized.



Astigmatism can be corrected by stigmators. Also by introducing electromagnetic lenses in some desirable directions it is possible to reduce astigmatism.

Care should be taken to ensure that all the signals recorded are within the working range of the film to get better resolution.

#### 1.6 ELECTRON MICRO PROBE ANALYSER AND ITS APPLICATION TO FRACTOGRAPHY. [38]

The electron microprobe analyser (EMPA) has been widely used for determining the chemical composition of constituents of the surface of the specimen. This instrument is capable of chemically analysing areas on a surface that are as small as 1 micron in diameter. The lower limit of concentration that the analyzer can detect is approximately 0.1% .

Use of an EMPA include : (a) identification of nonmetallic inclusions that may be present at the origin of a crack (b) analysis of the inclusions initiating microvoids in ductile dimpled fractures; and (c) analysis of corrosion or oxidation films.

Vacuum system are designed to minimise specimen contamination problems. Routine operating pressure in the column is  $10^{-6}$  torr.

### 1.6.1 Theory of Operation

An electron optical lens system produces an electron beam which is capable of being focussed to a point 1000 to 3000 Å in diameter. The impinging of the beam on a specimen will cause bound electrons to be ejected from the atoms and subsequent generation of characteristic X-Rays. The X-Rays are made to impinge on a crystal grating of known  $d$  (lattice) spacing and will be diffracted from the crystal in accordance with Bragg's law.

X- Rays are detected generally by use of proportional counter . The crystal and detector can be moved in relation to the specimen so that X-Rays of different wavelengths can be detected. The total system can be calibrated so that the wavelength of X-Rays being detected can be determined . Since every atom produces a unique characteristic X-Ray, determining the wavelength of the X-Rays unequivocally identifies the atoms present in the specimen. The range of element that can be identified with this technique is determined by the geometry of the instrument and  $d$ -spacing of diffracting crystal.

### 1.6.2 Modes of Data Presentation [39]

Direct compositional information can only be obtained from the X-Ray photons. The data may be

handled by the use of strip chart or X-Y recorder. In this case, intensity of X-Radiation is plotted against a second parameter. To determine the elements present in a specimen at a fixed point, one spectrometer would be varied while recording X-ray intensity as a function of spectrometer position (wavelength). From this plot it will be possible to determine the wavelength of all X-Rays present and in that manner identify all of the elements present.

In another case, any X-Ray entering the detector is converted into an energy pulse. It is in turn amplified, passed through a pulse height analyser, and stored in a scaling unit. Data are usually accumulated by counting X-Ray photons for a fixed length of time or by determining the length of time necessary to accumulate a fixed number of counts.

### 1.6.3 Specimen Preparation

In case of fractured specimen, no surface preparation can be performed. Generally for specimens of this type of interest is in a surface film or an inclusion on the surface. Specimens of this type can be evaluated qualitatively. The prime reason for this is that the surface is usually very rough and it would be very difficult to apply correction programs to the specimen. In preparing for the microprobe, the

specimen should be mounted so that the area of interest is as close to being normal to electron beam as is possible. It must also be ensured that no part of the specimen will block the area of interest from the detector.

X-Y recorder scan of intensity versus wavelength at a fixed point can be used for the identification of inclusion in a steel ingot. EPMA can be very useful in the examination of fracture surfaces.

These analysis will be discussed in detail in the next chapters.

#### 1.7 TRANSMISSION ELECTRON MICROSCOPY AND ITS APPLICATION TO FRACTOGRAPHY [33]

Transmission electron microscopy (TEM) is rapidly becoming a standard metallographic technique which few laboratories can do without. TEM has some features that are similar to those of SEM, but the principle of operation is different. The SEM concentrates electrons to a dense and as small a beam as possible, magnification of the image is performed by the relative raster scans of the specimen and cathode ray tube. The TEM, on the other hand, obtains magnification with the magnetic lenses below the specimen in the evacuated column; then the transmitted signal impinges directly

Specimens for TEM can be categorized into two groups, (i) those involving thin foils, 100  $\mu\text{m}$  or less in thickness for studies of quenched in defects, irradiation effects, dislocation interactions and diffusion (ii) (ii) wafers cut from bulk specimens for studies requiring direct comparisons between microstructure and physical properties.

Specimen is made anode in preparation from thin specimen in an electrolyte composed of an oxidizing agent and a carrier which removes metal ions from the specimen. After painting the edge of the specimen with an insulating lacquer to prevent preferential attack, a d.c. is impressed between the specimen and cathodes. The choice of electrolyte, temperature, and voltage is dictated by the material to be thinned. During polishing the ratio of the voltage to the current will vary. To establish optimum polishing conditions a plot of the current and voltage is first prepared. At lower voltages the current increases rapidly and the specimen is etching; a plateau is then reached where a further increase in voltage results in no increase in current. The best polishing takes place at the high end of the plateau.

#### 1.7.2 Preparation From Bulk Sections [38]

This requires that small sections be cut from the bulk material so that they will fit into the specimen holder.

After a small section has been obtained, the next stage is the initial thinning or dimpling of both sides of section. After the specimen has been dimpled, final polishing is performed in a specialized cell. Specimen is positioned between a light source and a detector which will interrupt the polishing action when perforation takes place. Holes less than 5  $\mu$ m in diameter in dimpled specimens can be detected and polishing can be stopped.

### 1.7.3 Artifacts in Specimen Preparation [38.]

They can arise during specimen preparation. The origin of artifacts may be attributed to polishing effects or changes which take place in the microstructure as thinning proceeds. One should be aware of the artifacts (e.g. formation of hydride or oxide layers) when interpreting precipitate structures, making accurate calculation of foil thickness and performing diffusion experiments in the microscope.

The choice of magnification depends on the size and characteristics of the surface features to be examined. If resolution of very small details is desired, high magnification is essential. Magnifications can be easily calibrated using replicas with standard grids.

The intensity of the image increases in direct proportion to the accelerating potential, varies inversely with the atomic number of the elements in a thin foil

specimen, or replica thickness. The intensity is also altered by tilting the specimen or replica, which introduces an effective change in thickness in the direction of electron beam travel.

#### 1.7.4 Application fo Thin Foil Techniques [38]

In order to obtain maximum amount of information from TEM, certain procedures or techniques which make microstructural features visible and identifiable must be employed, will be described in the following sections.

#### 1.7.5 Specimen Manipulation [ 38]

In order to get maximum information one must be able to control or change the specimen or foil orientation relative to the incident electron beam. Most electron microscopes today can be equipped with some type of goniometer stage.

#### 1.7.6 Selected Area Diffraction

Intermediate apertures may be inserted into the intermediate image plane so as to select any required portion of the image. The position of the intermediate apertures depends on the energizing current in the intermediate lens. This current has to be set to a fixed value so that when objective lens is focussed, the intermediate image and selecting aperture are coincident, i.e., when both the image and edge of the aperture are in sharp focus.

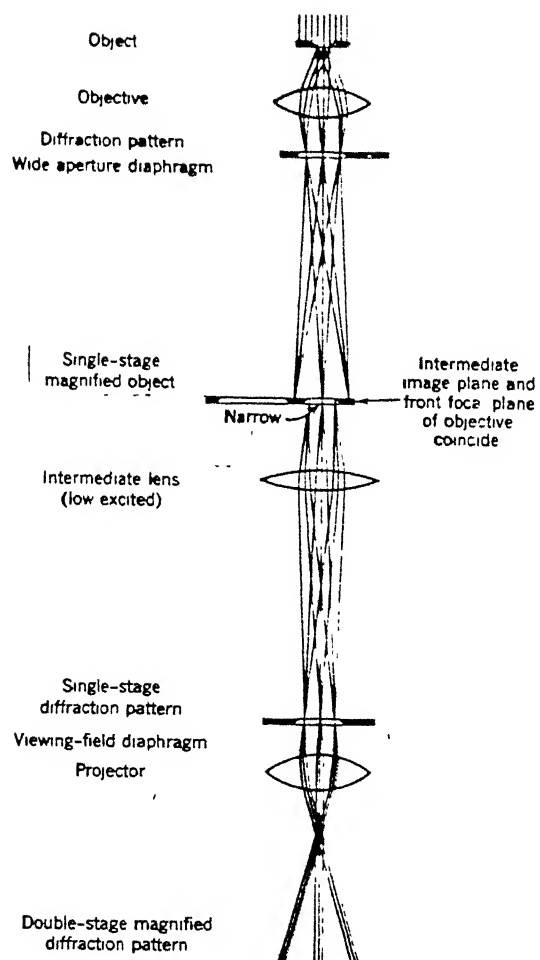


Fig. 18. Selected area diffraction pattern of the small area of specimen (Ref. 40)

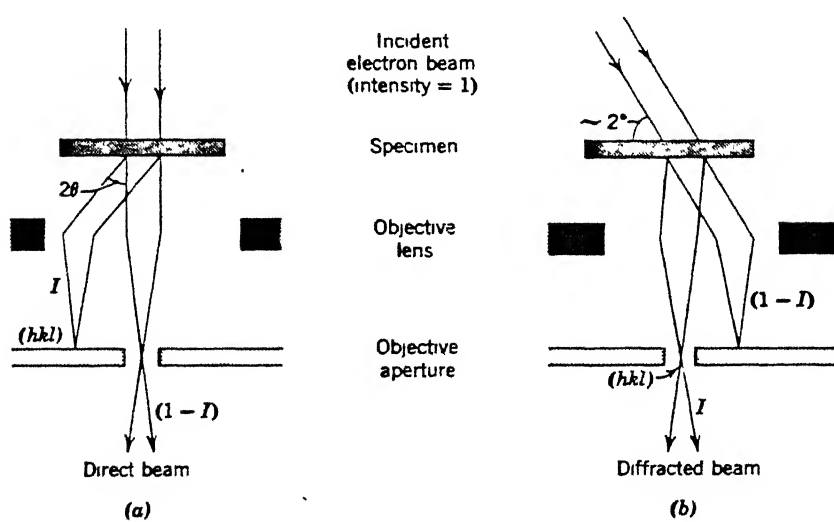


Fig. 19. Diffraction contrast  
(a) Bright field (b) Dark field  
(Ref. 40)



In the first image plane, the transmission electron diffraction pattern is formed.

One of the formula most useful for determining type of precipitate creating diffraction is  $dr = \lambda L$  where  $\lambda L$  = camera constant,  $d$  = lattice spacing,  $r$  = distance of transmitted spot from central spot.

#### 1.7.7 Bright and Dark Field Electron Microscopy

Contrast in bright field image is obtained by subtracting the intensity scattered into the Bragg reflections  $\{hkl\}$  from that of the direct beam.

Several advantages of dark field over bright field microscopy have been known for considerable time. For attainment of maximum resolution in the dark field, the diffracted beam must be coincident with the optical axis of the microscope. Originally this could only be done by tilting the gun; more recently, however microscopes have been equipped with electromagnetic coils which deflect the beam and simplify achievement of high resolution dark field. It must be realized that the operating reflection in dark field is the negative of that in bright field, so the beam must be filtered away from the theoretically analyzed.

#### 1.7.8 Applications of TEM [38]

Of great interest in metallurgy is the study of second phase or precipitates in metals. It is important to

know the size, shape, degree of coherency, strain field, and composition of the precipitates as well as its crystallographic relationship to the matrix. The ability to observe and distinguish precipitate in matrix by TEM depends on one or both of two basic factors, matrix and precipitate contrast. Matrix contrast arises from displacements in the matrix due to strain field of the precipitate. This is particularly useful for small precipitates. Precipitate contrast is due to the selective diffraction of the beam when passing through the particle.

Extensive information has been published in recent years on the identification of dislocation structures and interface structures such as stacking faults, twin boundaries and grain boundaries.

#### 1.7.9 Image Defects in Electron Lenses[40]

Spherical aberration is the only geometrical aberration which causes unsharpness of the image on the optic axis. This error corresponds to bad shaping of the lens surfaces such that a circle of confusion occurs about every image point. This error is same in principle like SEM. This can be reduced by using very small apertures in front of the objective lens. The higher the exciting current in the lens, the lower is the spherical aberration.

Chromatic aberration can be regulated to fluctuations of less than 1 in  $10^{-5}$  volts by voltage stabiliser.

Stigmator correctors are usually provided on most high resolution instruments. These correctors simply superimpose, across the gap in the pole pieces, an additional weak elliptical field, which can be varied in strength and direction to compensate for the astigmatism, and is particularly valuable when contamination of the objective aperture occurs. One type consists of a nickel coated, brass, hollow cylinder which can be raised or lowered and rotated inside the objective pole pieces.

## 1.8 SOME HEAT TREATMENTS AND EFFECT OF IT ON FRACTURE TOUGHNESS

### 1.8.1 Normalizing Followed by Tempering [41]

In normalizing, steel is heated to a temperature  $30-50^{\circ}\text{C}$  above  $A_3$  temp in the austenite region and cooled in air. Cooling proceeds more quickly than in common annealing, which gives a somewhat greater degree of undercooling of austenite. Because of this, normalising produces a finer ferrite-pearlite structure. Normalized steel has a greater strength than the steel annealed.

Normalising is employed most often as an intermediate operation to soften the steel before machining, to eliminate

structural defects, or to produce a general improvement in its structure before hardening.

Normalizing is applied mainly to plain carbon and low alloy steels. To reduce the increased hardness of normalised steel and to relieve the internal stress, normalising is followed by high tempering ( at 500 to 630°C). In high tempering coagulation and spheroidising processes take place in a steel.

Generally speaking, a fine grained steel has a lower transition temperature range with improved toughness than a coarse grained one.

### 1.3.2 Quenching Followed by Tempering [ 41]

Quenching consists in heating to a temperature from 30 to 350°C above point  $AC_3$  for hypoeutectoid steels or above point  $AC_1$  for hyperertectoid steels, holding untill phase transformations are completed and then cooling at a rate above the critical. Carbon steels are commonly quenched in water, alloy steels in oil or other media. Hardening by quenching is not a final heat treatment. It must be followed by tempering to reduce the brittleness and stress due to hardening and to obtain the required mechanical properties.

Heating time should be sufficient to heat the work throughout its cross section and to enable the phase

transformations to be completed, but should not be so long that it leads to grain growth and decarburization of the surface layer of steel. Generally for steel consisting of 0.1 to 0.5% carbon, heating is done for one hour for each inch of diameter or maximum thickness.

It is most desirable to provide a high cooling rate (above the critical cooling rate) in the temperature range from  $A_1$  to  $M_s$  to suppress supercooled austenite decomposition in the regions of the pearlite and intermediate transformations and slower cooling in the temperature range of martensite transformation from  $A_s$  to  $M_f$ .

Water, aqueous solutions of salts and oils are generally used as quenching media. In quenching carbon and certain low alloy steels having low stability of supercooled austenite, water or aqueous solutions of NaCl or NaOH are used as quenching medium. Mineral oils (usually petroleum type) are used in hardening alloy steels, which have high stability of supercooled austenite.

### 1.3.2 Tempering of Steel

Tempering consists in heating hardened steel to a temperature below point  $AC_1$ , holding at the given temperature and subsequent cooling at a definite rate

Low temperature tempering is performed by heating to  $250^{\circ}\text{C}$  with holding time 1 to 2.5 hours employed. This reduces the internal stress, the martensite is transformed to tempered martensite, the strength and wear resistance are increased and toughness is improved slightly without any appreciable loss in hardness.

Medium temperature tempering at  $350^{\circ}\text{C}$  to  $500^{\circ}\text{C}$  is employed chiefly for coil and laminated springs, as well as for dies. This operation provides high elastic limit, endurance limit, and resistance to relaxation. After tempering, work should be cooled in water. This promotes the development of compressive residual stress at the surface, which raise the endurance limit of the springs.

High temperature tempering is performed in the range from  $500^{\circ}\text{C}$  to  $680^{\circ}\text{C}$ . This operation provides for the best combination of strength and toughness of the steel. This operation raises the tensile strength and yield point reduction in area, especially toughness. For this reason this operation is called structural improvement.

#### 1.3.2.2 Temper Brittleness

As the tempering temperature of hardened carbon steels rises, their impact strength (toughness) continually increases. But two minimum of impact strength are generally

observed at about  $300^{\circ}\text{C}$  and  $500^{\circ}\text{C}$ . The first one is known as temper brittleness of first kind and second one is called temper brittleness of second kind.

The second kind is peculiar to alloy steels. The most radical means of eliminating temper brittleness of second kind, which is characteristic of alloy steels are high tempering around  $600^{\circ}\text{C}$  and rapid cooling, alloying with molybdenum in Chromium-Nickel or Chromium-Manganese steels, reduction of impurities because they can weaken the intergranular bondage. Brittleness is associated with reversible segregation of impurities along the grain boundary in a manner prejudicial to impact toughness.

### 1.8.3 Martempering [42]

This hardening method consists in heating the steel to the hardening temperature, quenching it in a medium having a temperature somewhat above point  $M_s$ , holding until the temperature throughout the cross-section is subsequently uniform, then cooling at a moderate rate to prevent large difference in surface and centre. The amount of residual austenite is much larger than in continuous hardening, resulting in less volume change. Alloy steels, which have a lower critical cooling rate, are more suitable for martempering.

#### 1.8.4 Austempering [42]

By applying this treatment, it is possible, in certain cases, to obtain greater toughness than that obtained after conventional hardening and tempering to the same hardness. There are no excessively large or harmful stresses induced in the tools and consequently distortion is small. As in the case of martempering, the parts to be hardened are quenched in a salt bath, the temperature of which is kept above that of martensite formation. The holding time in the bath, however, is so long that the austenite is completely transformed to lower bainite. The resulting hardness depends upon the temperature of the salt bath; a high temperature gives low hardness. Austempering generally improves toughness, particularly in that hardness range in which conventionally hardened and tempered steel are susceptible to a reduction in their impact strength. No tempering is required.

#### 1.9 NON-METALLIC INCLUSIONS IN STEEL AND THEIR EFFECTS ON FRACTURE TOUGHNESS.

The formation, mode of occurrence and type of the sulfide inclusions observed in steel is an extensive topic, as also are the influence of non metallic inclusions (N.M.I) in steel on the properties continues to be a major study by many metallurgists.



In general, nonmetallic inclusion in steel fall in to two major categories, namely oxides and sulfides, although several minor type os inclusions may be present.

By virtue of their mode of formation, non metallic inclusions are seldom, if ever, equilibrium products. The composition, and hence the constitution of an inclusion, may alter during reheating or slow cooling, by reaction with steel. This can occur in both sulfides and oxides.

#### 1.9.1 Sulfides in Steel

Sulfides in steel generally comprise of one or more of the phases,  $\text{FeS}$ ,  $\text{MnS}$ ,  $\text{CaS}$ . Frequently there can be extensive solid solution of other elements in the sulfide. In recent years, considerable attention has also been focussed on sulfides of titanium, zirconium and rare earth metals.

It is very evident that at normal steel solidification temperatures, the tendency to form  $\text{MnS}$  is only slightly greater than the tendency to form  $\text{FeS}$ ; above  $1600^{\circ}\text{C}$  the tendency is reversed, when the lower manganese activity is considered. Obviously, however, whilst the difference is small at steel solidification temperatures and concentrations,  $\text{MnS}$  is the more stable phase at much lower temperatures. In contrast, assuming unit activity of manganese,  $\text{FeS}$  should never be formed when manganese is present, until all the manganese has formed  $\text{MnS}$ . But this situation is not observed

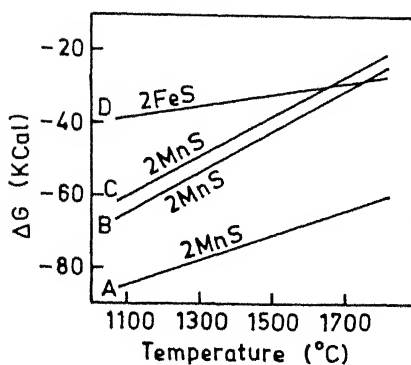


Fig. 20. Free energy of formation of MnS. (Ref. 53)

Reaction : Solid Mn or Fe + gaseous S

A.  $\alpha_{\text{MnS}} = 1.0$ ; 100% Mn melt

B.  $\alpha_{\text{MnS}} = 0.5$ ; 1% Mn melt

C.  $\alpha_{\text{MnS}} = 0.5$ ; 0.5% Mn melt

D.  $\alpha_{\text{MnS}} = 1.0$ ; 100% Mn melt

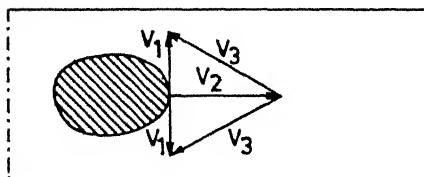


Fig. 21. Schematic indication of crack formation at the metal/inclusion interface, causing a conical gap (Ref. 52)

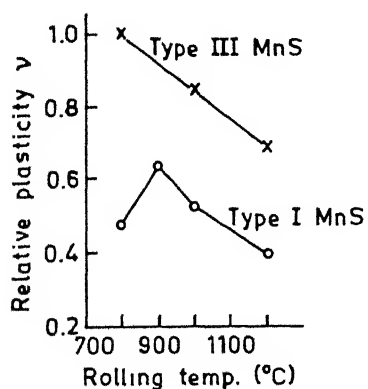


Fig. 22. Effect of rolling temperature on the relative plasticity of MnS (Ref. 53)

in practice, according to Kiessling [43] .

Three different from of MnS-type I, type II, type III are commonly found in steel. The morphology can generally be described as globular, branched rod and elongated or idiomorphic for type I,II, III respectively.

#### 1.9.2 Deformability of Steel Inclusions [43]

The plasticity of inclusions, as compared to plasticity of steel phase, has a strong influence on the behaviour of steel. If the steel phase and the inclusions are not working together during all the steeworking operations, the inclusions will be a potential source of future defects. This is one of the reasons why a knowledge of the metallography of the inclusions is so important.

Scheil & Schnell [44] and Pickering [45] in his studies of the effect of hot working on various types of inclusions, measured the deformation of the inclusions in rolled bars on microsections parallel to the rolling direction, where the deformed inclusions were visible as elongated ellipses.

According to Rudnik, [46, 47], for a deformability index close to 1 the inclusions lengthen in the same way as the steel. The binding forces at the inclusions/steel interface are never broken, and the inclusions appear in microsections as ellipses without the occurrence of

discontinuities in the steel caused by the inclusions. If the index of deformability decreases, the inclusion do not elongate uniformly during rolling of the steel. Stresses are built up at inclusion/ Steel interface which may lead to cracking. In principle, cracking occurs between the inclusion and steel perpendicular to the flow of the steel. However, the direction of the cracks is determined by the simultaneous flow of the steel, leading to the formation of conical gaps at the inclusion/steel interface, as shown in Fig. 21. The base of the cone is resting on this interface and the apex pointing in the direction of steel flow. The size of the conical gap depends on the inclusion plasticity, on rolling temperature, and rate of deformation. Due to the compressive stresses in the steel phase perpendicular to the direction of flow, the conical gap may be filled with steel leaving only the cracks, but if the steel is cold worked, the conical voids may be unfilled. Rudnik concluded from experimental evidence that inclusions with  $\gamma = 0.5-1$  deformed normally with a low frequency of microcracks in the inclusion/ steel interface. Those with  $\gamma = 0.03-0.3$  often gave fish tails with conical gaps, more frequently in the lower range of  $\gamma$ . For undeformed inclusions ( $\gamma = 0$ ) conical gaps and hot tears were frequently observed. The work of Rudnik indicates that this index should preferably be  $\gamma = 0.5-1$ . The inclusion phase should not be molten at hotworking temperature as it

then deforms to thin films which flow away (hot tearing).

It has been suggested that voids form at inclusions if  $\nu < 0.5$ . Initial void is much smaller than inclusion and growth occurs mainly in the direction of principle tensile stress. However, except in steels with high concentration of sulfides, other inclusions such as silicates are much more dangerous than sulfides in terms of void initiation and possible link-up leading to fracture.

The influence of temperature on the deformation of MnS inclusions in steel can also be seen from Fig. 22. The deformability apparently increasing progressively from type I to type III.

The relative plasticity increases on both type as rolling temperature decreases from  $1200^{\circ}\text{C}$ , but whereas with the type III the trend continues to  $800^{\circ}\text{C}$ , with the type I a maximum is encountered at  $900^{\circ}\text{C}$ . The increase in relative plasticity with the decreasing temperature reflects an increased rate of hardening of matrix relative to that of MnS. The change to a decreased plasticity below  $900^{\circ}\text{C}$  is apparently due to transformation of austenite to ferrite.

Depending on the Mn: S ratio of steel and rate of cooling, MnS can contain variable and often large amount of FeS in solution. Diffusion may then occur during subsequent reheating, to produce MnS which is virtually free

from Fe. In general as the degree of deoxidation increases, the sulfide morphology changes from globular type I, through the eutectic like type II to the angular type III. Other factors, like carbon seems to be very effective in producing angular type III MnS.

### 1.9.3 Hot Shortness

Hot shortness in steel is its tendency to brittle fracture in the hot forming temperature range. This phenomena has been attributed to sulfur, but oxygen has also been considered at least to enhance the effect of sulfur, whereas it is well known manganese counteracts hot shortness. The failure of steel is related to its sulfide inclusions, and in its original and pronounced form, hot shortness is caused by the precipitation of FeS in the austenitic grain boundaries of the steel.

If iron has Mn in solution, which is the case in almost all commercial steels, the solid solubility limit for sulfur in the  $\gamma$ -phase is considerably lowered. This is shown in Fig. 23. The lower amount of sulfur in solid solution will then result in a lower resistance to dislocation movements within the metal matrix. Secondly the sulfur will be bound to manganese instead of iron and precipitated as MnS if the manganese activity is high enough. MnS has a higher melting point than FeS ( $1610^{\circ}\text{C}$ )

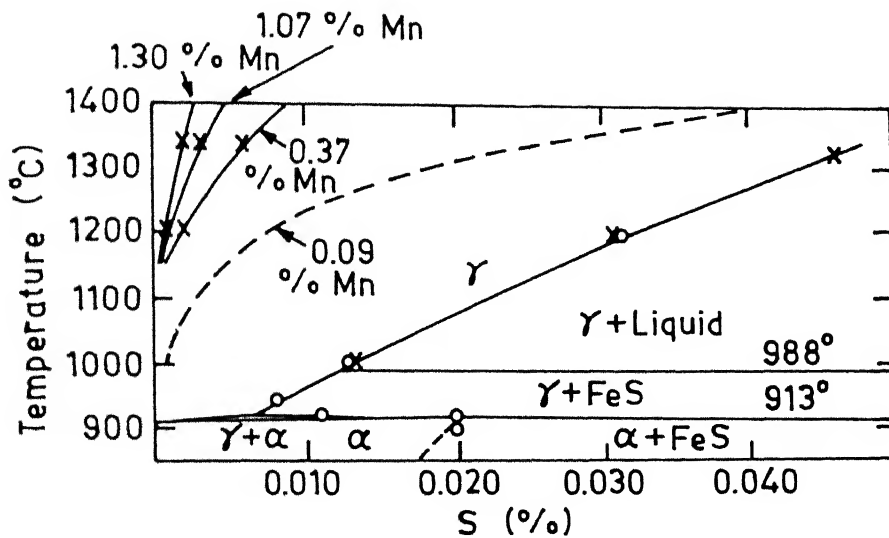


Fig. 23. Part of Fe-S phase diagram (Ref. 52)

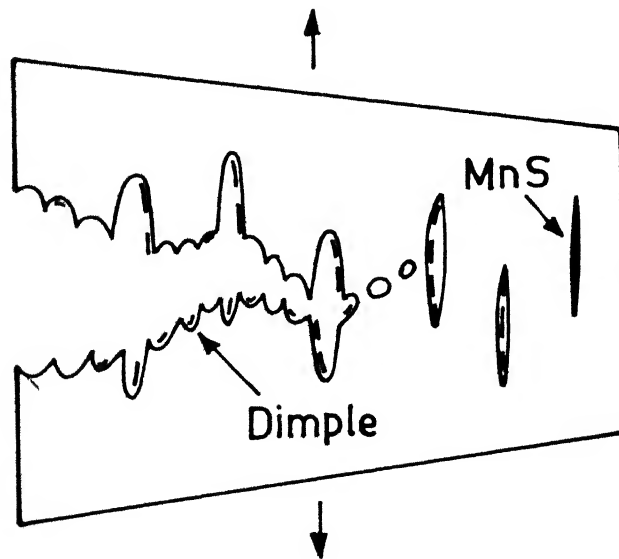


Fig. 24. Mechanism of the ductile fracture when elongated MnS inclusions are involved (Schematic), Ref. 53

and the possible MnS entectics also have higher melting points than those with FeS. The shear strength of the grain boundaries is therefore not decreased as much as with FeS and hot shortness may be avoided if the manganese concentration is high enough. Manganese therefore counteracts hot-shortness in two ways by neutralizing both the two embrittling mechanisms attributed to sulfur. Presence of Oxygen can form (Fe,Mn) O inclusions, thereby lowers the effective manganese content, thus promotes hot shortness.

#### 1.9.4 Influence of Inclusions on Mechanical Properties[52]

The dependence of mechanical properties on the microstructure has been known for many years. Work on strength-structure relationships was broadened to cover impact properties, and in recent years attention has been focussed on the effects of microstructure on ductility, which is an important property in connection with metal forming operations such as bending, and is also related to toughness as expressed by the ductile shelf energy.

In recent years, increasing attention have been paid to the influence of microinclusions on crack formation and crack propagation in the steel.

Hull [50] has shown cleavage crack can form by undeformed spherical inclusion ( $\gamma = 0$ ) where the inclusion is effective in concentrating the plastic deformation.



The formation and propagation of cleavage cracks occurs along the axis of tension. Although these observations were all made on single crystals of iron-silicon deformed on tension, a similar analysis in polycrystalline steel is possible.

MnS, as earlier discussed, with  $0.5 < \lambda < 1$ , usually deforms plastically with the steel. They should not be expected to cause crack formation, although they act as stress raisers in the slip planes of the steel.

MnS, with  $\lambda \gg 1$ , do not act as crack inducers in the parent steel phase, excluding grain boundary embrittlement. However, tension cracks may arise from axial compression in an iron matrix with highly deformable inclusions. The fractured inclusions, however, serve an important role in initiating failure of the steel when subsequent stressing reoriented from the initial compressive pattern.

The properties which are most greatly influenced by nonmetallic inclusions are those which involve ductile failure, i.e., opening up, growth and coalescence of voids within the metal with increasing strain. During straining at room temperature, the nucleation of cavities is often observed to occur either by particle cracking or by decohesion of particle-matrix interface. In case of carbide such as lamellar cementite in ferrite matrix, the cavitation process is commonly one of carbide cracking. In case of sulfides and oxides

cavitation commonly occurs by decohesion of the interface between the inclusion and matrix, although inclusion itself may suffer subsequent damage by virtue of secondary (compressive) strains. Interface decohesion associated with nonmetallic inclusions occurs at very small strains, suggesting that interface has a low mechanical strength.

Judging from the microfractographic evidence, MnS inclusions are understood to subdivide at first cross-section on which final separation takes place by the formation of inclusion sized cracks, as shown in Fig. 24. Subdivision of cross section results in a dominance of shear mode deformation which leads to decreased ductility. Applying this concept to a microscopic dimension, the decrease in ductility with MnS inclusions can be readily explained by this mechanism of subdivision.

Significant effects of inclusions are noted in connection with tensile ductility, ductility in triaxial ductile fracture, and situations where energy required for rupture is assessed, e.g., in the ductile self energy of notched impact tests. Inclusions have little effect on y.s., t.s. or tensile elongation; these properties are dependent upon the initiation of plastic deformation or upon plastic instability criteria associated with work hardening characteristics. Only severely reduced fracture ductility would cause fracture to precede the onset of plastic

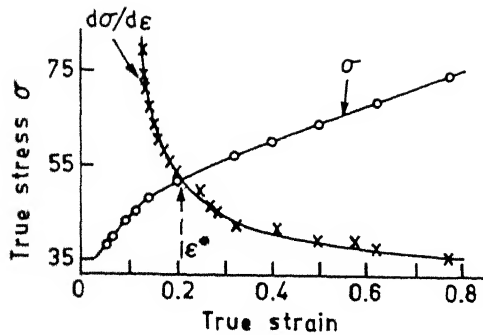
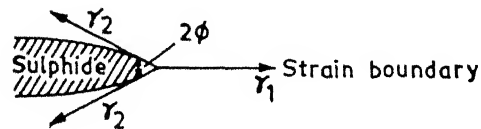


Fig. 25. The definition of plastic instability at strain above  $\epsilon^*$  (Ref. 53)



$\gamma_1$  = Interfacial tension or surface energy between iron grains

$\gamma_2$  = Interfacial tension or surface energy between iron grain and sulphide

$2\phi$  = Dihedral angle

Fig. 26. Relationship between surface energy and dihedral angle (Ref. 53)

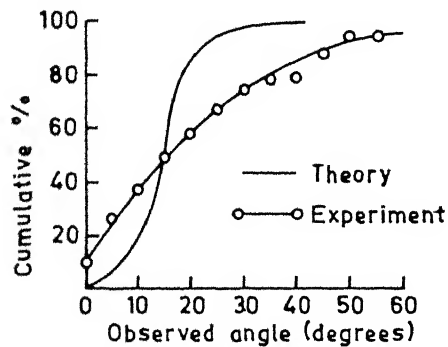


Fig. 27. Experimental and theoretical cumulative frequencies for a dihedral angle of  $15^\circ$  (Ref. 53)

instability in the uniaxial tension test. In biaxial tension, however, the instability strains are much higher and some effect of inclusions on the extension have been observed.

Dulieu and Gouch [51] have shown that the basic features of inclusions distributions which control ductility also affect  $K_{1c}$  values in ultra high strength steels when fracture occurs by the ductile rupture mechanism. Increasing the volume fraction of inclusions decreases the  $K_{1c}$  value, and  $K_{1c}$  value exhibits a degree of anisotropy that is directly commensurate with the effects of inclusion anisotropy on the ductile fracture process, i.e. transverse properties are inferior to longitudinal properties when elongated inclusions are present.

So we see that non-metallic inclusions have a marked effect on many properties which are virtually important to the steel user. Much still requires to be done however, not only to understand mechanisms by which inclusions affect various properties, but also to establish quantitative relationships which will enable the properties to be predicted. Considerable progress has been made with the continued and rapid development of quantitative image analysing microscopy, but the ultimate research tool would probably be the development of technique using the methods currently being developed but with the signals being

provided by the X-Rays generated from compositional differences in inclusions, i.e., by a microprobe analysis technique.

#### 1.10 SEGREGATION TO GRAIN BOUNDARY, INTERFACES AND FRACTURE

According to Murr [54] surface was considered to be the interface separating a solid phase particles from its saturated liquid or vapor phase. Interface can be described as any dividing surface that interrupts a periodic lattice arrangement, or separates homogeneous phase of various crystal structure, or heterogeneous phase of varying composition and crystal structure, or both, or any combination of those properties. These interfaces can be continuous or discontinuous on an atomic scale.

Research on surfaces and interfaces seems to have first developed in metallurgy. Thus pure crystal growth techniques, such as melting zone, were initiated for metals, then transferred to semiconductors. Many studies of metallurgical interest should, however, be pursued or examined with more refined techniques, especially in the field of plastic deformation of polycrystals, inter-and intra-grannular fractures, nucleation and propagation of fatigue cracks, role of surfaces and interfaces in fatigue, and more generally the role of surface treatments on plasticity [55].

The relationship between interfacial tensions and the dihedral angle has been developed, and is shown in Fig. 26. This work[53] was carried out on those sulfides which occur at grain boundaries.

It suffices to say that

$$\cos\phi = \frac{\gamma_1}{2\gamma_2} \quad (38)$$

and the limiting condition for this relationship is,

$$\gamma_1 \leq 2\gamma_2 \quad (39)$$

When  $\gamma_1 = 2\gamma_2$ ,  $\phi$  becomes zero and complete grain boundary penetration is possible. To determine the value of  $2\phi$  - the dihedral angle, a considerable number of individual angles must be measured, and a median value obtained by plotting a cumulative frequency curve.

In doing this, it becomes very clear that a unique angle does not exist, Fig. 27, because of the shape of the curve. This is perhaps to be expected because the interfacial tensions will be orientation dependent, and thus will vary between various pairs of grains. It is therefore only possible to quote an average median angle value. The variation found in the dihedral angle for both MnS and FeS at various Mn:S ratios is shown in Fig. 28. Both MnS and FeS show a minimum dihedral angle in the Mn:S ratio range 1.5 to 2.0, and much lower dihedral angle values of FeS together with its low melting temperature indicate why FeS will make a steel

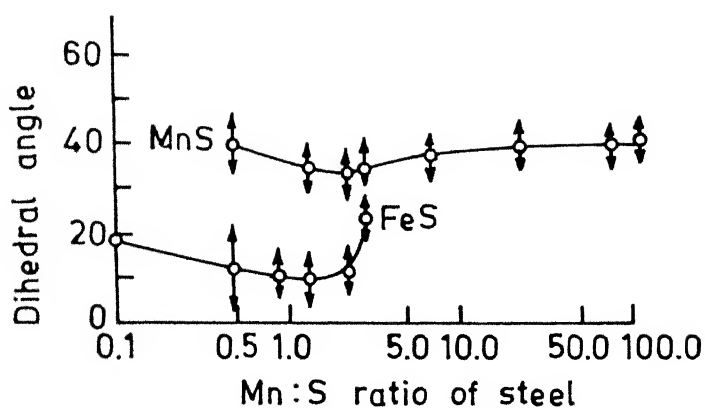


Fig. 28. Effect of Mn:S ratio on dihedral angle of sulphides (Ref. 53)

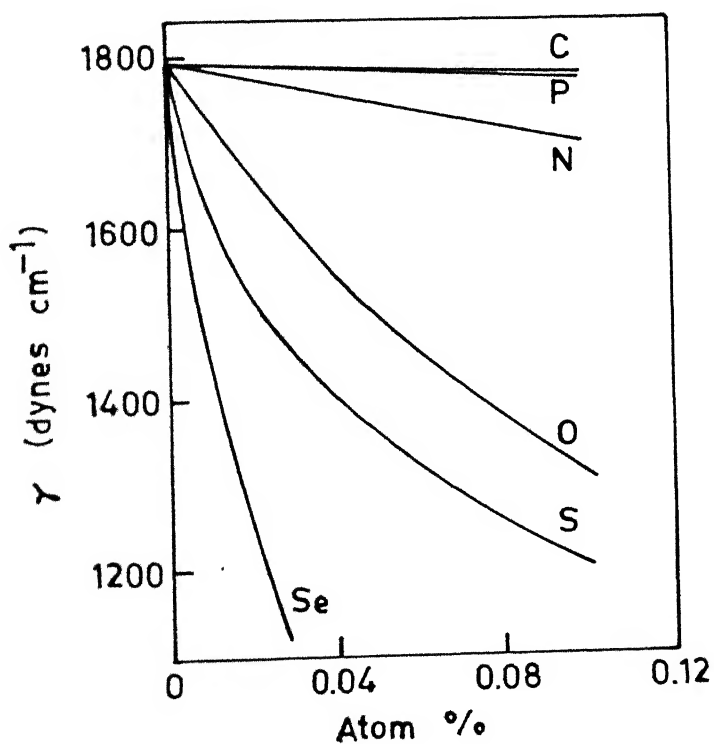


Fig. 29. Surface tensions for solutions (Ref. 53)

susceptible to becoming hot short, the FeS being much more able to penetrate between the austenitic grains.

According to Hondros [56] and Ramasubramanian [57] many substances are embrittled by grain boundary segregation of a solute, yet the equilibrium solubility of the solute in the bulk phase is very small. The relative interfacial energies of the segregated and unsegregated grain boundaries and surface energies, segregated and unsegregated, of the free surface are important in discussing the fracture of such materials. These quantities have not been fully measured and thus theoretical treatments have not been quantitatively useful.

According to Fine [58], the conditions for equilibrium surfaces and bulk phases are that the chemical potentials are everywhere equal. If the concentrations of the solute in the surface phase, are known, e.g., from Auger measurements, the surface and grain boundary energies of the pure solvent can be determined, and the free energy versus solute fraction in the bulk phase can be established, then the surface energies of the segregated grain boundary and segregated surface at equilibrium may be determined.

A small amount of sulfur often causes grain boundary embrittlement of iron and steel at low temperatures as well as at elevated temperatures. The grain boundary embrittlement considered to be caused by segregation of sulfur at grain boundaries. Solutes like carbon, nitrogen or others may



interact with sulfur and modify its segregation. But it is difficult to specify the state of sulfur ( i.e. in solid solution, in a precipitate, or in other states, with other solutes), on which the degree of segregation and properties of the specimens depend strongly. Studies on iron-sulfur alloys [50] showed that increasing the concentration of C prevented intragranular fracture and decreased the DBTT of all iron-sulfur alloys. The DBTT increased with the concentration of sulfur at a fixed concentration of carbon. More carbon had segregated to grain boundaries where more sulfur had segregated. The segregation energy, estimated for carbon to be about 80 KJ/mol, and for sulfur to be 75 KJ/mol. The segregation energy for sulfur is larger than that for phosphorous in iron, 50 KJ/mol. Hence sulfur segregates more readily than phosphorus for the same bulk concentration. Sulfur causes more severe embrittlement than phosphorous if compared at the same bulk concentration. According to Suzuki [59], toughening due to carbon segregation is partly due to site competition between sulfur and carbon at grain boundaries. But it is not the sole cause of the toughness improvement. Carbon segregated at grain boundaries increases the grain boundary cohesion. It has been estimated that 1 atom percent of sulfur at grain boundaries increases the DBTT by 40°K. Segregated carbon attractively interacts with the segregated sulfur to recover the boundary cohesion weakened by sulfur.

High temperature intergranular fracture has been identified as a mode of failure in alloy steels. It is associated with the dynamic segregation of sulfur to cracks in hard microstructures stressed at elevated temperature. According to Hippsley [60], sulfur is produced by the dissolution of grain boundary manganese sulfide on opened crack faces, and accumulates at the crack tip by surface diffusion. The sulfur can then promote fracture either by encouraging decohesion or by reducing the cavity tip 'flank angle.

Alloy steel, in the 'as received' condition contains sulfur largely combined with other elements in the form of relatively large sulfide inclusions. Such inclusions are distributed throughout the grain structure and will intersect some grain boundaries. High temperature austenization causes partial dissolution of large sulfides, enabling approximately 30 ppm sulfur to be taken into solution at 1300°C in some steels. A fast quench will cause some of the dissolved sulfur to remain in solution in the ferrite structure, while the rest precipitates out as a fine distribution of sulfides associated with prior-austenitic grain boundaries. Sulfides are either exposed by brittle intergranular fracture, but makes no significant contribution to sulfur enrichment, or they are not present on the fractured grain boundary surface in any significantly greater abundance than on transgranular surfaces. Fractographic evidence taken from several studies of

high and low temperature fracture in embrittled, overheated steels suggests that, in fact, the small sulfides are not exposed by brittle intergranular fracture. Crack tip stress was confirmed as an important factor enhancing sulfur enrichment. It was most effective at zones of local crack tip enrichment, and was found to encourage the release of sulfur from large sulfides where present.

It seems likely that sulfur plays an important role in slow, brittle crack propagation, it must both embrittle grain boundaries in steel and be suitably located at the crack tip to do so within the overall fracture mechanism envisaged.

It is apparent from many studies that dislocations can arise mainly from grain boundaries. The majority of the initial dislocations that appear during the onset of plastic flow arise at grain boundaries or other interface. Following the initial generation of dislocation at the grain or interphase boundaries to form forests or tangled arrays, subsequent dislocation multiplication can occur within each grain by a double cross-slip mechanism.

Many solutes in liquid metals are surface active, especially, O, S, Se, Te [61]. The effect of these on the surface tension of Fe is shown in Fig. 29. Solute metals are less active than nonmetals.

## CHAPTER II

### EXPERIMENTAL PROCEDURE

The HSLA steel used in the present investigations had the following composition ( in weight %) in the as received condition ( hot rolled, air cooled):

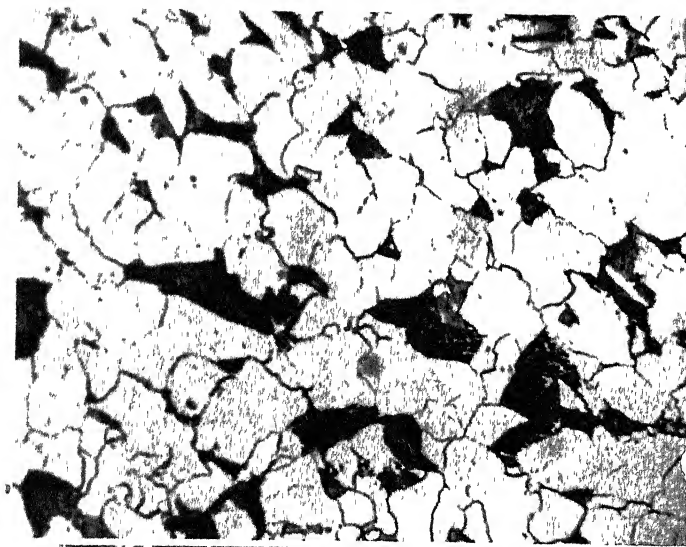
C	Si	S	P	Mn	Nb	V	Ni	Cr	Cu
.185	.16	.019	.014	.96	.062	.006	.013	.015	.011

The regular mechanical properties of the steel were determined using standard tensile test specimens recommended by ASTM and tabulated below. A micrograph of the steel under study in as received condition is shown in Fig. .

#### Mechanical Properties

.2% yield strength	430 MPa
Ultimate strength	525 MPa
Elongation	27%
Room Temperature Charpy Energy	26 ft-lb (35.26 J)

Bend tests, direct tensile tests and Charpy impact tests were carried out over a range of temperatures in order to correlate fracture toughness with other mechanical properties.



Microstructure of the HSLA steel in as received condition

## 2.1 BEND TEST

### 2.1.1 Specimen Design and Preparation

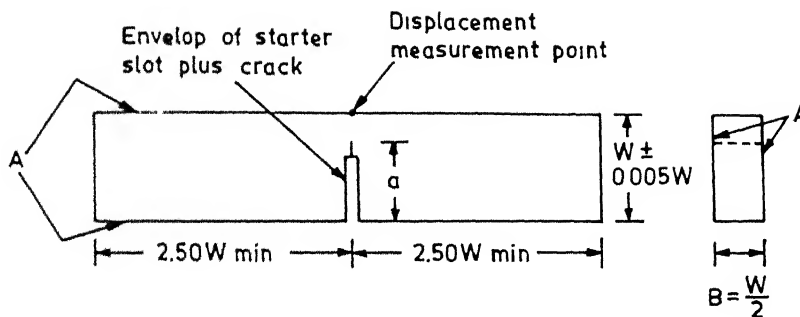
Specimens (100 mm X 20 mm X 10 mm) for the three point bend test were machined from the as received angle ( received as 130 mm X 10 mm- 90° angles).

a) Plane Strain Condition : One important requirement of this test method is to limit plastic deformation by maintaining plane strain conditions at the crack tip. High triaxial stress are developed at the crack tip, if the test piece is thick which prevents spreading of yield laterally to the centre of the crack - front. The size requirement for test specimens to ensure plane strain is given by the relation

$$B, a \geq \frac{\alpha J_{1c}}{\sigma_{flow}} \quad (40)$$

Where B,a are the specimen thickness , and crack length respectively.  $\sigma_{flow}$  is the flow stress which is taken as the average of yield stress and ultimate stress.  $\alpha$  is a non-dimensional constant taken to be in the order of 25. This value might differ slightly from one material to another depending on the degree to which the material strain hardens.

Different specimens of varying thickness and crack length were produced and tested and the values of  $J_{1c}$  and



$$\begin{aligned} W &= 20 \text{ mm} \\ B &= 10 \text{ mm} \\ a &= 15 \text{ mm}, \quad \frac{a}{W} = 0.75 \end{aligned}$$

Fig. 30. Bend specimen standard proportions and tolerances. Surface A is perpendicular and parallel to within  $0.001W$ , crack is perpendicular to specimen length and thickness to within  $2^\circ$ .

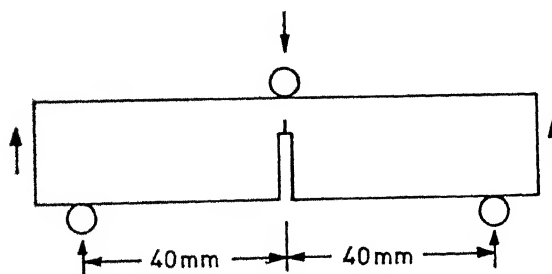


Fig. 31. Loading conditions of the specimen during bend test.

$\sigma_{flow}$  analysed. The dimension of the test samples were thus consistent with the bar creiterion. The standard bend type specimens were prepared according to the recommended ASTM  $J_{1c}$  test standard E 813-81. The sample had the profile and dimensions as shown in Fig. 30.

The loading conditions of the specimen during the test is shown in the Fig.31 .

b) Specimen Preparation: Many specimens obtained from SAIL, Ranchi, manufactured by IISCO, of the dimensions 100 X 20 X 10 mm. were machined from the angle. The crack length to width ratio of specimen, i.e.,  $a/W$  was kept 0.75 in all the specimens. First, a slot of 1 mm width and 13 mm length was made in each specimen on the full thickness and the width direction of the specimen. This was done uniformly by milling in all the specimens. The final 2 mm of the required 15 mm notch depth was cut by a spark erosion wire. The spark erosion machine used paraffin as the dielectric medium and operated at minimum gap voltage to prevent overheating of the crack root. The speed of the cutting was also kept low to create smooth cutting.

Similar notches were cut in all the specimens used in the bend tests. The  $a/W$  ratio was kept consistent at 0.75 in all the specimens.

All the specimens were polished on all the sides by automatic magnetic grinder and were free of any surface



defect, before testing on the bending fixtures.

### 2.1.2 Test Procedure

Bend tests were carried out in a MTS floor model machine ( 810.12) of the hydraulic arm movement type. The standard bending fixtures were fixed on the MTS. Initially a test was conducted at room temperature. A specimen was mounted on the fixtures and the bottom rolls were adjusted to give the required span length of exactly 80 mm. The point of application of load, P, on the specimen was properly fixed with the help of telescopic viewer. The cross head motion was fixed at the rate of 1.5 mm/ sec. Proper scale were chosen for the load and displacement measurements on the X-Y recorder. A plot between load and the displacement of the load point was obtained. The test was stopped once the load dropped due to the initiation of the crack and the point of maximum load was pin-pointed. The area under the curve, A, i.e. measured till the maximum load, gives the work done on the specimen to initiate the crack. This area as described earlier related to the J-value by the equation

$$J_1 = \frac{2A}{Bb}$$

where B is the specimen thickness and

b is the uncracked ligament

### Correction of Load-Displacement Records

Several sources of coincidental displacement are included when load displacement in three-point bending is

measured from the loading pin relative to the test base. The major errors are due to elastic deformation of the various test fixture components and the elastic and plastic indentations of the specimen by the loading pin and supporting rollers. A method for correcting the test record for such coincidental displacement has been discussed by Buzzard and Fisher [20]. The experimental set up for determining coincidental load point displacement is illustrated in Figures 32 and 33.

A block of the same material and material conditions as the support block was inserted into the span gap of the support block. The support rollers were butted together to provide a span as close to zero possible. An undeformed part of the specimen was then placed in position on the butted rollers with the same orientation as in the test proper. A load versus load point deflection record was obtained as described in the previous section with the highest load slightly in excess of the maximum load achieved during the bend test. This is described in Fig. 32.

In determining  $J_1$ , the test record was primarily used to obtain the area under the load-displacement curve. A simple and direct method used for determining the corrected area under the load-displacement curve is depicted in Figures 32 and 33. The area under the coincidental displacement curve was simply subtracted from the area

under the primary test curve to yield the corrected area for the test. No replotting is necessary in using this procedure, thus conserving much time and effort in analyzing test data.

The area was measured by using Planimeter, which is one of the most accurate methods of measuring area under the curve.

### 2.1.3 Bend Tests at Various Temperatures

The bend tests were carried out over a range of temperature starting from  $440^{\circ}\text{C}$  upto  $727^{\circ}\text{C}$  which is slightly above the eutectoid temperature in a plain carbon steel. Tests were conducted at  $30^{\circ}\text{C}$ ,  $440^{\circ}\text{C}$ ,  $490^{\circ}\text{C}$ ,  $603^{\circ}\text{C}$ ,  $693^{\circ}\text{C}$ ,  $717^{\circ}\text{C}$ ,  $718^{\circ}\text{C}$ ,  $727^{\circ}\text{C}$ .

Suitable thermocouple i.e., chromel-alumel thermocouple were soldered to each specimen. Samples were soaked in a furnace at about  $1000^{\circ}\text{C}$  for 30 minutes. The specimens were then taken out and fixed on the bending fixtures as quickly as possible and the temperature monitored continuously. The test was started when once the required temperature was going to be reached. In each test, the temperature was noted at the point when the load dropped after reaching the maximum load and test was stopped and specimen taken out. The total duration of test was limited to 1-2 minutes. Strain rate remained constant for all the temperatures.

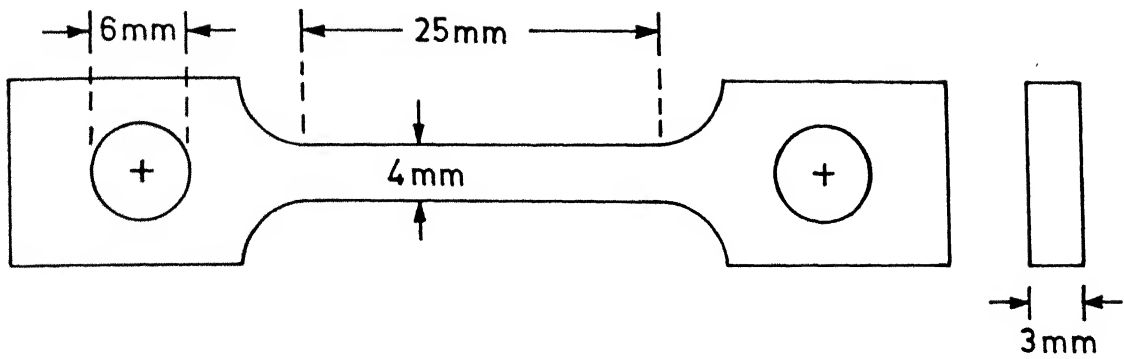


Fig. 34a. Profile and dimensions of direct tensile test specimen.

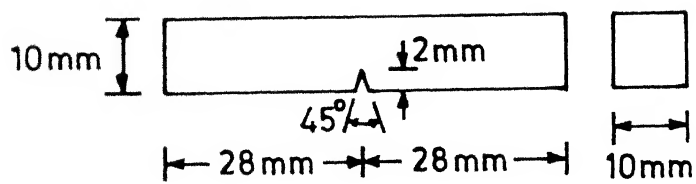


Fig. 34b. Charpy impact test specimen.

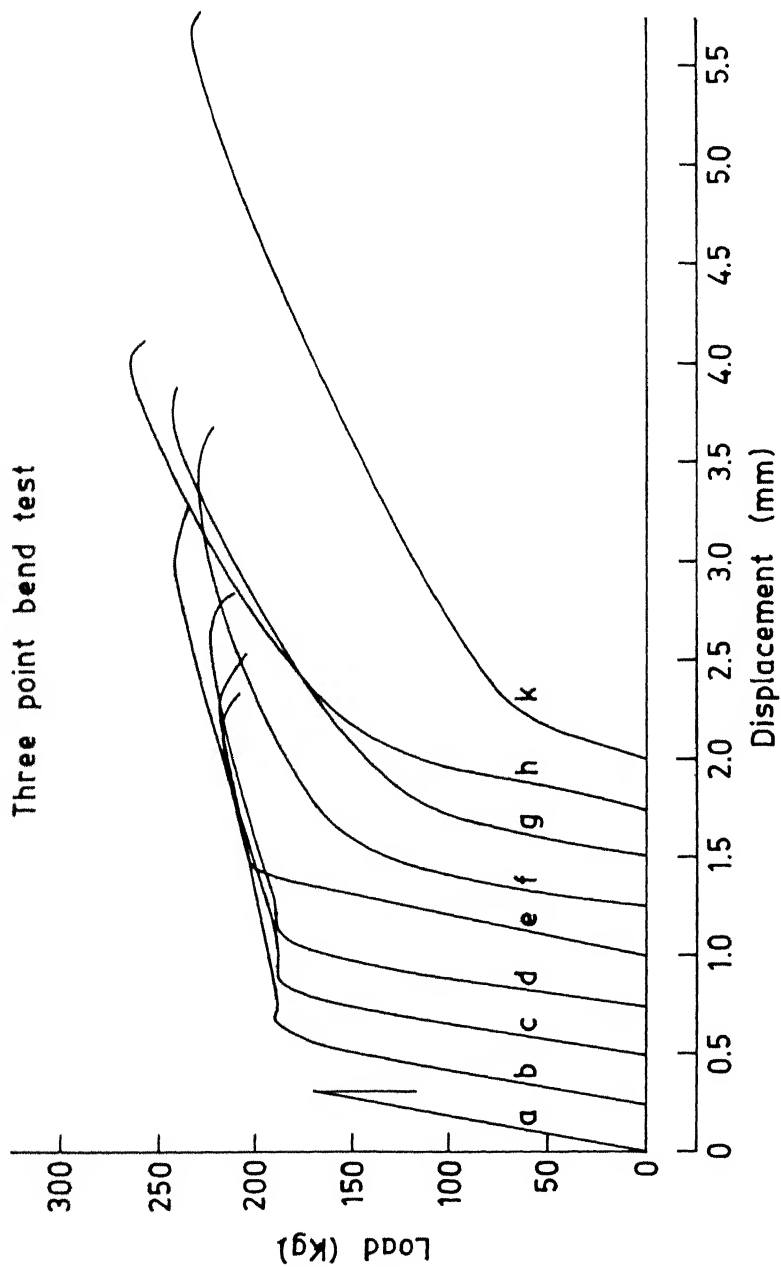


Fig. 35a. Load displacement records for three point bend tests at various temperatures. (a)  $-170^{\circ}\text{C}$  (b)  $-59^{\circ}\text{C}$  (d)  $-21^{\circ}\text{C}$  (d)  $-10^{\circ}\text{C}$  (e)  $28^{\circ}\text{C}$  (f)  $101^{\circ}\text{C}$  (g)  $190^{\circ}\text{C}$  (h)  $260^{\circ}\text{C}$  (k)  $340^{\circ}\text{C}$

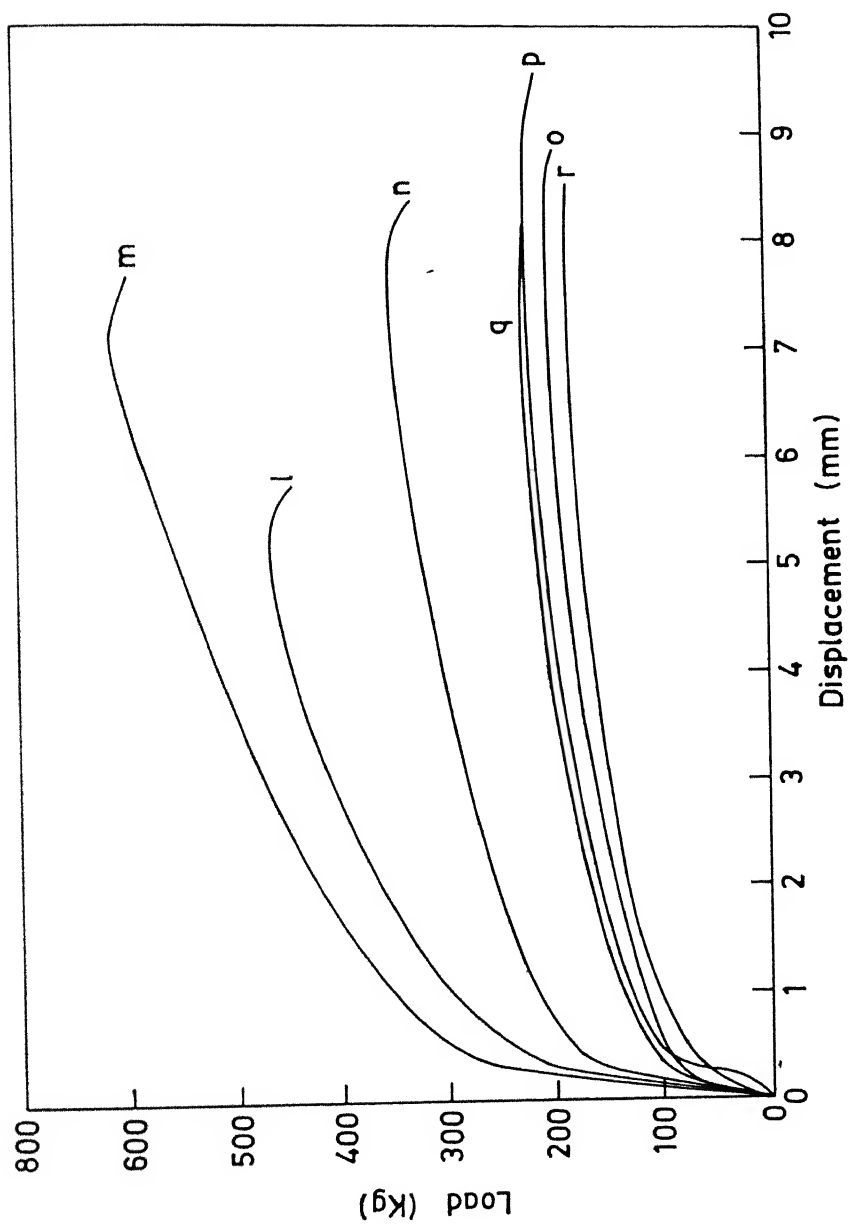


Fig. 35b. Load displacement records for three point bend tests at various temp.  
 (l) 440°C (m) 490°C (n) 603°C (o) 693°C (p) 717°C (q) 718°C (r) 727°C.

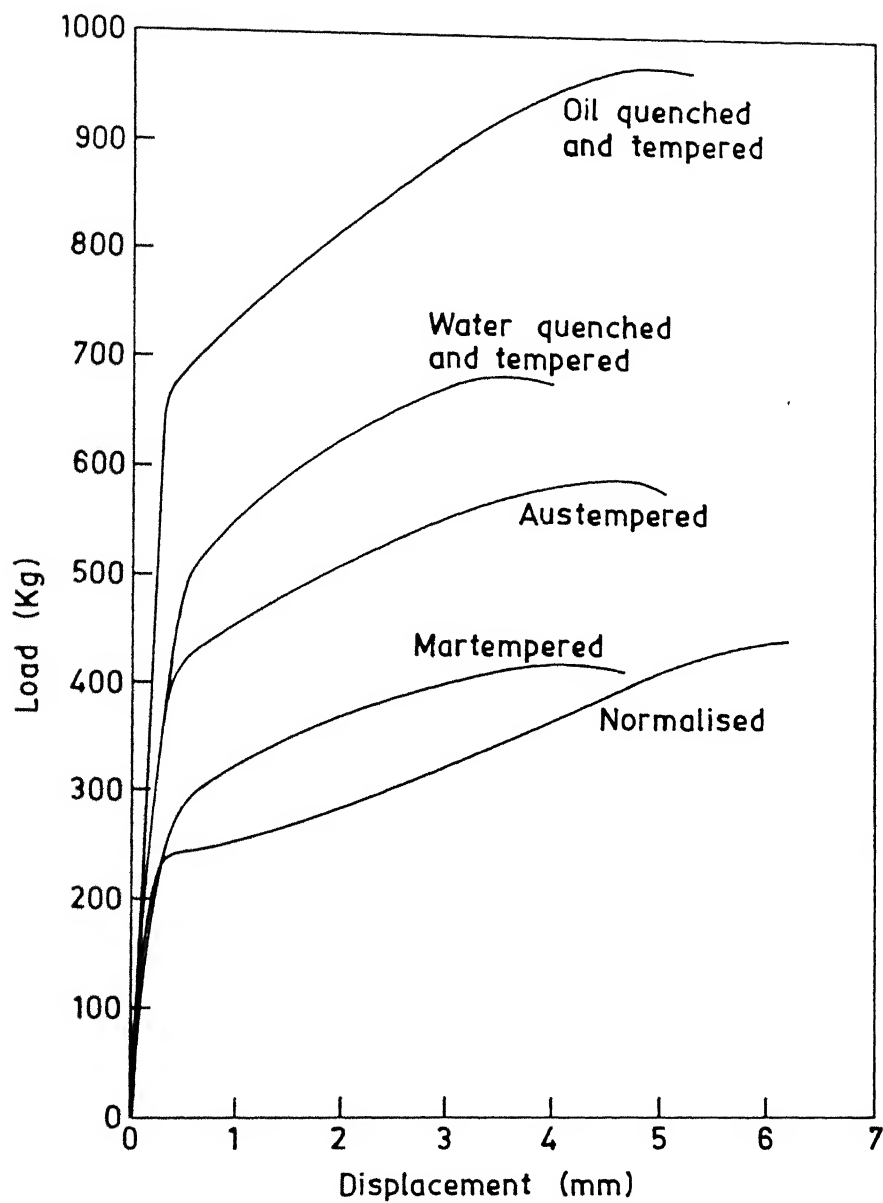


Fig. 36. Load-displacement records for three point bend tests for various heat treatments.

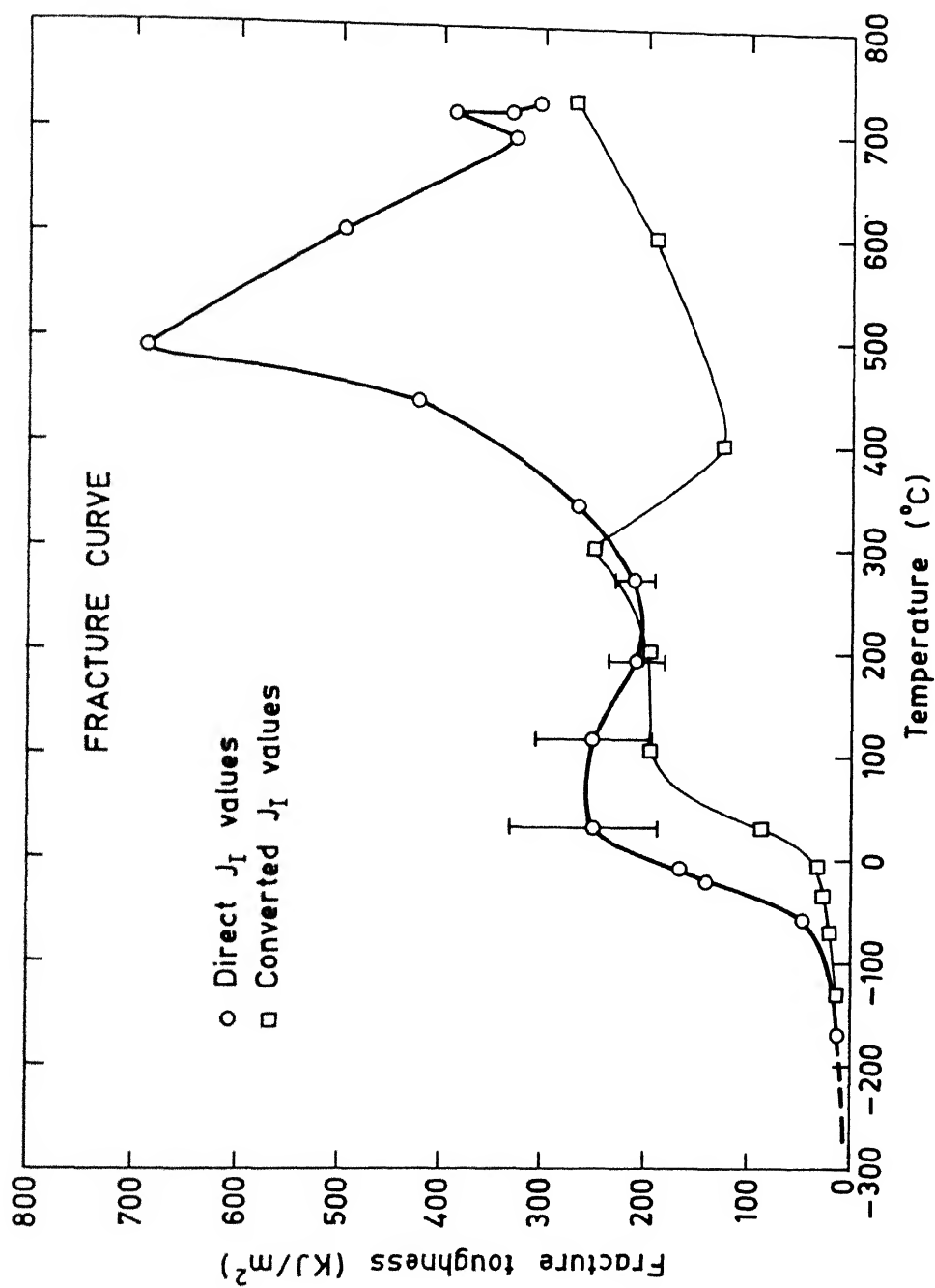


Fig. 37a. Variation of fracture toughness ( $J_I$ ) with temperature.



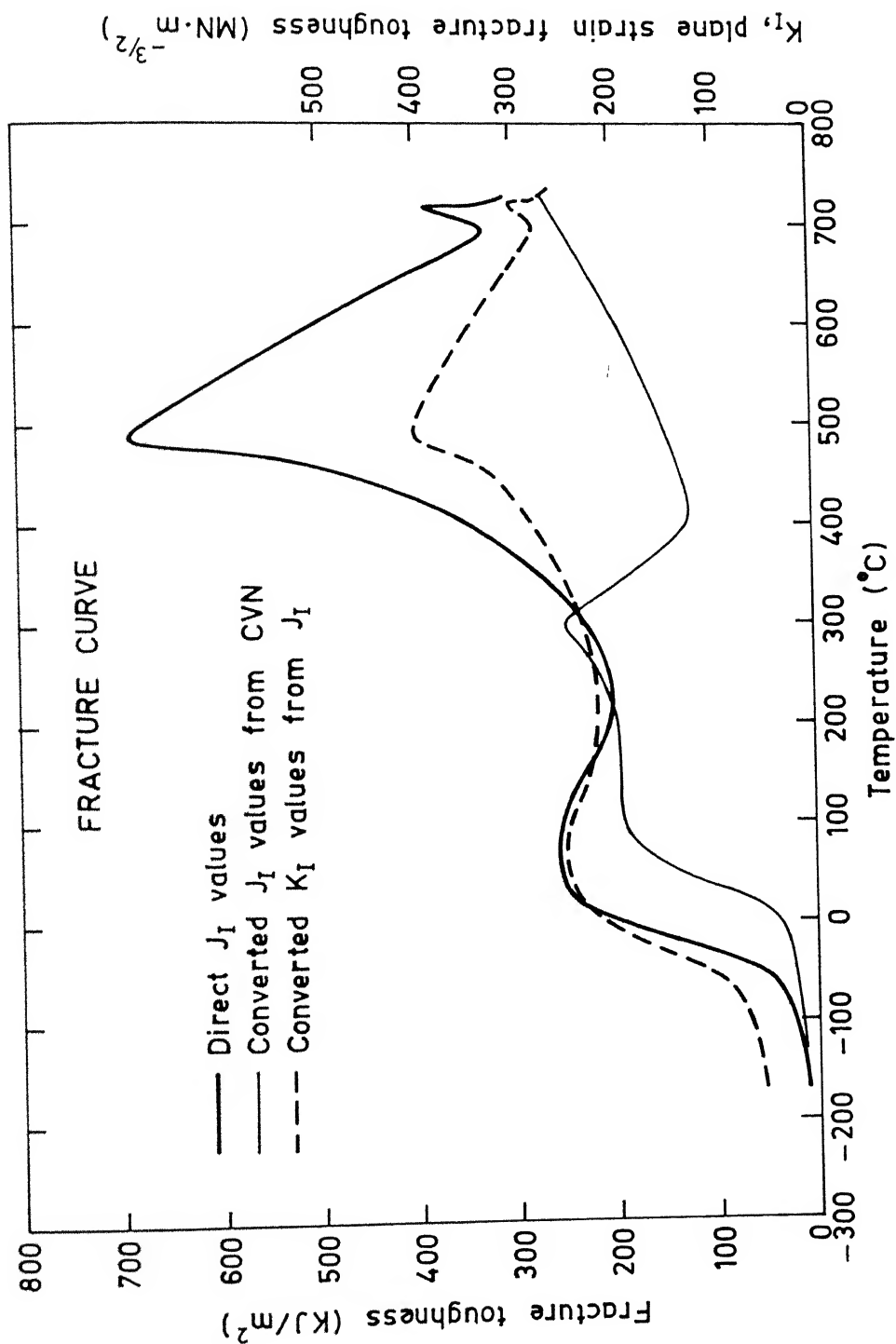


Fig. 37b. Variation of fracture toughness with temperature .

The cross-head speed and corresponding strain rate was kept constant for all the tests carried out at different temperatures. The load displacement records were plotted on a separate X-Y recorder and corresponding areas under the load-displacement plot were determined. From these areas the coincidental displacement area (discussed above) was subtracted to obtain the respective corrected areas. The J-values were calculated using the relation

$$J_1 = \frac{2A}{Bb}$$

where A is the area under load-displacement,

B is the thickness

b is the unbroken ligament.

Low temperature test results from -170°C upto 340°C were available from an earlier investigation.

These  $J_1$ - values were plotted against the temperature. Fig.37(a).

$J_{1c}$  at room temperature was determined for three different crack lengths, which can be used as a design criteria without going through the conventional, cumbersome  $J_{1c}$  determination.

## 2.2 STRAIGHT TENSILE TEST

Tensile specimens of the same steel were machined according to the dimensions shown in Fig.34(a). Straight tensile tests were carried out at temperatures 400°C,

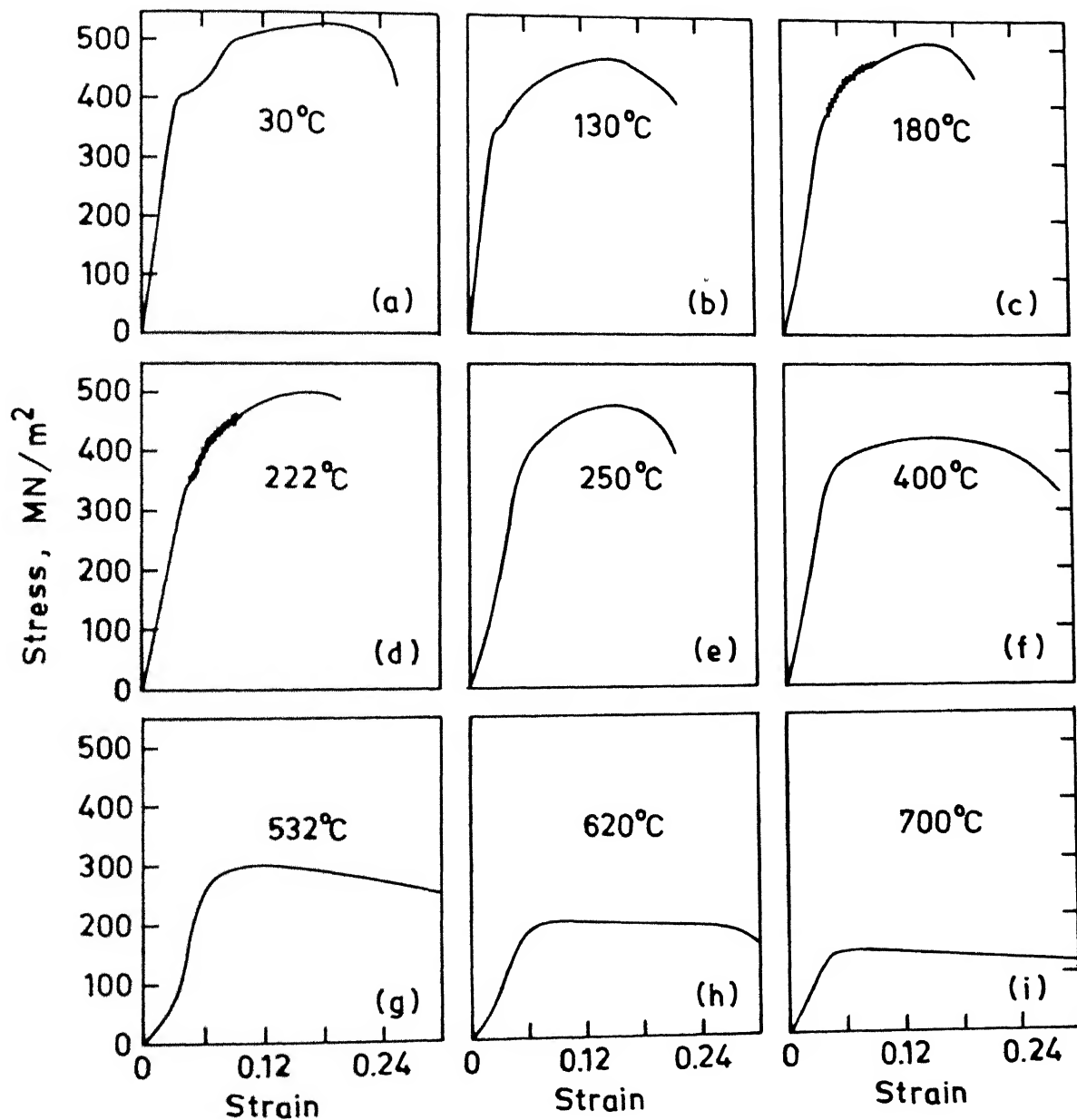


Fig. 39. Stress strain curves of direct tensile tests at various temperatures.

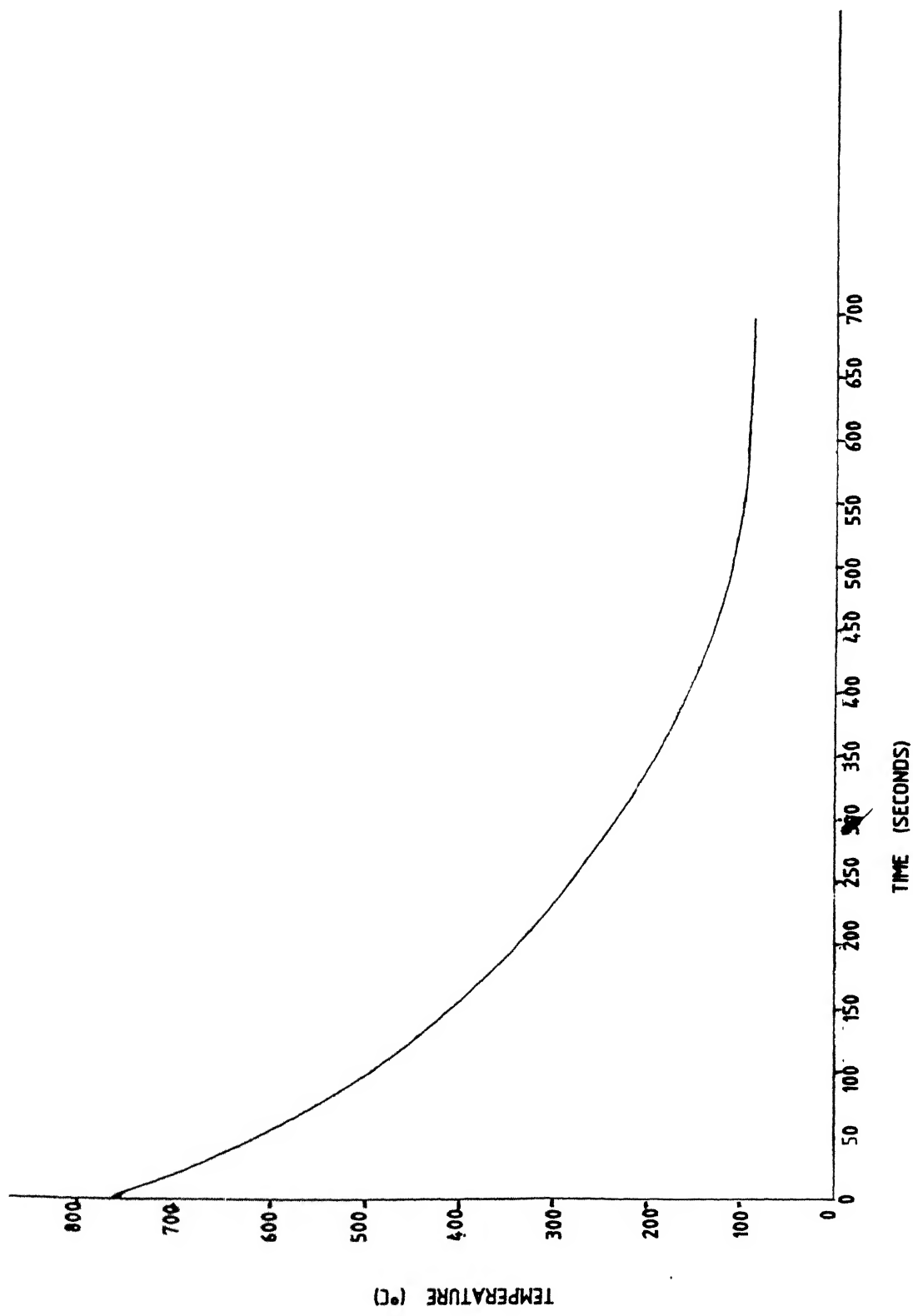


Fig. 38a. Cooling curve of the sample for charpy impact testing.

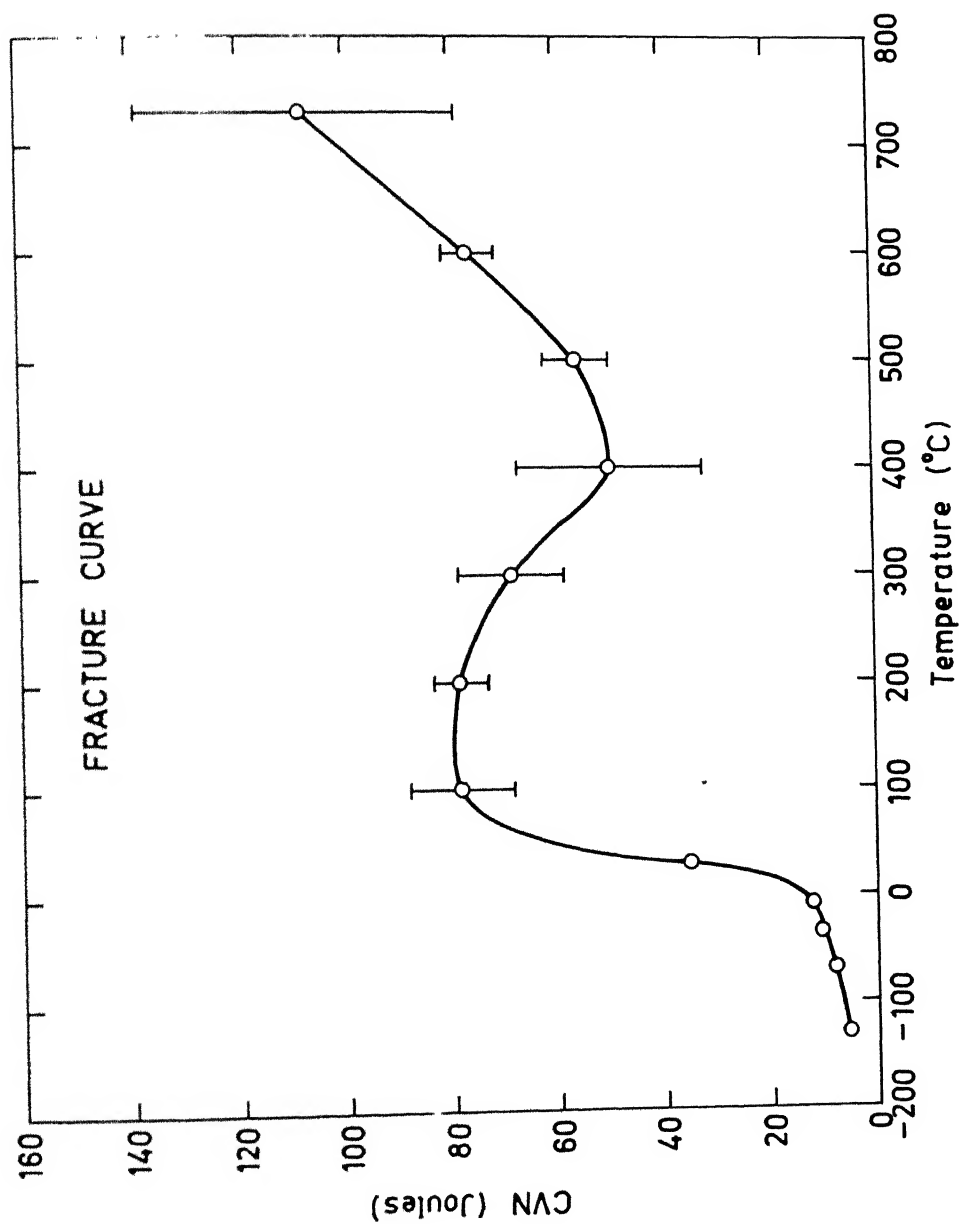


Fig. 38b. Variation of Charpy V-notch number with temperature.

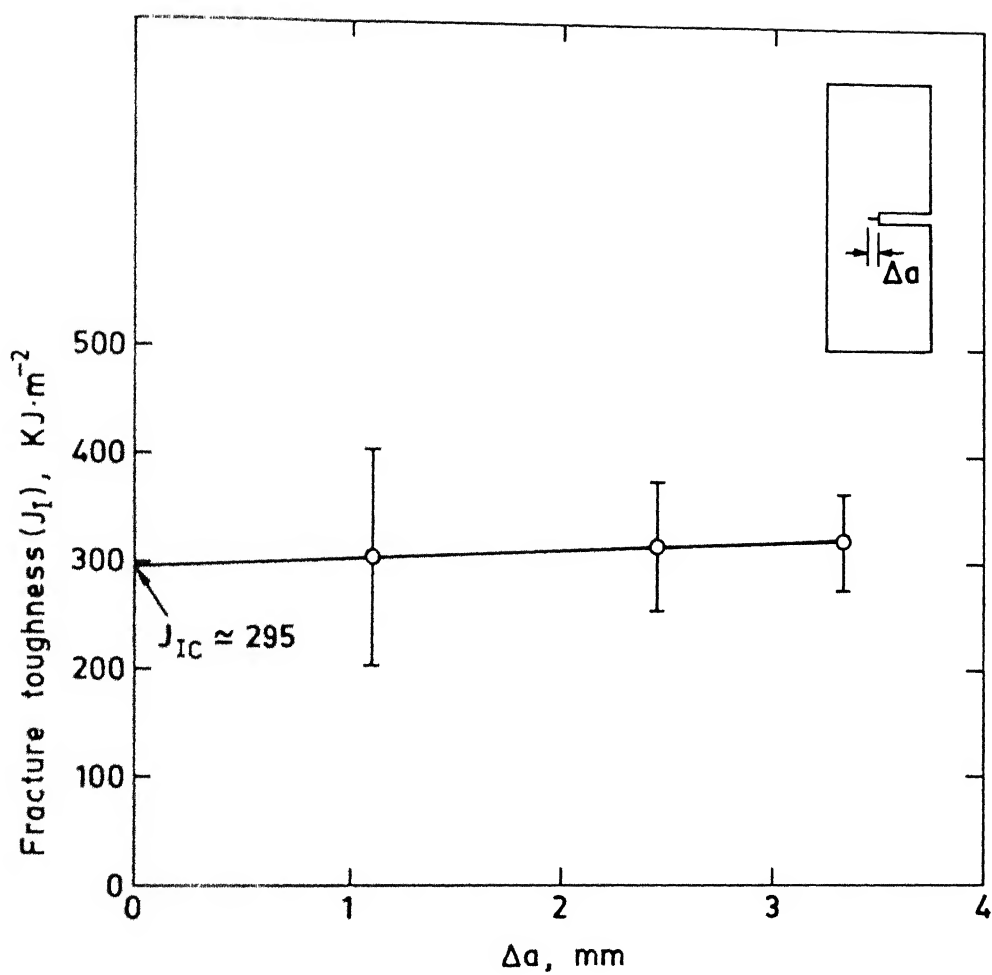


Fig. 40. Determination of  $J_{IC}$  for various crack lengths.

532°C, 620°C, 700°C. The tests were conducted in the floor model Instron 1195. The specimens were mounted on a specially designed grips. The furnace temperature was brought to the required one and specimen along with the grips were introduced inside and properly mounted at both ends. Once the specimen attained the required temperature which was again monitored by a thermocouple attached to its centre, the test was conducted. Generally, it took around 20 minutes to soak the required temperature before the test started. A cross head speed of 1 mm/ min corresponding to a strain rate  $6.67 \times 10^{-4} \text{ sec}^{-1}$  was used at all temperature tests. The load-displacement plots were obtained for all the specimens at different temperatures and converted into engineering stress versus engineering strain plots after applying machine corrections. All these plots have been presented in Fig. 39.

Low temperature results from 30°C upto 250°C were taken from an earlier investigation. Engineering strain at fracture versus temperature, UTS versus temperature and YS versus temperature were plotted, will be discussed in the next chapter.

### 2.3. NOTCHED BAR IMPACT TEST

#### 2.3.1 Speciment Design and Preparation:

Samples were cut from the block. Specimen has a square cross-section ( 10 mm X 10 mm) and contains a

45°V notch, 2 mm deep with a 0.25 mm root radius according to standard specification for a charpy test, as shown in Fig. 34 (b).

### 2.3.2 Test Procedure

Tests were carried out on a charpy impact machine over a range of temperature. A complete cooling curve of the sample resting on the machine anvil was obtained from a temperature starting from 800°C which gives the time taken to reach any desired test temperature before the conduct of a series of impact tests since the temperature was measured by inserting a chromel-alumel thermocouple into a cylindrical hole terminating at the notch plane, the test temperature would correspond in as far as possible to the temperature at the plane of fracture.

In actual test, striker of the charpy impact machine was released as soon as the sample reached the test temperature while on the anvil of the machine and fracture energy noted. Tests were carried out from 400°C to 730°C, which is slightly above the eutectoid temperature. Low temperature tests from -130°C upto 300°C were available from a previous study.

### 2.4 Electron Micro Probe Analyser and Scanning Electron Microscopy

Scanning Electron Fractographs and X-Ray microanalysis were carried out in a JEOL Electron Micro Probe



Analyser ( model JC X A -733) operating at an accelerating voltage of 20 KV with probe current  $1 \times 10^{-8}$  A and pressure inside the chamber was  $10^{-6}$  torr. It can operate at a maximum voltage of 50 KV.

Fractured samples were chosen from room temperature upto  $727^{\circ}\text{C}$  and some of the heat treated samples. X-Ray micro analysis was done for room temperature sample to know the distribution of microconstituents on the fracture surface, microconstituents being sulfur and phosphorus . Both the secondary and back scattered electron mode were studied for SEM fractographs, which will be discussed in detail in the next chapter.

## 2.5 TRANSMISSION ELECTRON MICROSCOPY

TEM study of a zone immediately behind the fracture surface produced in the CVN and bend tests was carried out to determine the presence of precipitates, if present, in the microstructure and also to know the mechanism of fracture. Dark and bright field images as well as selected area diffraction pattern (SADP) were taken besides normal TEM pictures.

The instrument was operating at an accelerating voltage of 300 KV.

TEM samples were chosen from CVN tests at room temperature and  $730^{\circ}\text{C}$  and bend tests from room temperature

The salient features of the micrographs will be discussed in the next chapter.

## 2.6 OPTICAL MICROSCOPY

Some of the heat treated bend samples are presented in Fig.47, besides room temperature tested bend sample and will be discussed in the next chapter.

## CHAPTER III

### RESULTS AND DISCUSSIONS

#### 3.1 BEND TEST RESULTS

The  $J_1$  values calculated from the load-displacement plots of the bend tests, carried out at different temperatures are tabulated as follows:

Temperature ( $^{\circ}\text{C}$ )	$J_1$ ( $\text{KJ} \cdot \text{m}^2$ )
-170	12.82
- 59	45.01
- 21	140.07
- 10	168.92
+ 28	255.00
+115	250.00
+190	209.71
+276	210.00
+340	268.59
+440	424.81
+490	689.023
+603	499.75
+693	328.78
+717	388.98
+718	332.49
+727	306.59

## CHAPTER III

### RESULTS AND DISCUSSIONS

#### 3.1 BEND TEST RESULTS

The  $J_1$  values calculated from the load-displacement plots of the bend tests, carried out at different temperatures are tabulated as follows:

Temperature ( $^{\circ}\text{C}$ )	$J_1$ ( $\text{KJ} \cdot \text{m}^{-2}$ )
-270	12.82
- 59	45.01
- 21	140.07
- 10	168.92
+ 28	255.00
+115	250.00
+190	209.71
+276	210.00
+340	268.59
+440	424.81
+490	689.023
+603	499.75
+693	328.78
+717	388.98
+718	332.49
+727	306.59

These results have been graphically plotted taking  $J_1$  values on ordinate and temperature on abscissa. This is shown in Fig. 37. From this graph it is obvious that  $J_1$  values increase with temperature from subzero temperatures to high temperature level. This indicates that the fracture toughness of the steel under investigation increases with temperature. There is a sharp decrease in  $J_1$  values in going from  $-20^{\circ}\text{C}$  to  $-80^{\circ}\text{C}$  as shown in Fig. 37. Therefore there exists a ductile to brittle transition in using  $J_1$  as a material property. After this, from  $25^{\circ}\text{C}$  to  $230^{\circ}\text{C}$  exists a plateau region in the curve which signifies a minimal change in the  $J_1$  Values. Above  $230^{\circ}\text{C}$ , there exists again a steep increase in the  $J_1$  values upto  $490^{\circ}\text{C}$ . The plateau in the  $J_1$  versus temperature plot corresponds to the dynamic strain ageing appearing in the direct tensile tests over these temperature range are given in a succeeding section and analysed. After  $490^{\circ}\text{C}$ , there is sharp decrease in  $J_1$  values upto  $730^{\circ}\text{C}$ . The reason for the decrease discussed earlier, due to hot shortness or presence of deleterious sulfide inclusions, will be discussed later.

The brittle fracture of material continues to be a problem of major technological importance and one of the more interesting aspects of brittle fracture is its relation with temperature. When the temperature is decreased many materials undergo a ductile to brittle transition, with the

resulting fracture surface being either of the cleavage or grain boundary type, as revealed by SEM fractographs and by slow bend test and impact test carried out over a range of temperatures. The crack is simply following the path of lowest fracture energy determined by the amount of plastic work plus the true surface energy of the fracture surface. When the temperature is decreased, the dislocation mobility will be decreased, probably without much change in the theoretical fracture stress and this will promote brittle fracture. At the higher temperatures the specimen absorbs much energy as ductile failure occurs, but at the transition temperature, the energy needed to initiate a crack from the notch root which ultimately will lead to the breaking of the specimen suddenly becomes very much smaller. The transition temperature is sensitive to a number of metallurgical variables of which purity and grain size are most important, but with steels, the exact heat treatment also matters much.

Occurance of low temperature brittle fracture is associated with the body-centred cubic metals. This is more pronounced in the presence of impurities which form interstitial solid solutions. The most important element is carbon in  $\alpha$ -iron which, if present to the extent of only a few parts per million, will cause the metal to undergo a ductile-brittle transition.

Sharp yield point in the stress - strain curve is introduced by interstitial impurity atoms. This is a result of the strong asymmetric distortion which these atoms produce in the b.c.c. structures which causes them to have a large interaction energy with the stress fields of dislocations. Strong dislocation locking will take place, so that when plastic deformation occurs it will be either by the sudden avalanche of dislocations which are torn from their solute atmospheres, or by the rapid movement of newly generated dislocations, which have no solute atmosphere. In either case the conditions are suitable for the coalescence of dislocation to form crack nuclei, for the first dislocations to move are acted on by a high stress, and thus will have a high velocity. As the temperature is lowered, the yield stress rises sharply which is again a characteristic of b.c.c. metals. In terms of dislocations this means that Peierls-Nabarro stress in b.c.c. metals is strongly temperature dependent. Consequently, first dislocation to be mobile will move rapidly at lower temperatures, and the chances of forming crack nuclei will increase.

At low temperature, there will be less plastic blunting of the crack due to difficulty in plastic deformation, and propagation will occur more readily.

A brittle fracture is characterized by separation normal to the tensile stress. Outwardly there is no evidence

of deformation. A cleavage fracture appears bright and granular, owing to the reflection of light from the flat cleavage surface. The process of brittle fracture consists of three steps, plastic deformation involving the pile up of dislocations along the slip plane at an obstacle, build up of shear stress at the head of the pile up to nucleate a microcrack, stored energy drives the microcrack to complete fracture without dislocation movement in the pile up. In metals, a distinct growth stage is observed in which increased stress is required to propagate the microcrack.

A ductile fracture is characterized by a cup and cone type separation. Necking begins at the point of plastic instability where the increase in strength due to strain hardening fails to compensate for the decrease in cross-sectional area. The formation of neck introduces a triaxial state of stress in the region. Many times cavities form in these regions and under continued straining these grow and coalesce into the central crack. This crack grows in a direction perpendicular to the axis of the specimen until it approaches the surface. It then propagates along localized shear planes at roughly  $45^\circ$  to the axis to form the cone part of the fracture. The voids which are the basic source of ductile fracture are nucleated heterogeneously at sites where compatibility of deformation is difficult such as inclusions, second phase particles, grain boundaries etc.



The presence of notch in bend specimen can alter the ductile to brittle transition of steel. A notch creates a local stress peak at the root of the notch producing triaxial stresses. Plastic flow begins at the notch root when this local stress reaches the yield strength of the material. Due to this, general yield stress of a notched specimen is greater than the uniaxial tensile stress because it is more difficult to spread the yielded zone in the presence of triaxial stress. The triaxial stress state results in notch strengthening in a ductile metal, but in a material prone to brittle fracture the increased tensile stresses from the plastic constraint can exceed the critical value for fracture before the material undergoes general plastic yielding. Notch also produces high locally concentrated strain. The accompanying strain hardening can lead to ductile void formation that can become converted into brittle cracks.

Figure 40 shows  $J_{1c}$  estimation at room temperatures. For three different crack lengths, a bend test is carried out at room temperature. Despite the existing scatter, the measurements show that  $J_1$  is essentially constant and can be directly used as a design criteria without going through tedious  $J_{1c}$  determination.

### 3.2 TENSILE TEST RESULTS

From the  $J_1$  versus temperature curve, it is observed that there exists a plateau region, i.e., in the temperature range of  $30^{\circ}\text{C}$  to  $230^{\circ}\text{C}$ . There is not much change in the value of  $J_1$  in this temperature range.

Straight tensile tests were carried out at four different temperatures. Some data were taken from previous study. The results are tabulated below:

Temperature, $^{\circ}\text{C}$	% Elongation	UTS ( $\text{MN.m}^{-2}$ )
30	27.09	525
130	20.16	474
180	20.00	505
222	21.20	502
250	22.16	480
400	18.00	388.06
532	10.40	137.2
620	8.20	125.17
700	6.60	96.62

Serrations that appeared in the load-displacement curve over the temperature range of  $130^{\circ}\text{C}$  to  $222^{\circ}\text{C}$  corresponding strain aging gives rise to a plateau in the  $J_1$  versus temperature curve. The occurrence of strain aging is fairly

general phenomenon in metals. The reappearance of the yield point is due to diffusion of carbon and nitrogen atoms to the dislocations during the aging period to form atmospheres of interstitials anchoring the dislocations. Support of this mechanism is found in the fact that the activation energy for the return of the yield point on ageing is in good agreement with the activation energy for the diffusion of carbon in  $\alpha$ -iron.

Serrations arise from successive yielding and ageing while the specimen is tested. If the speed of the dislocation is low, it may be able to move by dragging its atmospheres of impurities along behind it. At higher velocity the dislocation pulls away from the atmosphere and a yield drop occurs. Since the solute atom mobility is high at the temperatures at which discontinuous yielding occurs, new atoms move to the dislocations and lock them. The process is repeated many times, causing the serrations in the stress-strain curves.

For plain carbon steel discontinuous yielding occurs in the temperatures regions of 100 to 300°C. Another interesting aspect of dynamic strain ageing is that when it occurs the yield stress of a metal tends to become independent of temperature. This is evident from the tensile curves plotted at different temperatures.

From previous study, it was clear that the dynamic strain ageing has a direct effect on fracture criterion  $J_1$ . This is the reason for plateau region of  $J_1$  versus temperature plot. The serration disappeared in the stress-strain curves above  $250^{\circ}\text{C}$ . So there is a corresponding change in the fracture curve also.  $J_1$  values again increases sharply above  $250^{\circ}\text{C}$  to  $490^{\circ}\text{C}$ .

Engineering strain at fracture or elongation,  $e_f$  is measured from engineering stress- engineering strain curves obtained at various temperature. Variation of  $e_f$  with temperature is plotted in Fig.41. There is a decrease in  $e_f$  values upto  $220^{\circ}\text{C}$  (dynamic strain ageing region) and then  $e_f$  increases as the temperature increases.

Ultimate tensile strength (UTS) can be obtained similarly from tensile testing curves, and by using the following formula,

$$\text{UTS} = \frac{P_{\max}}{A_0}$$

where  $P_{\max}$  is the maximum load and  $A_0$  is the original cross-sectional area, UTS versus temperature curve is shown in Fig. 41. Subzero values are obtained from the load-displacement curves of slow bend test. There is slight change in UTS values below  $0^{\circ}\text{C}$ , but there is sharp increase in UTS values (ductile-brittle transition region) and after that UTS decreases continually with temperature.

Yield strength (YS) can be obtained by using the following relation[62] :

$$Y = \frac{2P_{\max}S}{BW^2} \times 9.807 \text{ MN. m}^{-2} \quad (41)$$

where Y = Yield strength of the material

$P_{\max}$  = maximum load

S = Specimen bend span

W = Width of the specimen

B = Thickness of the specimen

Now considering stress field present in tensile testing is similar to bend test, we can use this equation for calculating YS.

For bend tests, S = 80 mm, B = 10 mm, W = 20 mm.

Variation of YS with temperature is shown in Figure 41 . At subzero temperatures, YS is almost constant, there is a increase in YS value above 0°C and then it decreases with the increase in temperature.

YS is important when considering the effect of dislocation motion on the fracture of materials, since it is the rate at which a material can deform at a crack tip that determines the effect of plastic deformation on fracture

In recent years controversy has existed concerning the origin of the temperature dependence of yield stress in BCC metals. One group of investigators felt that the temperature dependence of yield stress was an inherent

property of the BCC metals and that attempts to modify it required an alternation in the basic electron building. Another group felt that the temperature dependence was largely due to the interfacial impurities in the metals and that if they were made sufficiently pure, the temperature dependence could be markedly reduced. Strong support for the interfacial impurity argument has developed in recent years and examples of the change in the yield stress at low temperatures with increasing purity has been found in literature, [65]. The problem with using these findings to develop industrial alloys is associated with the trace amounts of impurities that have a strong effect on the low temperature yield stress.

$\epsilon_f$  UTS, YS values obtained at various temperature are tabulated below:

Temperature $^{\circ}\text{C}$	UTS (MN.m <sup>2</sup> )	$\epsilon_f$	YS (MN.m <sup>2</sup> )
-170	80.72	-	66.47
-59	91.30	-	75.188
-21	89.99	-	74.096
-10	88.66	-	73.010
+30	525	0.26	208.398
+130	505	0.2134	188.784
+180	505	0.2000	201.04
+222	502	0.1967	196.14

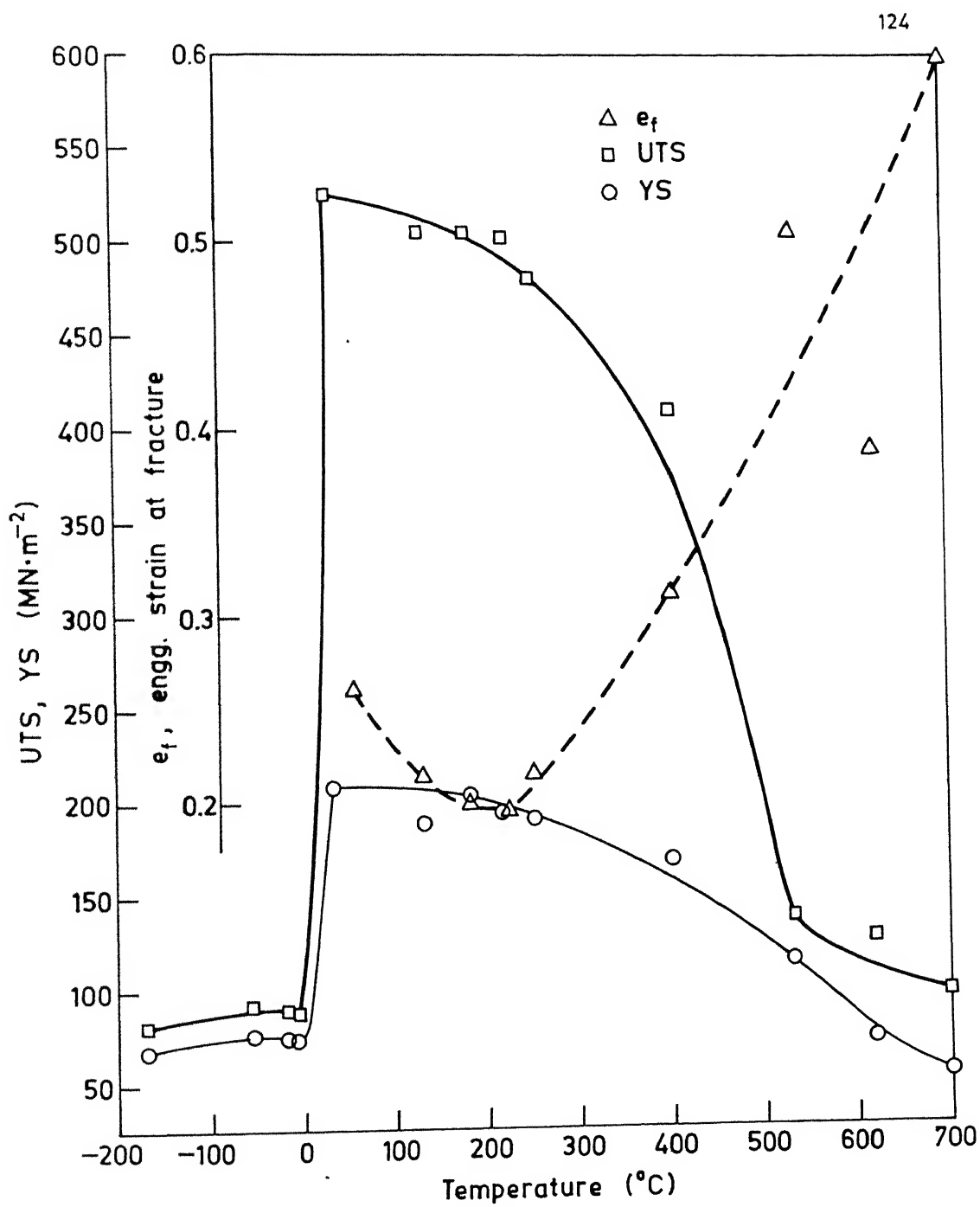
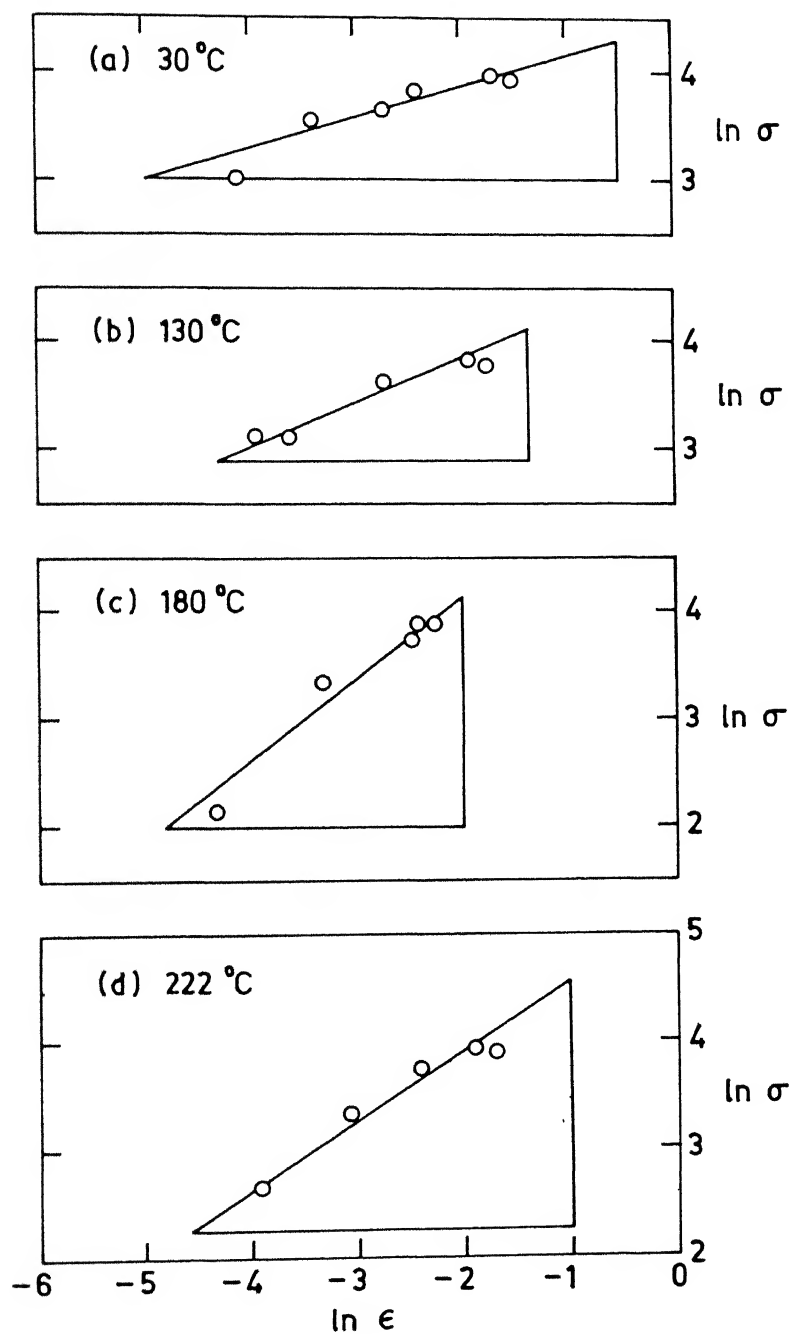


Fig. 41. Variation of UTS, YS,  $e_f$  versus temperature.





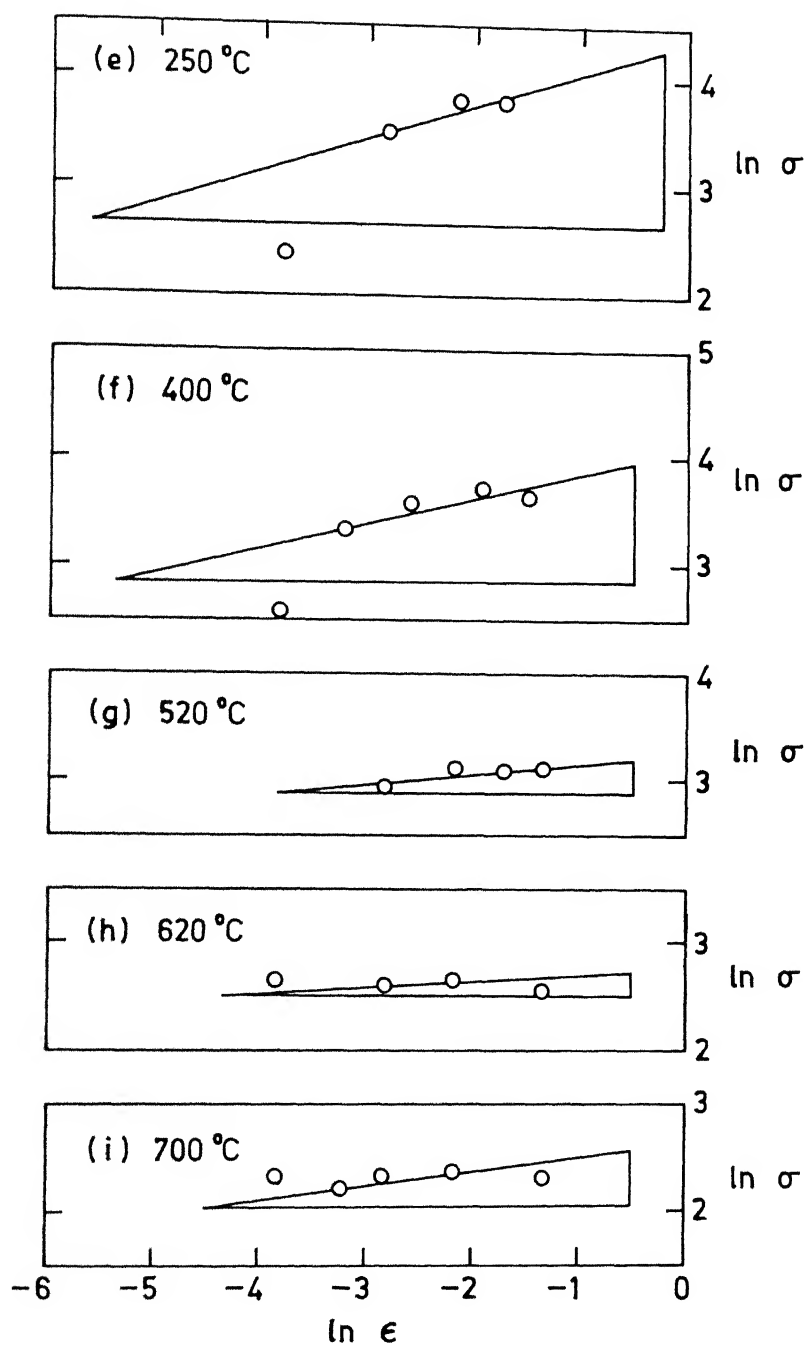


Fig. 42. Determination of  $n$  from  $\ln \sigma$  versus  $\ln \epsilon$  plot.

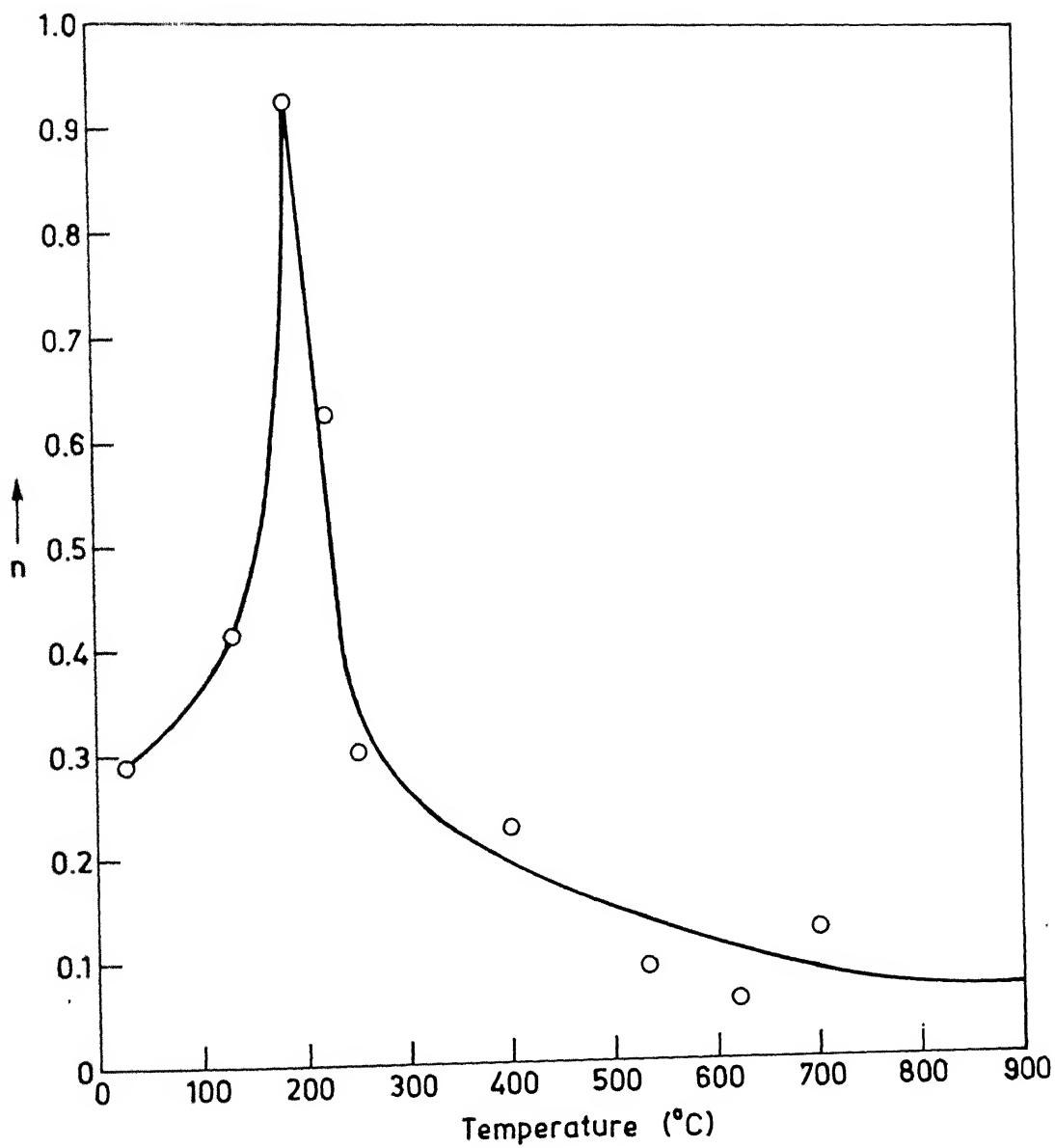
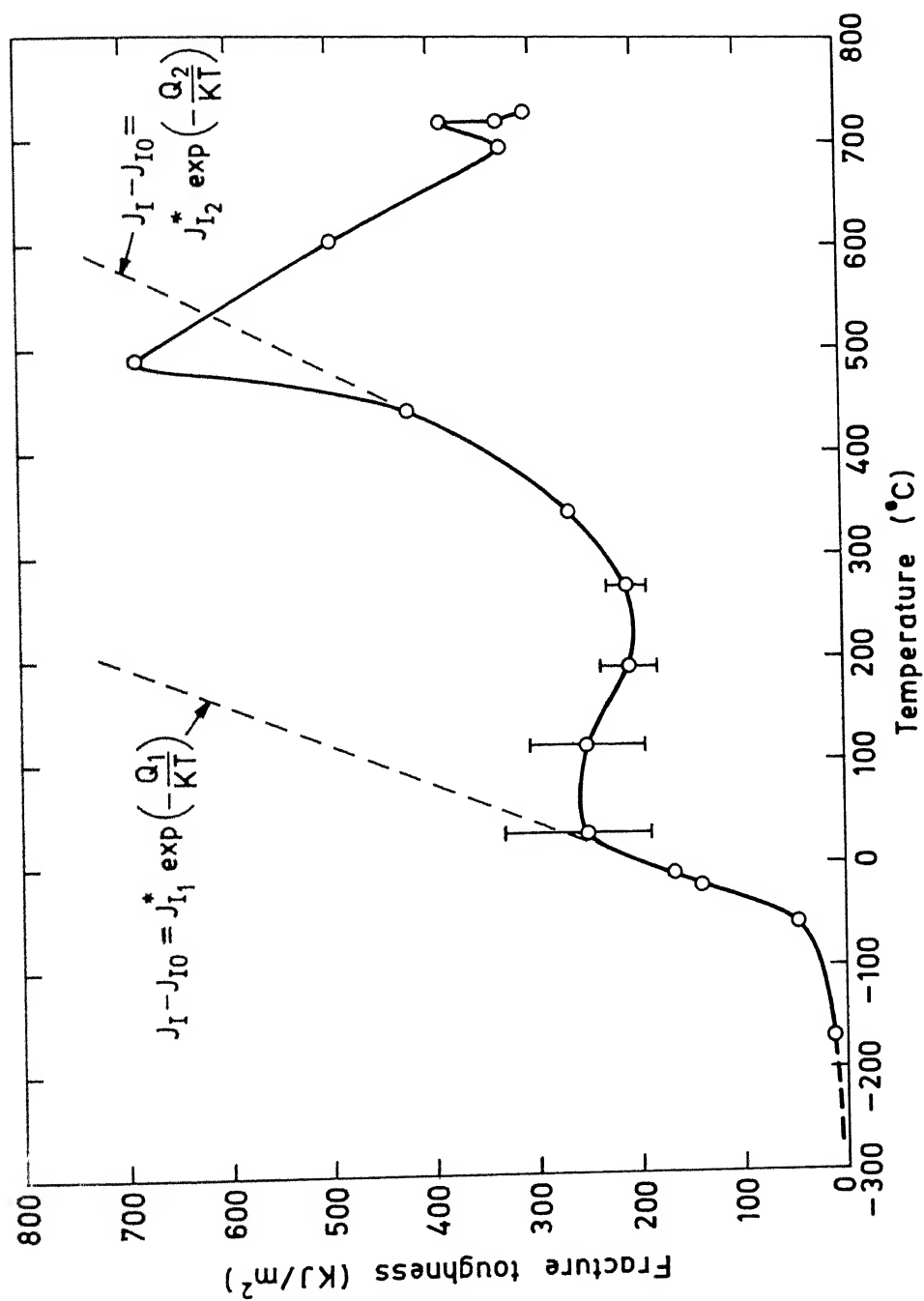


Fig. 43. Variation of  $n$  versus temperature.

Fig. 44a. Variation of  $J_I$  versus temperature.

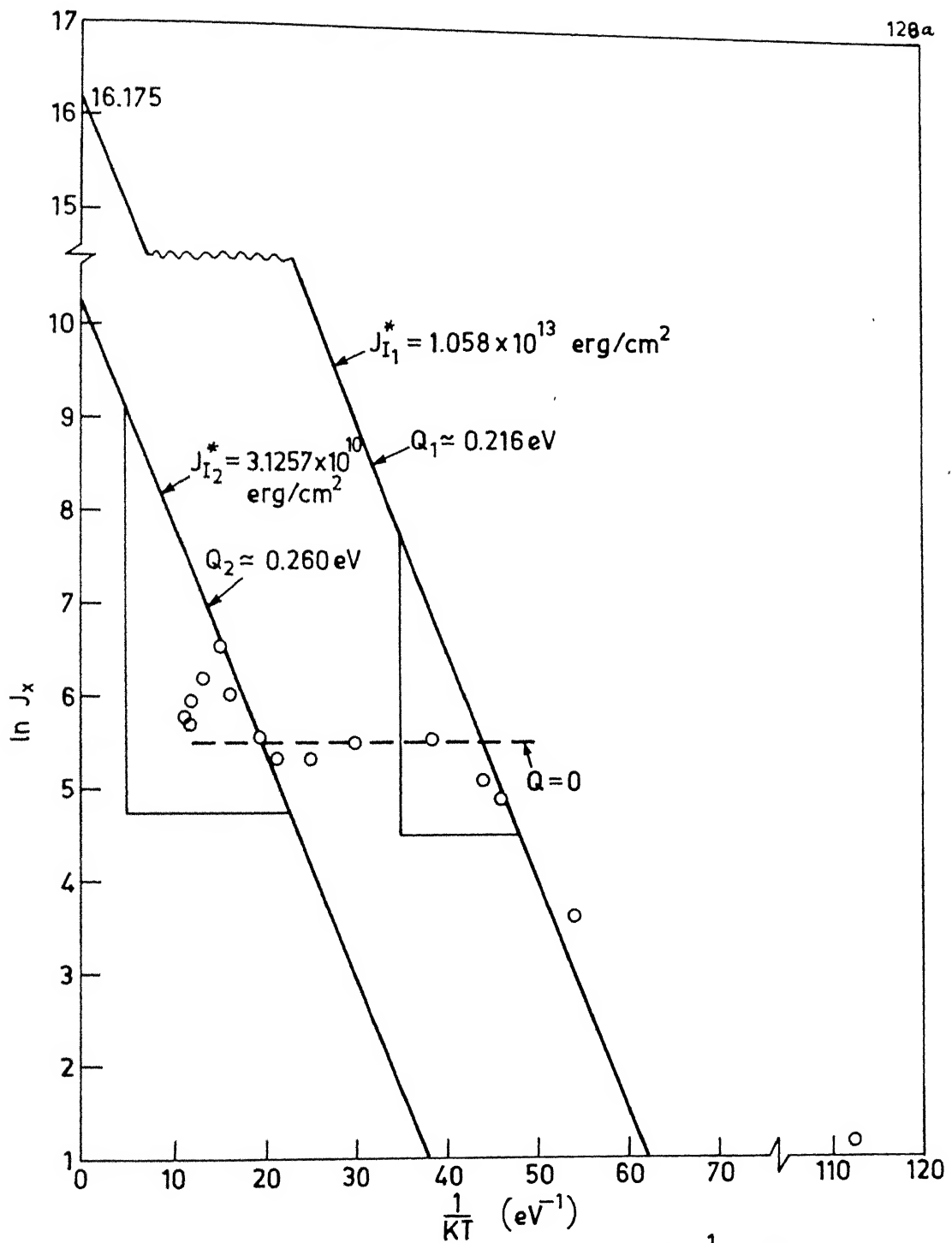


Fig. 44b. Determination of  $Q$  from  $\ln J_x$  versus  $\frac{1}{KT}$  plot.

Temperature °C	UTS (MN.m <sup>2</sup> )	e <sub>f</sub>	YS(MN.m <sup>2</sup> )
+250	480	0.2167	191.22
+400	385	0.3120	167.80
+532	137.2	0.5040	112.978
+620	125.17	0.3880	71.38
+700	96.62	0.5980	52.173

The flow curve of many metals in the region of uniform plastic deformation can be expressed by the simple power curve relation :

$$\sigma = K \epsilon^n \quad (42)$$

where  $n$  is the strain-hardening exponent and  $K$  is the strength coefficient.,  $\sigma$  and  $\epsilon$  are true stress and true strain values

$\sigma$  and  $\epsilon$  can be obtained from engineering stress,  $s$  and engineering strain,  $e$  values according to the following relation

$$\sigma = s (e+1) \quad (43 \text{ a})$$

$$\epsilon = \ln (e+1) \quad (43 \text{ b})$$

Taking  $\ln$  on both sides of equation (42) we get

$$\ln \sigma = \ln K + n \ln \epsilon$$

Log-log plots of true stress and true strain at various temperatures are shown in Figure 42 . The linear slope of these straight line plots is  $n$  calculated for various

temperatures and tabulated below:

---

Temperature ( $^{\circ}\text{C}$ )	n
30	0.2890
130	0.4152
180	0.9240
222	0.6250
250	0.3009
400	0.2245
532	0.0895
620	0.0584
700	0.1250

---

n, strain hardening exponent is plotted as a function of temperature is shown in the Figure 43. It increases with temperature upto  $222^{\circ}\text{C}$  and then it decreases like exponential manner.

### 3.3 IMPACT TEST RESULTS

The principal measurement from the impact energy test is the energy required in fracturing the specimen. The energy absorbed at various temperatures ranging from subzero to as high as eutectoid temperature is tabulated below:

to the plateau region in the  $J_1$  versus temperature plot. This is because of dynamic strain ageing phenomenon which occurs in this temperature range. This phenomenon is also called 'blue brittleness' generally observed in low carbon steels.

It has been found from an earlier investigation that there is a shift in transition temperature from the  $J_1$  versus temperature plot to impact energy versus temperature plot. The shift is from  $-32^{\circ}\text{C}$  to  $55^{\circ}\text{C}$ . This is attributed to vast difference in strain rate effects in two test procedure about  $10^4 \text{ sec}^{-1}$  in CVN and only  $6.67 \times 10^{-4} \text{ Sec}^{-1}$  in bend test. Therefore, it is clear that one has to be careful in using fracture toughness obtained from different test procedures. After  $400^{\circ}\text{C}$ , there is increase in impact energy values upto  $730^{\circ}\text{C}$ .

### 3.4 COMPOSITE CURVES

From CVN values,  $K_1$  values are calculated as follows:

$$K_1 = A(\text{CVN})^{1/2} \quad (44)$$

where  $A$  is a constant having the dimension of  $\text{N}^{-1/2} \cdot \text{m}^{-2}$  and its numerical value depends on the test procedure and type of steel.

The relation between  $K_1$  and  $J_1$  is as follows:

$$J_1 = (1 - \nu^2) \frac{K_1^2}{E} \quad (45)$$

where  $\nu$  is the poisson's ratio and E is the modulus of elasticity. Putting the value of  $K_1$  from equation we have,

$$J_1 = (1 - \nu^2) \frac{[A(CVN)^{1/2}]^2}{E} \quad (46)$$

We can extrapolate the J versus T and CVN versus T curves to find out the value of J and CVN at  $0^\circ\text{K}$ . Since at  $0^\circ\text{K}$ , material is perfectly brittle, it is reasonable to compare  $J_1$  and CVN.

Now  $J_1 = 7.5 \text{ KJ. m}^{-2}$  at  $0^\circ\text{K}$  from direct measurement of  $J_1$  from bend test,

$$\nu = \frac{1}{3}$$

CVN = 3 Joules at  $0^\circ\text{K}$  from CVN test

$$E = 2.07 \times 10^{11} \text{ N.m}^{-2}$$

A comes out to be  $4.04 \times 10^6 \text{ N}^{1/2}.\text{m}^{-2}$ . So the equation(46) becomes,

$$J_1 = 2.5 \times 10^3 \text{ CVN} \quad (47)$$

$K_1$  values can be calculated from the  $J_1$  (obtained from experiment) values according to the equation(45). We can rewrite the equation as,

$$K_1 = \left[ \frac{J_1 \cdot E}{1 - \nu^2} \right]^{1/2} \text{ MN.m}^{-3/2} \quad (48)$$

Using the equation (47) we can calculate converted  $J_1$  and datas are tabulated below:



---

Temperature °C	CVN(J)	Converted $J_1$ from CVN (KJ .m <sup>-2</sup> )
<hr/>		
-130	5.42	13.55
- 70	8.14	20.35
- 36	10.85	27.13
- 9	12.20	30.50
+ 30	35.26	88.15
+100	78.64	196.60
+200	78.64	196.60
+300	100.00	250.00
+400	50.00	125.00
+500	56.00	140.00
+600	76.00	190.00
+730	108.00	270.00

---

Using the equation (48) we can calculated  $K_1$  from experimental  $J_1$  values and datas are tabulated below:

Temperature, °C	Experimental $J_1$ (KJ.m <sup>-2</sup> )	$K_1$ (MN.m <sup>-3/2</sup> )
-170	12.82	54.63
- 59	45.01	102.78
- 21	140.07	180.60
- 10	168.92	198.33
+ 28	255.00	243.68
+115	250.00	241.28
+190	209.71	220.98
+276	210.00	221.14
+340	268.59	250.09
+440	424. 1	314.52
+490	689.023	400.56
+603	499.75	341.14
+693	328.78	276.70
+717	388.98	300.97
+718	332.49	278.25
+727	306.59	267.20

CVN versus temperature and  $J_1$  versus temperature graphs are shown in Fig. 38 and Fig. 37 respectively. Fig. 37 also shows converted  $J_1$  versus temperature and converted  $K_1$  versus temperature graphs.

The nature of the three curves is similar upto a certain temperature. The scatter in the value is due to various factors, will be discussed in the next section.

One of the reason for the scatter in converted  $J_1$  and experimental  $J_1$  values is discussed below.

Converted  $J_1$  values are actually dynamic  $J_1$  values whereas experimental  $J_1$  values are obtained from slow bend test, so bend test gives static  $J_1$ . The dynamic and static values [32] related to each other by the following expression

$$J_1 \text{ (dynamic)} = \frac{1-\alpha}{1+\alpha} J_1 \text{ (static)}$$

where  $\alpha$  is called relative crack speed and given by  $\alpha = \frac{\dot{a}}{C_0}$  where  $\dot{a}$  is the crack speed and  $C_0$  is the speed of sound in metals.

### 3.5 EFFECTS OF HEAT TREATMENTS AND OPTICAL MICROSCOPY RESULTS

Fig. 45 shows the effect of heat treatment on the room temperature values of  $J_1$ , which shows that depending upon the heat treatments a two to three fold increase in fracture toughness is possible. Some of the heat treated and bend tested samples are presented in Fig. 47, showing that plastic deformation is concentrated essentially in the vicinity of crack tip supporting some of the basic assumptions in the theories of fracture.

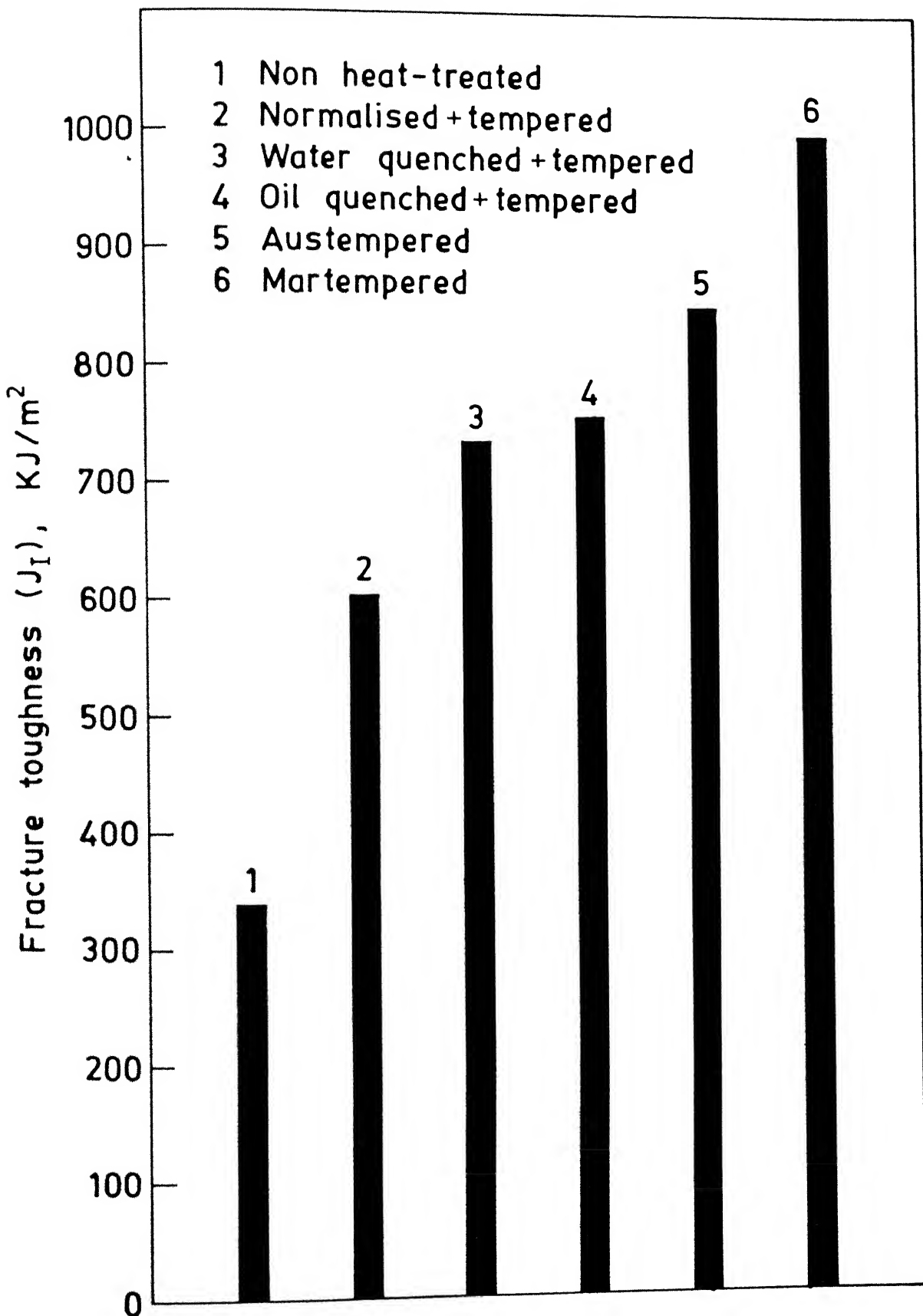
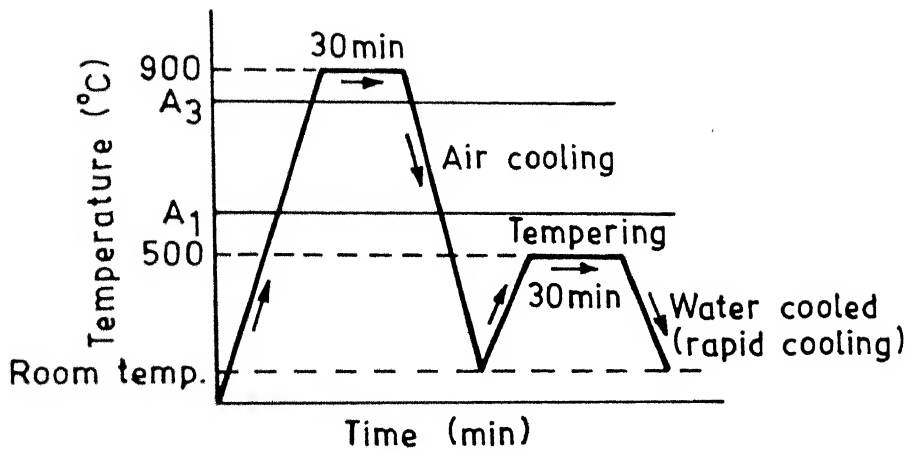
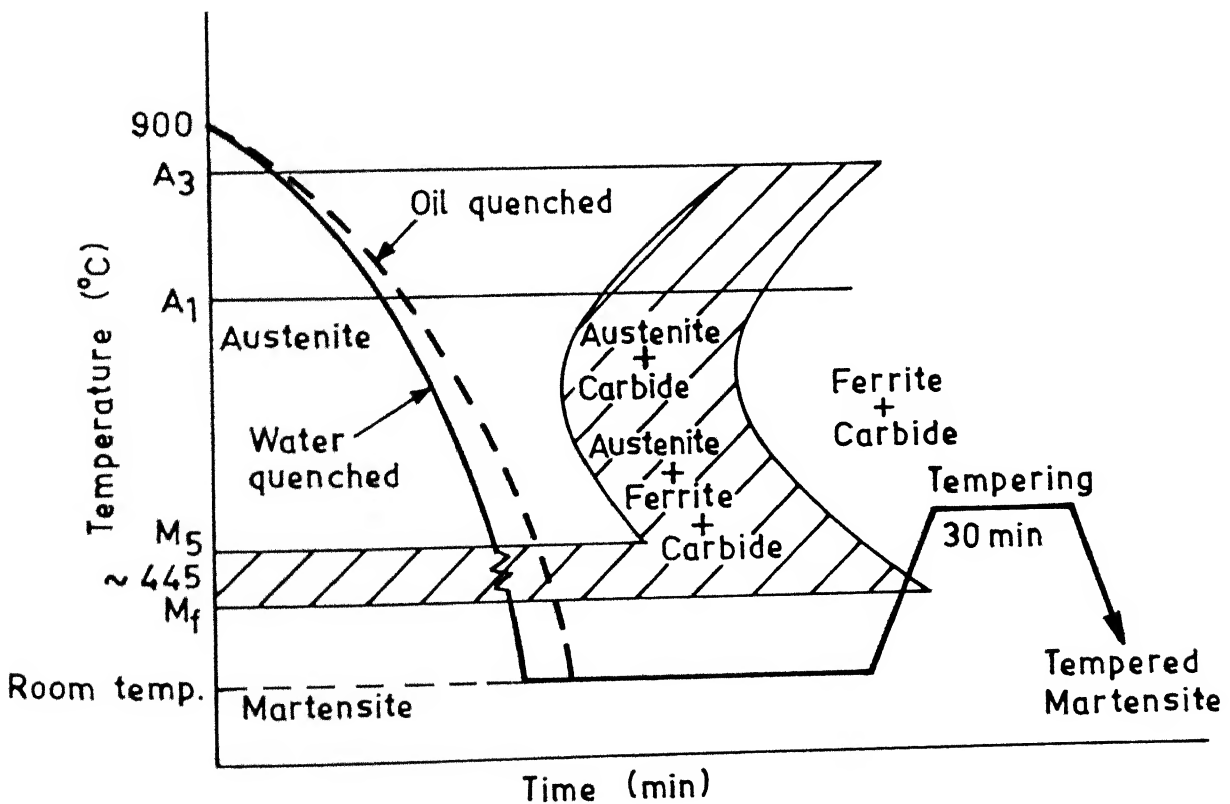


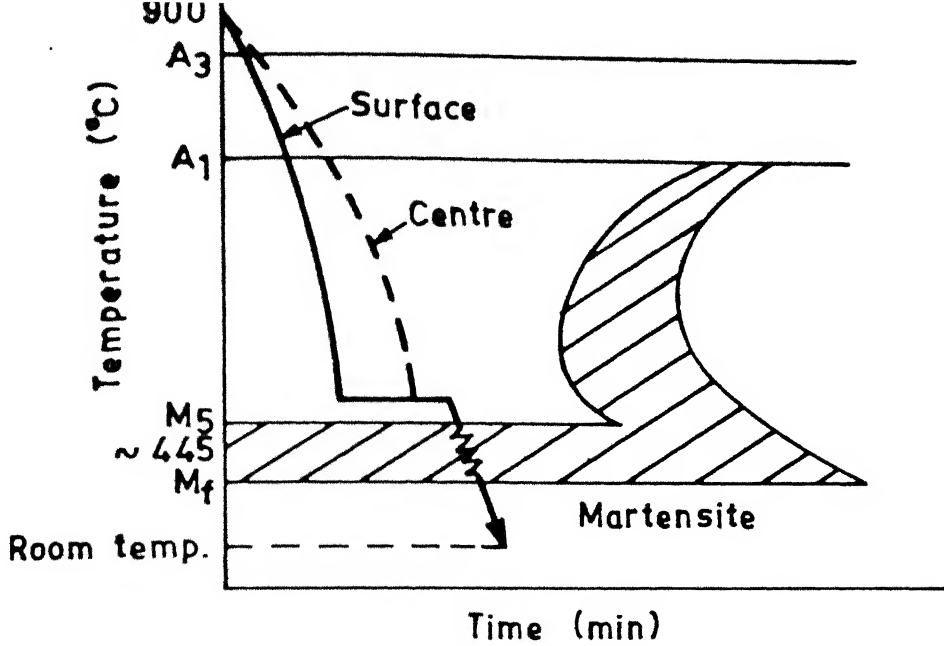
Fig. 45. Variation of fracture toughness ( $J_I$ ) with different heat-treatments.



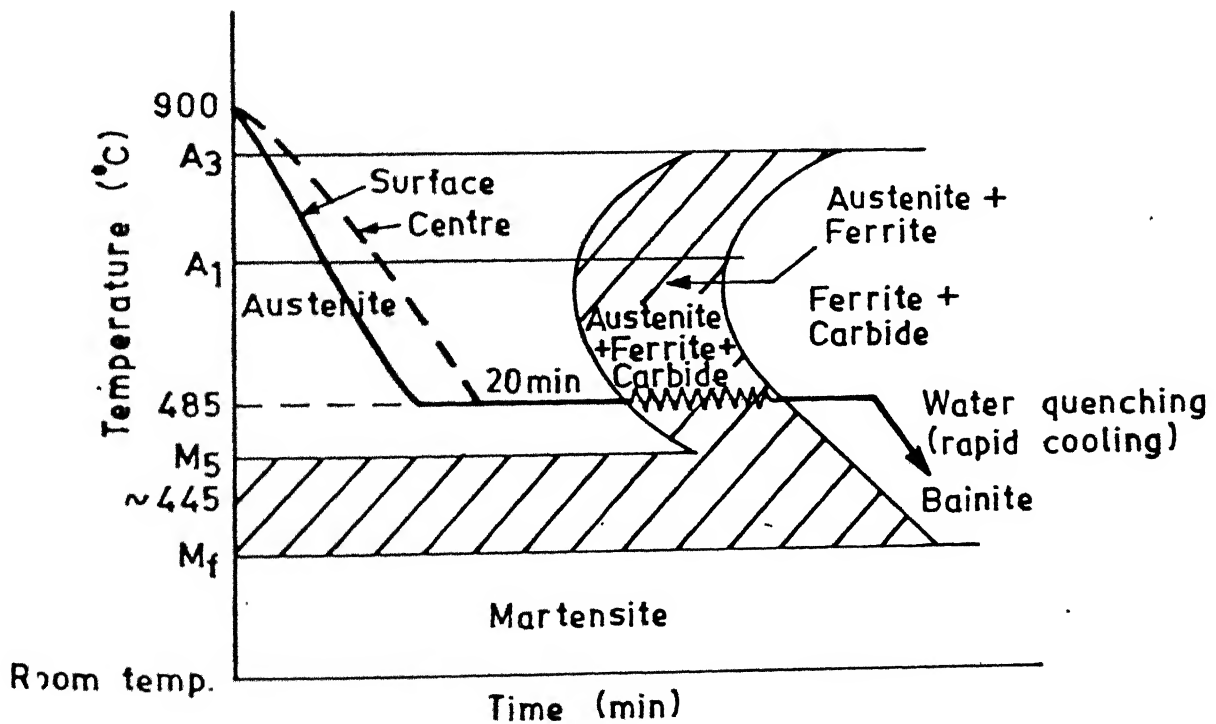
(a) Normalizing followed by tempering



(b) Water and oil quenching followed by tempering



(c) Martempering

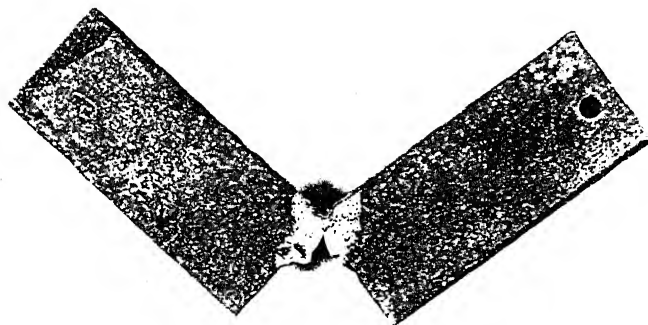


(d) Austempering

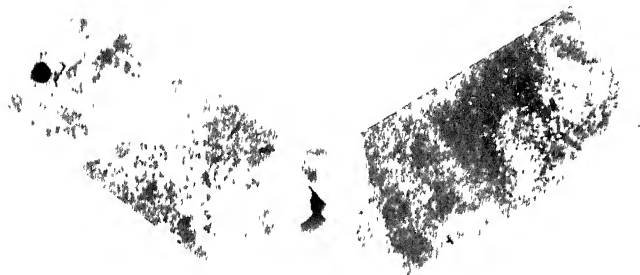
Fig. 46. Model heat-treated cycles employed for present study.



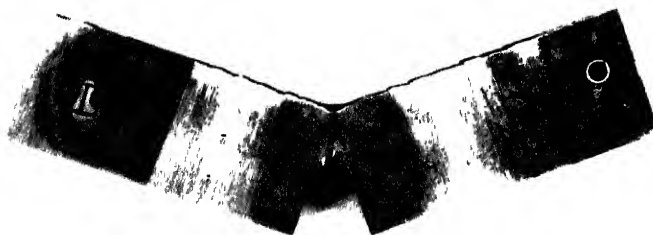
(a)



(b)



(c)



(d)

Fig.47 Three point bend tested samples for  $J_I$  -estimation  
(a) as received, (b) normalized, (c) austempered  
(d) martempered.



Fig. 46 shows model cycles employed for heat treatments for our present study.

$M_s$  temperature determined according to the following relation,  $M_s (^{\circ}\text{C}) = 550 - 350\%C - 40\%Mn - 20\%Cr - 17\%Ni - 35\%V - 10\%Cu$ .

As discussed in the literature, normalized steels show an improvement in the fracture toughness as a result of phase recrystallisation which produces a more dispersoid ferrite/cementite conglomerate with an overall improvement in mechanical properties.

Quenching followed by tempering helps in reducing brittleness and stress due to hardening. The formation of tempered martensite helps in improving fracture toughness value. Quenching followed by high temperature tempering as employed in our study, raises the tensile strength, yield point, reduction in area, besides toughness. High temperature tempering followed by rapid cooling can avoid temper brittleness.

In martempering, fracture toughness improves considerably and there is a less danger of crack propagation owing to the presence of greater amount of retained austenite and possibility of self-tempering of martensite.

Best fracture toughness can be obtained by producing lower bainitic structure in austempering, but in our present study it is lower than in martempering. This is due to

insufficient cooling rate during experiment. Salt bath furnace containing mixtures of 55% Potassium Nitrate and 45% sodium Nitrite cannot produce the cooling rate required for producing completely bainitic structures. So a mixture of phases are produced.

### 3.5.1 Effect of Microstructure on Transition Temperature

At a given strength level, the transition temperature of a steel is determined by its microstructure [6]. For example, if the major microstructure constituents found in steels, ferrite displays the highest transition temperature, followed by pearlite, upper bainite and finally lower bainite and tempered martensite. The transition temperature of each of these constituents varies from the temperature at which the constituent formed and where applicable, the temperature at which the steel was tempered. In practice, the cooling or quenching rate and time temperature transformation characteristics of a steel (including the conventional hardenability) determine the resulting microstructure or mixture of microstructures. The transformation characteristics, in turn, are controlled by the alloy composition, austenizing temperature and austenite grain size. Generally, treatments that produce microstructures with inferior room temperatures fracture toughness also raise the transition temperature. Isothermally transformed lower bainite has superior fracture toughness, and a slightly lower transition

temperature, than tempered martensite. However, mixed structures, which result from incomplete bainitic treatments causing partial transformation to martensite, have lower fracture toughness and much higher transition temperature than either 100% tempered martensite or 100% lower bainite. Thus it is important that bainite treatments be carried to completion to avoid the adverse effects of mixed structure.

### 3.6 ELECTRON MICRO PROBE ANALYSER AND SCANNING ELECTRON MICROSCOPE RESULTS AND EFFECTS OF MICROSTRUCTURE ON FRACTURE TOUGHNESS

From the photographs in Fig. 48, we can observe the distribution of micro-constituent elements.  $MnK\alpha$  and  $S-K\alpha$  X-Ray image show the distribution of sulfur in the form of manganese sulfide and phosphorus in the form of manganese phosphide or compounds of both,  $MnSP_2$ . These elements have deleterious effects on the mechanical properties especially toughness. The corresponding microstructure shows the presence of inclusions and crack nucleation zone at room temperature.

Secondary electron image of two spots show at room temperature that fracture is predominantly brittle with some void formation.

Cleavage fractures is produced at low temperatures, under a condition of high triaxial stress that is, at the root of the notch . It is typically of b.c.c. metals.

It is apparant from room temperature SEM fractographs that fracture plane changes orientation from grain to grain. The change of orientation from grain to grain leads to a very chaotic overall appearance of the fracture surface. The origin of the main crack may be carbide particles at grain boundary present in microstructures of HSLA steel. From the particle, which is small, crack propagated through the surrounding grains by cleavage.

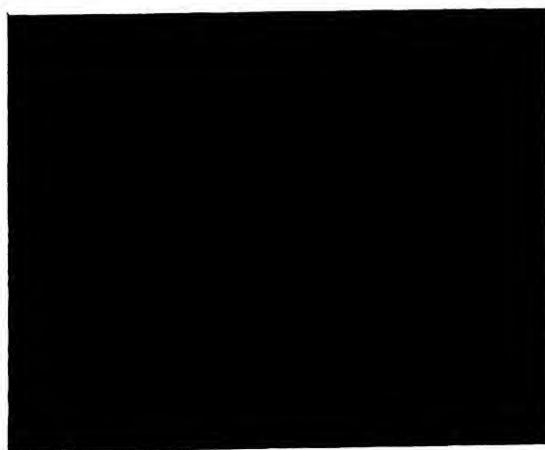
Quenched and tempered microstructure showed that failure occured by void nucleation, growth and coalescence. Microvoids are initiated at oxide and sulfides inclusions, carbides and also at imperfections such as microporosity and microcracks. Some of the voids spaced closely enough to impinge upon one another . The fractographic examination indicated that these linking mocrocracks occured locally as mode I opening cracks. The presence of particles may also assists void formation by providing a surface of low cohesive strength which separates by tension, or by undergoing fracture with the halves of the fractured particles moving apart by plastic flow of the matrix. The individual voids then join by necking of the matrix material between the voids. There



(a)

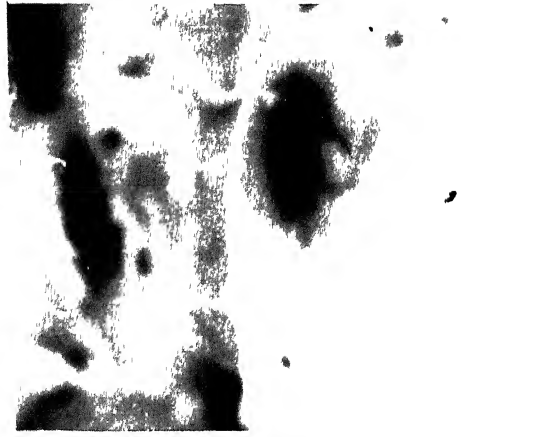


(b)



(c)

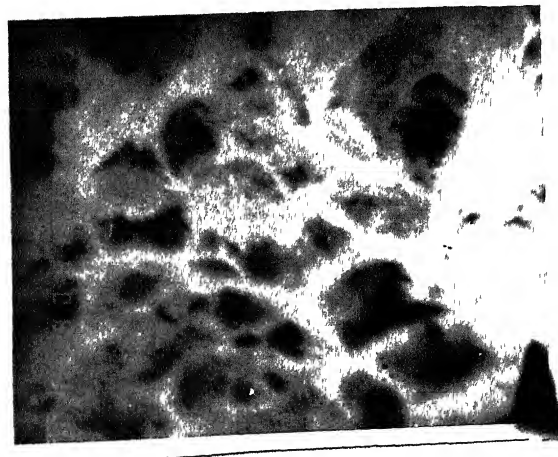
Fig.48 SEM fractographs from three point bend tests at room temperature showing fracture characteristics with electron microprobe  $K\alpha$ -X-Ray intensity mapping (a) SEI, R.T. (b)  $Mn - K\alpha$  (c)  $S - K\alpha$ .



(d)



(e)

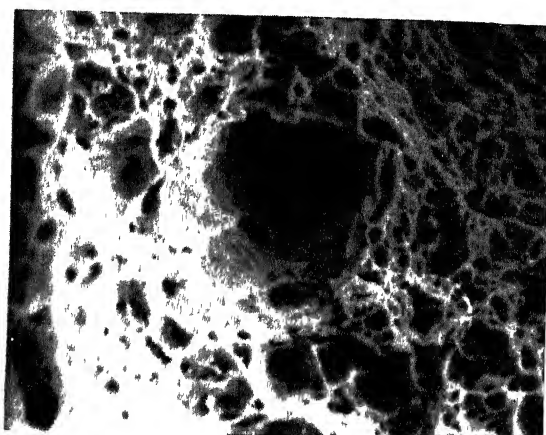


(f)

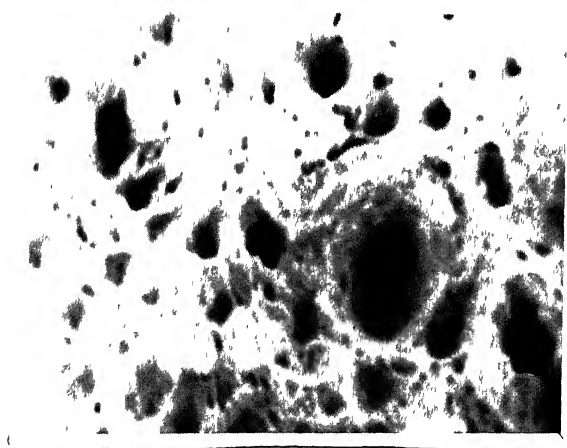
Fig.48 SEM fractographs from three point bend tests at room temperature (d) BEI (e) SEI of same spot (f) at 210°C, SEI.



(g)

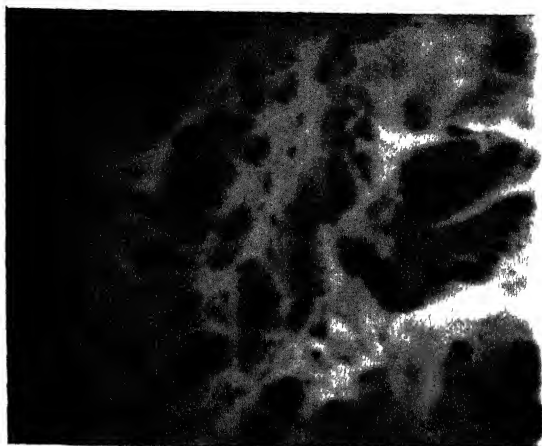


(h)

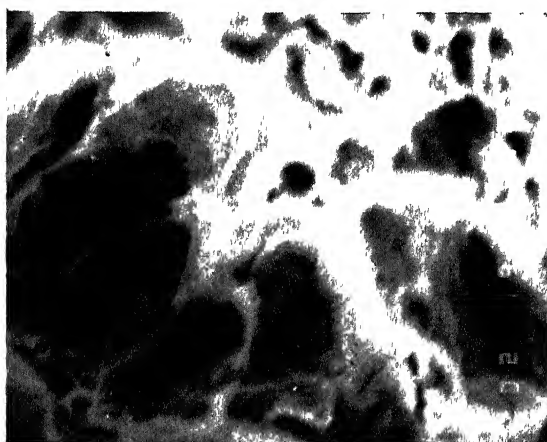


(i)

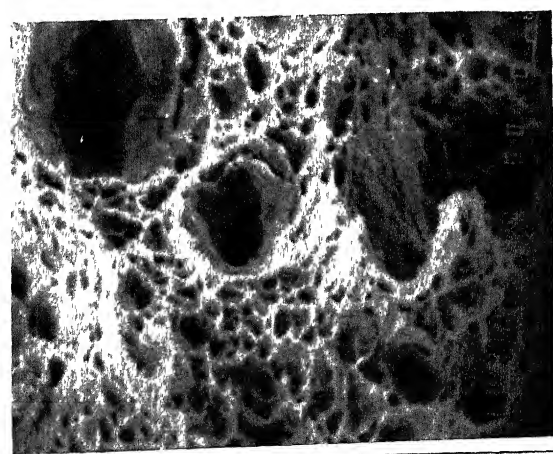
Fig. 48 SEM fractographs from three point bend tests at  
(g) 730°C, SEI (h) Water quenched and tempered, SEI (i) oil  
quenched and tempered, SEI.



(j)



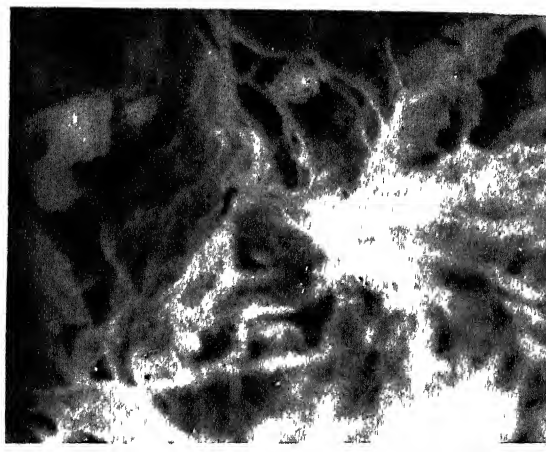
(k)



(l)

Fig.48 SEM fractograph from three point bend test (j) Normalised and tempered, SEI (k) Martempered, SEI (l) austempered, SEI.





(m)

Fig.48 SEM fractograph from three point bend test (m) austempered, SEI of another spot.

is general plastic flow throughout the whole specimen before fracture occurs.

Martempered structure shows the presence of dimples formed by second phase particles.

Austempered structure shows fine distribution of dimples commensurate with the fine scale distribution of carbides, carbonitrides, sulfides etc. Secondary electron image of austempered structure of different spot shows presence of cleavage facet, making the fracture quasicleavage.

Normalised and tempered fractograph shows dimpled structure slightly distorted forming a network. The dimples are of the type of tear dimples. The elongated microvoids that become tear dimples are formed in a narrow band just ahead of a well developed crack front. Some cleavage facets also observed in this fractograph.

In ductile fractures, size and shape of dimples are seldom uniform. In engineering materials with an appreciable variation in size and shape of the precipitate particles, dimples may exhibit a wide range of dimensions.

The occurrence of mixed fractures usually indicates that interacting influences have caused the fracture to depart from either limiting mechanism. Grains with different orientation may have lower resolved normal stresses and can undergo plastic deformation and exhibit a ductile mechanism of fracture -often dimple formation by microvoid coalescence.

Treatments that produce microstructures with inferior room temperature fracture toughness raise the transition temperature. Spherodization treatments can improve fracture toughness by reducing strength and by eliminating ferrite plates, which are paths of easy cleavage fracture in pearlite. Presence of austenite inhibits the fast propagation of cleavage fracture in some ferritic and martensitic steels.

### 3.7 EFFECTS OF NON METALLIC INCLUSIONS ON FRACTURE TOUGHNESS

Discontinuities in the form of inclusions, such as oxides, sulfides have been identified as initiation sites of ductile fractures in steel by several investigator [66] and evident from our fractographs. At relatively low strains, microvoids form at inclusions, either by fracture of the inclusion or by decohesion of matrix-inclusion interface. With additional straining, the microvoids grow to the size represented by the large dimples. During final fracture, many small dimples formed at fine particles. SEM fractographs consist of many large, shallow dimples mixed with small dimples, that appear to have been nucleated during the fracture process by numerous, relatively coarse sulfide particles. Many small dimples were nucleated by small carbide particles.

Nonmetallic inclusions usually form from deoxidation products or slag, but may also result from the intentional addition of elements such as sulfur to enhance machinability.

Among the different types of inclusions, as discussed earlier, sulfides is one of the most harmful in decreasing the value of fracture toughness. Both globular and stringered ( i.e. elongated) inclusions have a detrimental effect on reduction of fracture toughness, it is much more severe for stringered inclusions than the globular inclusions. Stringered sulfide inclusions help in promoting elongated dimples, as is evident from our fractographs, in contrast to the more equiaxed ones. X-Ray microanalysis showed presence of  $MnS$  and  $MnSP_2$  in the presently investigated steel. Some of the inclusion nucleated voids spaced close enough so that they impinged upon one another. Above the DBTT, the flow stress is lowered so that plastic relaxation at the microcrack tip prevents the achievement of the critical stress intensity for cleavage. Then the microcrack distorts into void that grows and eventually links with the main crack. In the latter case, the microcrack can occur either by through-particle cleavage or by decohesion of the particle-matrix interface.

Elongated sulfide inclusions can result in longitudinal cracking along inclusions, whilst bending normal

to rolling direction gives excellent bends.

Cavitation commonly occurs by decohesion of the interface between interface and matrix although inclusion itself may suffer subsequent damage by virtue of secondary (compressive) strains. Interface decohesion is associated with non-metallic inclusions occurs at very small strains, suggesting that interface has low mechanical strength.

During straining at room temperature, the nucleation of cavities is often observed to occur either by particle cracking or by decohesion of particle -matrix interface. In case of carbides such as lamellar cementite in ferrite matrix, the cavitation is commonly one of carbide cracking.

Normalised and tempered fractograph show sulfides are broken with some deep cavity.

Energy associated with elongated inclusion-matrix interface becomes extremely large and can result in partial spheroidisation of inclusion during heat treatment. This ability of elongated sulfides to spheroidise at elevated temperature reduces their detrimental effect and it has been found that substantial improvement in toughness achieved by the use of heat treatments.

As the yield strength of the steel decreases with increasing tempering temperature, the plastic zone size

increases and there is increased opportunity for fracture to propagate along austenite grain boundaries. Eventually zone size becomes greater than the austenite grain size and a fully faceted structure may then occur if sufficient grain boundary embrittlement has occurred. These facets consists of numerous fine ductile dimples which are nucleated by very fine particles of MnS.

So we see, fracture of sulfide inclusions appears to play a key role in initial crack extension, both by cleavage and ductile dimpled rupture.

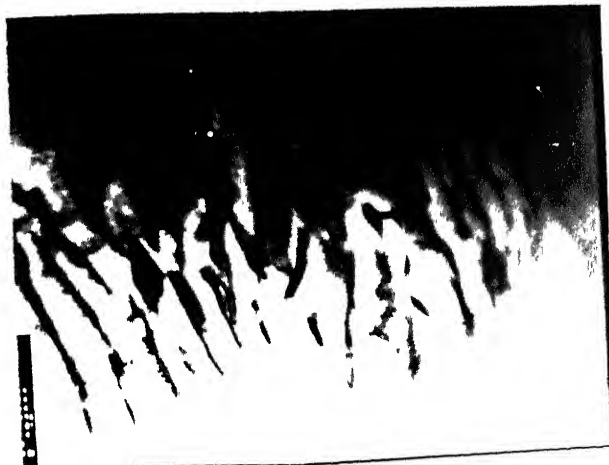
### 3.8 TRANSMISSION ELECTRON MICROSCOPY RESULTS

TEM photographs have shown in Fig. 49 for CVN samples and Fig. 50 for bend samples. Some of the features identifiable from these photographs.

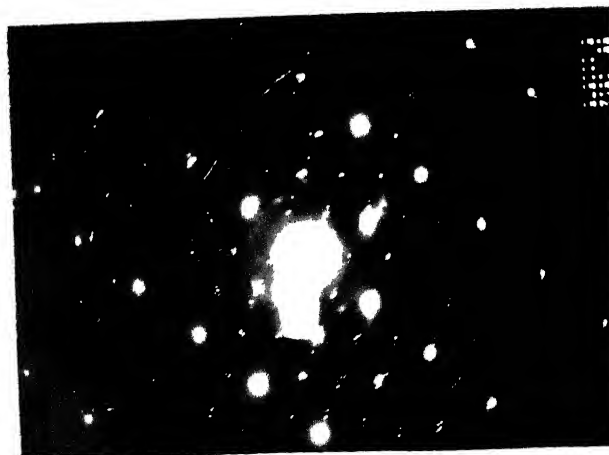
Study of dislocation has been intense over recent years since their properties govern the mode of plastic flow in crystals. In electron microscope, dislocations can be revealed as a result of certain diffraction conditions arising from the displacement of the atoms from their positions around the dislocation line. With an edge, the displacements produce compressive strains above the dislocation line, and tensile strain at the bottom of the dislocation line. For screw dislocations the displacements produce a helical strain field. In general dislocation is characterized by the magnitude and direction of the slip movement



(a)



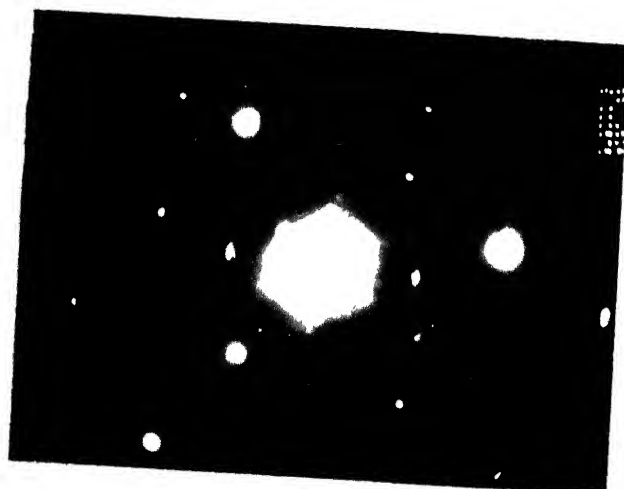
(b)



(c)



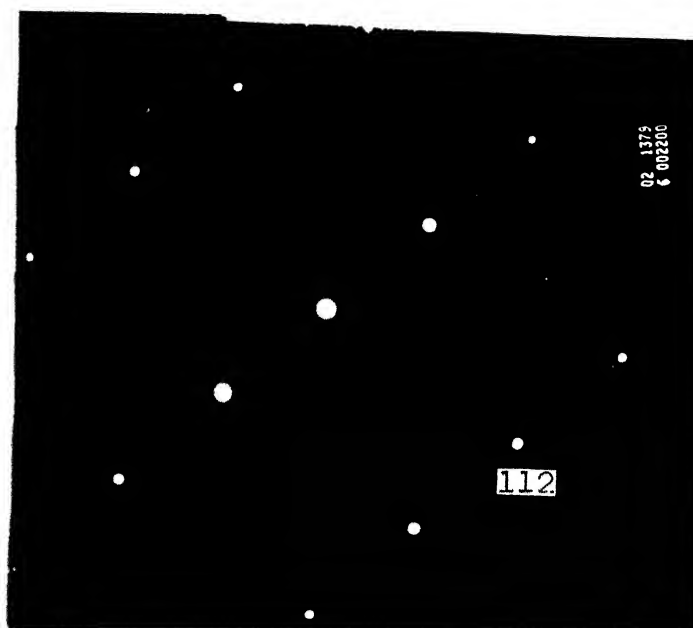
(d)



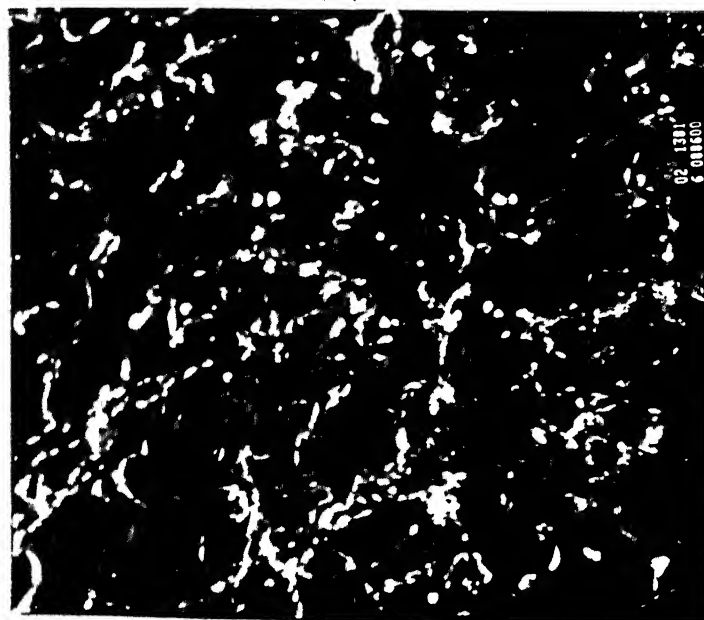
(c)

Fig.49 Transmission electron micrographs showing microstructures from CVN tests at room temperature, (a) to (c), and at 730°C, (d) to (e).

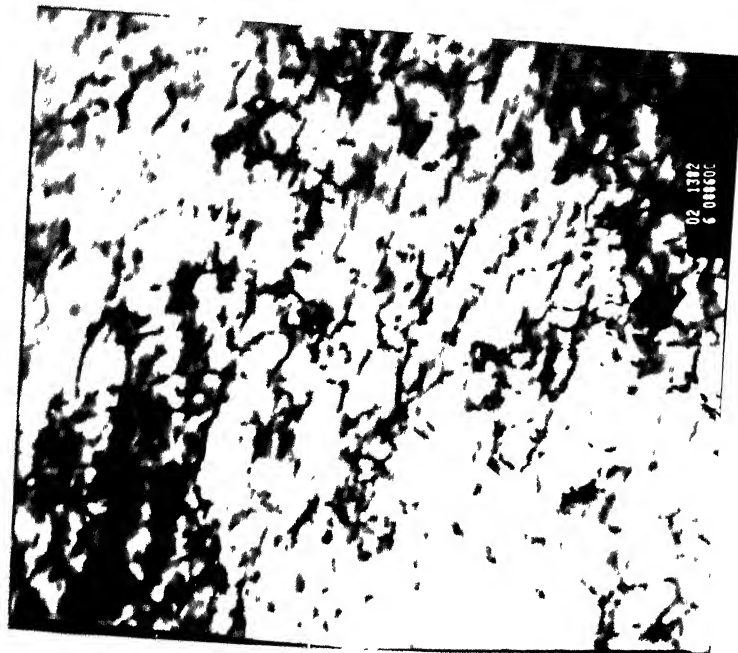




(a)



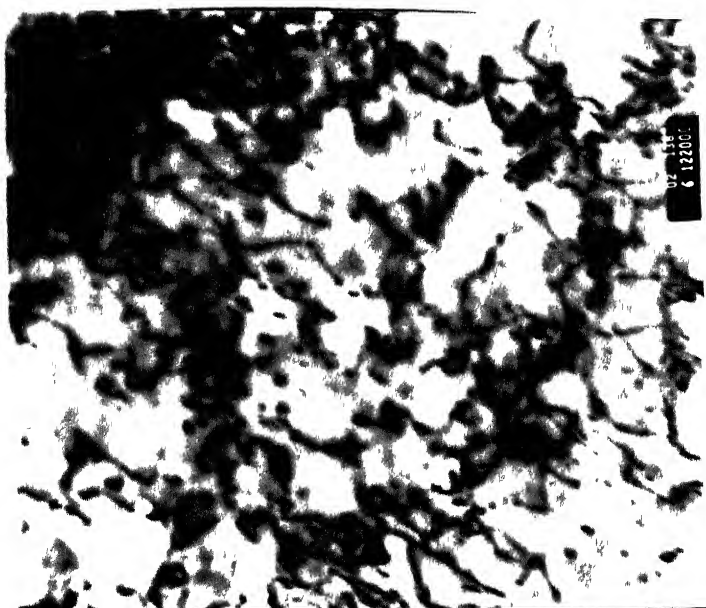
(b)



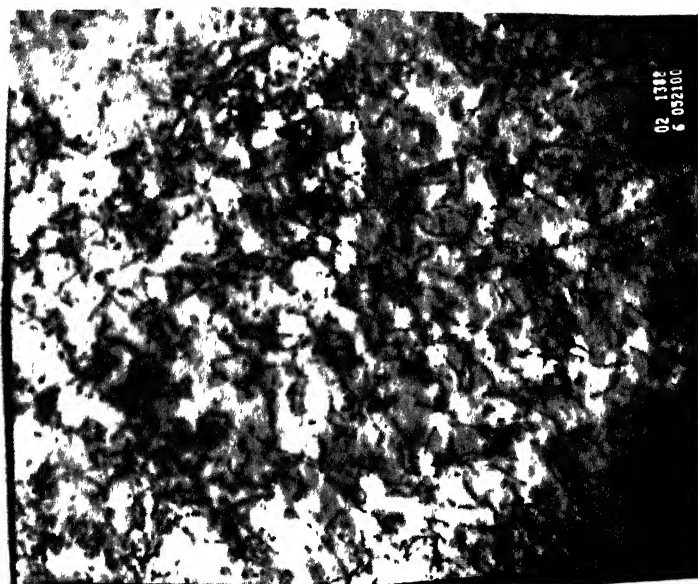
(c)



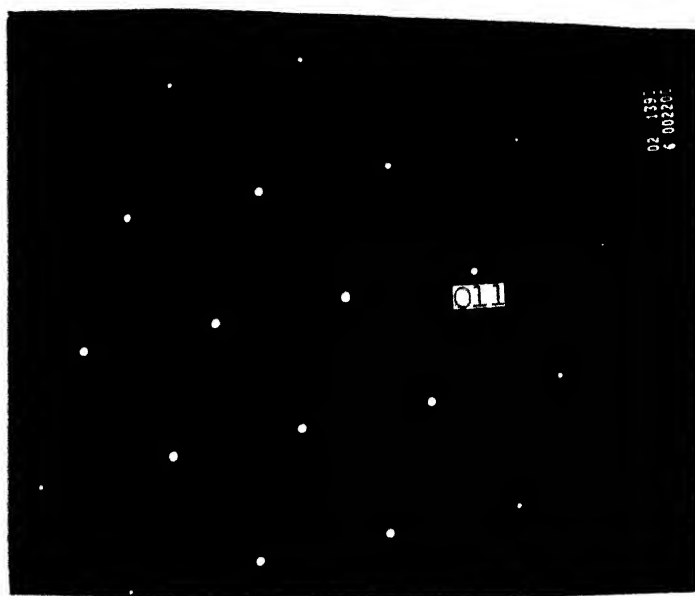
(d)



(e)



(f)



(g)

Fig.5C Transmission electron micrograph showing microstructure from three-point bend tests at room temperature (a) SADP from Non-Pearlitic region (b) DF image (c) Same area as (b), B.F. image (d) area of small precipitates (e) another area of precipitate (f) same area as (e), lower magnification (g) SADP.

associated with it, i.e., the Burgers vector.

Because of the difficulty of cross-slip, dislocations in metals of low stacking fault energy will tend to pile up against any obstacles in their path e.g., any precipitate present or grain boundaries, as is evident from Fig. 49. In the bright field image, because of Bragg contrast, they appear as black lines whereas contrast is reversed in the dark field image.

Theories of flow stress and work hardening depend on the particular dislocation distribution which is assumed to exist in the cold worked metals. Dislocation pile-ups are assumed with the formation of immobile lengths of Lomer-Cottrell locks and these are barrier to the glide dislocations. In our steel, pile ups and dislocation interactions producing these locks have been observed. Type of dislocation distribution is determined by the stacking fault energy of the metal or alloy being considered. Pile-ups are definitely known to occur with metals of low stacking fault energy. More recently, as a result of electron microscope investigations, attention is being paid to the importance of jogs on dislocations. During glide many dislocation loops are formed as a result of the cross-slip of screw dislocation at jogs when they are held up at an obstacle.

Distribution of dislocations in our present study is different in each group and can be summarized. In groups

(i) pile-ups, stacking faults, complex networks, deformation twins are produced (ii) dislocation occur in irregular network which build up into a cell structure with increasing deformation. This cell structure consists of boundaries containing a high density of dislocations separated by regions which are relatively dislocation free.

Generally speaking, dislocations in b.c.c. metals are arranged either in regular or irregular networks. Networks are formed by the interaction of dislocations. In this way subboundaries and sessile dislocations can be found. Nucleation of dislocations can occur at grain boundaries, twin boundaries, polygonization walls, precipitates and during glide.

In b.c.c. metal many slip systems may operate during deformation, and by using selected area diffraction (SAD) technique it is possible to examine this in some detail.

(SADP) in Figure 49c, samples taken from room temperature CVN tests, shows ferrite twinning which appears to be dominant mode of deformation at ambient temperatures under impact loading though the exact transition temperature has not been determined, twinning does not appear at higher temperature say beyond  $400^{\circ}\text{C}$ . The SADP sample taken from CVN test at  $730^{\circ}\text{C}$  after cooling to room temperature, shows diffraction spots from a cluster of precipitate particles

of different micro-constituents. The diffraction spots can be indexed according to (i) very strong spots-ferrite, (ii) the central set of spots with medium intensity arranged as two inverted equilateral triangles and other related spots with appropriate symmetry- two NbC (cubic), particles with a mutual rotation of  $60^\circ$  around  $[111]$  and the weak spots immediately behind those of NbC as belonging to Nb- the electron beam along  $[111]$  of NbC (iii) a lateral set of spots going through the centre and other related spots (not clearly visible) of medium intensity as belonging to  $\alpha$ -FeS. The TEM observation compliment SEM observations showing the presence and distribution of second phase particles and their influence on the fracture characteristics.

The SADP of room temperature tested bend specimens have shown in the figure 50g. The interpretation of SADP is given below:

$R$  = distance from central spot to transmitted spot. Now  $R = 3.65/2 = 1.825 \text{ cm} = 18.25 \text{ mm}$ .

$$\text{We know, } d = \frac{1\lambda}{R} = \text{camera constant}/R$$

$$= \frac{35.97 \text{ mm} \cdot \text{\AA}}{18.25 \text{ mm}} = 1.97 \text{ \AA}.$$

Within the experimental error, assuming,  $d \approx 2.027$  the  $(hkl)$  value of the spot as shown is  $(011)$  [63].

Indexing of other spots can be carried out in a similar manner.

Similarly, (hkl) of spot shown in Fig. 50a is (112).

### 3.9 DETERMINATION OF Q

Activation energy, Q, can be calculated according to the following equation,

$$J_1 = J_{10} + J_1^* \exp(-Q/KT) \quad (49)$$

where  $J_{10} = 7.5 \text{ KJ.m}^{-2}$  at  $0^\circ\text{K}$  from  $J_1$  versus temperature curve.

$J_1^*$  = constant for a particular temperature

Q = activation energy

K = Boltzmann constant =  $8.64 \times 10^{-5} \text{ eV.K}^{-1}$

Equation(49) can be rewritten as,

$$(J_1 - J_{10}) = J_x = J_1^* \exp(-Q/KT)$$

Taking ln on both sides,

$$\ln J_x = \ln J_1^* - Q \frac{1}{KT} \quad (50)$$

Q can be obtained from  $\ln J_x$  versus  $\frac{1}{KT}$  plot, as shown in Fig. 44 . Datas required to calculate Q, are tabulated below:



Temperature (°C)	Temperature (°K)	$\frac{1}{KT}$ (eV <sup>-1</sup> )	$J_x$ (Kj.m <sup>-2</sup> )	$\ln J_x$
-173	103	112.36	5.32	1.671
- 59	214	54.08	37.51	3.624
- 21	252	45.92	132.57	4.887
- 10	263	44.00	161.42	5.084
+ 28	301	38.45	247.50	5.511
+115	388	29.43	243.50	5.495
+140	463	24.998	202.21	5.309
+268	543	21.31	206.92	5.332
+340	615	18.81	261.09	5.564
+440	715	16.18	417.31	6.033
+490	765	15.12	681.52	6.524
+603	878	13.18	492.25	6.198
+693	968	11.96	321.28	5.772
+717	992	11.66	381.48	5.994
+718	993	11.65	324.99	5.783
+727	1002	11.55	299.09	5.700

From Fig. 44,

$$\text{Slope} - Q_2 = - \tan \theta_2 = -\tan \left( \frac{4.5}{17.5} \right) = 0.26 \text{ eV.}$$

$$\therefore Q_2 = 0.26 \text{ eV.}$$

$$\text{Atomic density of (100) plane in b.c.c. } \alpha \text{ Fe} = \frac{1}{a^2}$$

where  $a$  = side of b.c.c. crystal.

$$a \text{ for } \alpha\text{-Fe} = 2.8664 \text{ \AA}$$

$$\text{Now } 1 \text{ eV} = 1.6 \times 10^{-19} \text{ J} = 1.6 \times 10^{-12} \text{ erg}$$

$$\begin{aligned} \text{Therefore, } Q_2 &= 0.26 \times \frac{1}{(2.8664 \times 10^{-8})^2} \times 1.6 \times 10^{-12} \\ &= 506.31 \text{ ergs} \cdot \text{cm}^{-2} \end{aligned}$$

Atomic density of (110) plane, which is the most closest packed plane in b.c.c.  $\alpha$ -Fe =  $\frac{2}{\sqrt{2}a^2} = \frac{\sqrt{2}}{a^2}$

$$\begin{aligned} Q_2 &= 0.26 \times \frac{\sqrt{2}}{(2.8664 \times 10^{-8})^2} \times 1.6 \times 10^{-12} \\ &= 716.0358 \text{ ergs} \cdot \text{cm}^{-2} \end{aligned}$$

again from Fig. 44,

$$-Q_1 = -\tan \theta_1 = -\tan \left( \frac{3.25}{15} \right) = -0.216 \text{ eV}$$

$$\text{Therefore, } Q_1 = 0.216 \text{ eV}$$

$$\begin{aligned} \text{For (100) plane, } Q_1 &= 0.216 \times \frac{1.6 \times 10^{-12}}{(2.8664 \times 10^{-8})^2} \\ &= 420.6299 \text{ ergs} \cdot \text{cm}^{-2} \end{aligned}$$

$$\begin{aligned} \text{For (110) plane, } Q_1 &= 0.216 \times \frac{\sqrt{2} \times 1.6 \times 10^{-12}}{(2.8664 \times 10^{-8})^2} \\ &= 594.86 \text{ ergs} \cdot \text{cm}^{-2} \end{aligned}$$

(100) and (110) planes are chosen because actual plane where crack is occurring cannot be determined.

It has been found in literature [54 and .61] that for pure Fe, value of  $Q$  is approximately  $2000 \text{ ergs/cm}^2$ . So we see that there is a significant lowering of  $Q$ . The reasons for this are discussed in literature and have been included in theory section [56,57,58,59,60]. Grain boundary segregation of sulfur may cause the decrease in  $Q$  and thereby can lower the energy required for cleavage crack propagation, helps in promoting brittle intergranular fracture and increase the ductile-brittle transition temperature (DBTT). Sulfur can accumulate on opened crack faces in the form of  $\text{MnS}$ , thereby promotes decohesion of grain boundary .

Slopes  $Q_1$  and  $Q_2$  are slightly different because of the different mechanisms acting at different temperatures, also evident from the values of  $J_1^*$ .

$Q=0$  for dynamic strain ageing region, may be due to very high diffusion rate of carbon atoms.

### CONCLUSION

The concept of J- integral and J-estimation through bend test procedure, thus well suited our study of J-dependence on temperature. Charpy impact tests and tensile tests conducted over the temperature matched well with the  $J_1$  versus temperature curve. Strain rate effects on various procedures have been noted. An attempt was made to see the effects of sulfur content and sulfide morphology on fracture toughness by using Electron Micro Probe Analysis, Scanning Electron Microscopy and Transmission Electron Microscopy. Fracture of sulfide inclusions appears to play a key role in initial crack extension, both by cleavage by dimpled rupture. The higher value of transition temperature has been attributed to the presence of these microconstituents. This work is a kind of first attempt to investigate fracture toughness dependence of temperature and undertaken to expand the body of knowledge by identifying microstructural effects on opening mode (Mode-I) cleavage and dimpled rupture resistance.

# REFERENCES

1. Griffith, A.A., 'The phenomena of rupture and flow in solids', Phil. Trans. Roy. Soc. 1921, A221, 163.
2. Orwan, E., 'Fracture and strength of solids', Rep. Prog. Phys. 1949, 12, 185.
3. Orwan, E., 'Fatigue and fracture of metals', Symp. at M.I.T., U.S.A., John Wiley and Sons, Inc., New York, 1952.
4. Irwin, G.R. and Kics, J.A., 'Fracturing and fracture dynamics', Weld. J. Res. Suppl. 1952, 17, 95S.
5. Irwin, G.R., 'Analysis of stresses and strains near the end of a crack traversing a plate', J. Appl. Mech. 1957, 24, 361.
6. Irwin, G.R., 'Fracture on encyclopaedia of physics', Vol. VI, Springer, Heidelberg, 1958.
7. Westergaard, H.M., 'Bearing pressures and cracks', J. Appl. Mech. 1939, 61, A49.
8. Irwin, G.R., 'Analysis of stresses and strains near the end of a crack traversing a plate', Trans. ASME, J. Appl. Mech. 24, pp. 361-4.
9. Wells, A.A. (1961), 'Unstable crack propagation in metals: Cleavage and fast fracture', Symp. Crack Propagation, College of Aeronautics, Cranfield, Paper B4.
10. Cottrell, A.H., 'Theoretical aspects of radiation damage and brittle fracture in steel pressure vessels' Iron and Steel Inst. Spec. Rep. 1961, No. 69, pp. 281-96.
11. Barenblatt, G.I., 'The mathematical theory of equilibrium cracks in brittle fracture', Adv. in Appl. Mech. 1962, 7, Academic Press, New York.
12. Dugdale, D.S., 'Yielding of steel sheets containing slits', J. Mech. Phys. Solids 1960, 8, 100-104.
13. Wells, A.A., 'Unstable crack propagation in metals: Cleavage and fast fracture', Crack Propagation symposium, Cranfield, 1961.

14. Rice, J.R., 'A path independent integral and the approximate analysis of strain concentration by notches and cracks', J. Appl. Mech. 1968, 35, 379-386.
15. Hutchinson, J.W., ' Singular behaviour at the end of a tensile crack in a hardening material', J. Mechs. and Phys. of Solids 16, 1968, 13-31.
16. Rice, J.R. and Rosengren, G.F., ' Plane-strain deformation near a crack tip in a power law hardening material', J. of Mechs. and Phys. of Solids, 16, 1968, 1-12.
17. McClintock, F., ' Plasticity aspects of fracture' Fracture, Vol. III, Ed. Liebowitz, H., Academic Press, New York, 1971, pp. 47-225.
18. Broberg, K.B., ' Crack growth criteria and nonlinear fracture mechanics' J. Mechs. and Phys. of Solids, 19, 1971, pp. 407-418.
19. Rice, J.R. et al., ' Some further results of J integral analysis and estimates' in Progress in flow growth and fracture toughness testing, 1973, ASTM-STP 536, pp. 231-45.
20. Buzzard, R.J. and Fisher, D.M., ' Load-displacement and work deformation in three-point bend tests', J. of Testing and Evaluation, JTEVA, Vol. 6, No.1, Jan.1978, pp. 35-39.
21. Davis, M.G., ' Elastic-plastic fracture toughness based on the COD and J-contour integral concepts', Elastic-Plastic Fracture, ASTM STP 668.
22. Joyce, J.A. and Paris, P.C., ' Direct evaluation of J-resistance curves from load displacement records', Fracture Mechanics, ASTM STP 700, 1980, pp. 232-36.
23. Irwin, G.R. and Roland de Wit, ' A summary of fracture mechanics concepts', J. of Testing and Evaluation, JTEVA, Vol. 11, No. 1, Jan. 1983.
24. Clarks, G.A., Begley, J.A. et al., ' A procedure for the determination of ductile fracture toughness values using J integral techniques', J. of Testing and Evaluation, Vol. 7, No.1, Jan. 1979.
25. Chipperfield, C.G., ' A summary and comparison of J estimation procedures', J. of Testing and Evaluation, Vol. 6, No. 4, July 1978.

26. Landes, J.D. and Begley, J.A., 'The effect of specimen geometry on  $J_{1c}$ ', ASTM STP 514, 1972, pp. 24-39.
27. Rice, J.R., Bucci, R.J. and Landes, J.D., 'J integral estimation procedures', ASTM STP 514, 1972, pp.40-69.
28. Landes, J.D., Begley, J.A. and Clarke, G.A., 'Elastic-plastic fracture', ASTM STP 668, 1977.
29. Landes, J.D. and Latzko, D.G.H., 'Post-yield fracture mechanics', Second Edition, 1984, Elsevier Applied Science Publishers, London and New York.
30. 'A general introduction to fracture mechanics', A Journal of Strain Analysis Monograph, Mechanical Engineering Publications Limited, London.
31. 'Developments in fracture mechanics test methods standardization', Editors, Brown W.F. and Kaufman, J.G., ASTM STP 632, 1976.
32. Kare Hellan, 'Introduction to fracture mechanics', 1984, McGraw-Hill Book Company.
33. 'Advances in elasto-plastic fracture mechanics' Ed. by Larsson, L.H., 1979, Applied Science Publishers Ltd., London.
34. Robinson, J.N., 'An experimental investigation of the effect of specimen type on the crack tip opening displacement and J integral fracture criteria', Int. J. of Fracture, Vol. 12, No.5, Oct. 1976.
35. Scanning Electron Microscopy by Wells O.C., Boyde. A., Lifshin. E., Rezanowich A.
36. Scanning Electron Microscopy by Thorton P.H.
37. Metals handbook, V.9, p.49-63.
38. Applications of modern metallographic techniques - ASTM STP 480, 1969, p. 182-211.
39. Developments in Electron Microscopy and analysis 1977 Proc. of Inst. of Physics Electron Microscopy, Glasgow- Edited by D.C. Misell, p. 333-336.
40. Transmission Electron Microscopy of Metals by Garath Thomas .

41. Steels and its heat treatment- Thelning p.194 - 195  
p.209 - 211, p.214-223.
42. Theory of Heat treatment of metals by Novikov p.294,  
p.188.
43. R. Kiesling and N. Lange, ISI Pub., No. 100, 1966.
44. E. Scheil and R. Schnell, Stahl U. Eisen, 1952, 72,  
p.683-687.
45. F.B. Pickering , J.I.S.I., 1958, 189, p148-159.
46. T. Malkiewicz and S. Rudnik, J.I.S.I., 1963,201,  
p.33-38.
47. S. Rudnik, J.I.S.I., 1966,204, p.374-376.
48. W. Dahl and W. Henstenberg and C. Duren, Stahl U.  
Eisen, 1966, 86, p.796-817.
49. L. Roesch, G. Henry, J. Plateau: Mem. Sci.Rev.Met.,  
1966,63,p.941-950.
50. D. Hall, Proc. Roy. Soc. London, A., 1965, 285,  
p.148-150.
51. Inclusions and their effects on properties by Dulien  
and Gouch, 1974, BSC PMC Conf.
52. Non-metallic inclusions in steel by Roland Kiesling  
p.94- 107.
53. Inclusions by F.B. Pickering p.94-102.p.157-165,  
187-190, p.32-33.
54. Interfacial Phenomena in Metals and Alloys by L.E.  
Murr p.10.
55. Handbook of surfaces and interfaces by Leonard Dobrz-  
ynski, p.7.
56. Proc. Roy Soc. London, A., 286, p.479, 1965-E.D.  
Hondros.
57. P.V. Ramasubramaniam and D.F. Stein, Metall. Trans.,1973  
4, p. 1735.
58. M.E. Fine, J. P. Stark, H.L. Marcurs, Scripta Metallu-  
rgica, 1986, V.20, p.1619-1620.



59. Suzuki.S, Tani.K, Kimura, H., Metal Trans A., Vol.18A, No.6, 1987, p.110p-1115.
60. C.A. Hippsley, Acta Metall. 1987, Vol.35, No.10, p.2399-2416.
61. Physical Chemistry of Melts in Metallurgy, Vol.2, Richardson. F.D., 1974, p.426-p.431.
62. Introduction to mechanics of solids, Crandall. S.H., Dahl N.C.
63. Interpretation of Diffraction Patterns-Andrews K.W., Dyson . D.J. Keown S.R. p.211.
64. Metals Handbook, 8th Edition, Vol.10, 'Failure Analysis and Prevention'.
65. Microstructure and Design of Alloys, Proc.3rd Int. Conf., ISI, Stein D.F. 1973, p.58-88.
66. Spitzig A., Metall. Trans. A, Vol. 14A, 1983 p.471-484.
67. Microstructural Science, Cutler L.R., Krishnadev, M.R. 1982 Vol.10, p.79-90,
- 68, Circular IC 299, 1973 Department of Energy, Mines and Resources, Mines Branch, Ottawa, Boyd.